The University Of Sheffield.

MULTISCALE MODELLING OF STENT/VESSEL INTERACTIONS

CLAUDIA MARIA AMATRUDA

School of Medicine and Biomedical Sciences
Department of Cardiovascular Science
Medical Physics Group

Submitted for the degree of Doctor of Philosophy

Submission Date
October 2015

ABSTRACT

Angioplasty with stenting re-opens stenosed arteries, but in-stent restenosis remains a common negative outcome. Correlations between local mechanical stimuli and ISR have been reported, explained by mechanotransduction mechanisms that influence cell behaviour. This thesis investigates the loads imposed on the coronary artery following stent implantation.

The changes in mechanical stimuli in a vessel following stent deployment were initially considered using a simple MATLAB model, followed by analysis of a 2D cross-section model to represent variation of stress with stent strut distribution. This model revealed the distribution of the stress through the thickness and around the circumference varied significantly for high expansion ratios and uneven strut distributions.

A 3D continuum model of stent geometry post-expansion, obtained from micro-CT images, was used to analyse stent interaction with an idealised vessel geometry. The structural stress at the level of individual struts was compared to histological data and to fluid dynamic simulations of the same stent/vessel geometry. When structural and fluid dynamic stimuli were considered together, correlations with the amount of neointimal growth became more significant than when they were considered individually. This suggests that both stimuli contribute to the development of neointimal growth and their combination may accelerate the progression of ISR.

Finally, the thesis describes a model of the evolution of in-stent restenosis. A cellular model of growth was developed to include feedback from a finite element model of the vessel and neointima. Change in the lumen geometry was captured with neointimal growth, an updated geometry was passed to the finite element model to compute the subsequent change of stress direction on cells during their growth. The results show encouraging resemblance with histological images of ISR, especially for the early phases of growth. The thesis concludes with a summary of the modelling results and a review of opportunities for further research.

ACKNOWLEDGEMENTS

The realisation of this work would have not been possible without the help of a number of people over the years – so many I am not even able to count them.

My deepest gratitude goes to Dr. Andrew Narracott, for the endless support provided under every aspect of the PhD, including the understanding of WHAT research actually is. I would also like to thank Prof. Rodney Hose and Prof. Patricia Lawford, for providing their expertise to help choose the direction to take during the process.

The whole Medical Physics group, thank you all for sharing stretches of time with me, in the office and out; it was heart-warming to realise how many of you became actual friends. A special mention goes to my everything-buddy Iwonka, for being so close to me since my very first hours in Sheffield, and Angelina, for not hating me in the most difficult hours (maybe days…or months?) of the writing period.

Thanks to all the people that have been supporting me during my crises, moments of discouragement and shared my joy in the most exciting points of my research, even without a complete understanding of the actual reason of such joys. My family, so far and yet so incredibly close; my housemates, who had to stand me even against their will; my friends, the ones here and the ones there, disseminated around the world.

Thanks Sheffield, the Peak District and the incredible people living here: I moved from my beloved country for a PhD but through this place I discovered aspects of myself I would have not thought existed before.

And thanks to everyone that keeps reminding me that science is actually really fun.

This research was made possible thanks to the financial support from the EU in the form of a Marie Curie fellowship (Project MeDDiCA Marie Curie Initial Training Network, www.meddica.eu, EU-FP7/2007-2013, Grant agreement PITN-GA-2008-238113).

TABLE OF CONTRIBUTIONS

The work of this thesis is the work of the author, but it also relies on the efforts of other individuals and groups working in the same or related fields. For purposes of clarification, significant contributions to the work of the thesis not undertaken by the author are presented below.

Chapter I constitutes a review by the author of the clinical problem of ISR and a review of the models in the literature.

The first part of Chapter II introduces the modelling of ISR, with a description of the mechanical environment followed by a simple analytical model, produced by the author; the second part is a literature review of ISR models of other authors.

The content of Chapter III includes a symmetric model of stent deployment and a model with uneven strut distribution, all based on work of the author; one histology image from previous research (Fig.III.11) has been used to choose the set-up of the model.

Chapter IV presents a 3D stent/vessel model based on work from multiple research centres. Specifically the *Histology Data* used for the study was provided by Prof. Julian Gunn; the *Structural Analysis* section describes work developed by the author, while the *Fluid Dynamic Analysis* was developed by Brandis Keller (Politecnico di Milano, Italy); the *Statistical Analysis* is the result of the collaboration between Brandis Keller and the author.

The content of Chapter V is a model of ISR, produced by the author; histology images from Prof. Julian Gunn and of the results of work by Tahir *et al.* are reported for results analysis and comparison.

Chapter 6 is a summary/discussion of the work by the author.

TABLE OF CONTENTS

LIST OF FIGURES

LIST OF TABLES

CHAPTER I – INTRODUCTION TO ISR

INTRODUCTION

Ischemic heart disease represents the most common cause of death and disability in the world, and one of its manifestations is obstructive coronary artery disease (CAD), which causes over 4 million deaths in Europe each year, that corresponds to 45% of deaths in Europe (Townsend, Nichols et al. 2015).

Atherosclerosis is the primary cause of coronary artery disease (Libby and Theroux 2005). Atherosclerotic disease is mostly treated with percutaneous coronary interventional procedures, stenting operations in particular. One of the main disadvantages of this technique is in-stent restenosis (ISR), which occurs a few months after this intervention (Gunn and Cumberland 1999) in 20% of all bare metal stent cases (Kim and Dean 2011).

Considerable effort has been made by the scientific community to solve or diminish the problem through various strategies: through product design, attempting to produce new more biocompatible stents, or based on gaining a better understanding of the mechanisms associated with in-stent restenosis, using *in vivo* and *in vitro* models. It is essential to improve knowledge about not only how this phenomenon starts, but also about both its development over time and how it stops.

This Chapter provides an overview of the problem of in-stent restenosis from the clinical point of view. Section 1 gives a brief description of the anatomy of the coronary arteries and Section 2 illustrates the process of development of atherosclerotic disease that might eventually lead to stenosis and require revascularisation via stenting. Section 3 summarises the historical evolution of revascularisation from angioplasty to the most modern concept of stents and the issues encountered with each new technology. An analysis of the desirable characteristics of a stent is presented and the influence of stent design and material properties on the ability to meet these needs is discussed. Section 4 describes the problem of in-stent restenosis, its incidence, evolution and possible interventions. Section 5 provides an overview of how the presence of a stent and its alteration of the mechanical environment can stimulate a local biological reaction in the vessel wall through a brief description of mechanotransduction mechanisms at the cellular level. Finally, Section 6 provides a review of strategies reported in the literature to model the interaction between the stent and vessel wall immediately after stenting.

1.1 CORONARY ARTERIES

Coronary arteries are the vessels responsible for supply of oxygen to the heart muscle. *Figure I.1* shows the two main coronary arteries which originate from the beginning of the aorta, above the aortic valve. Their typical branching is described below but anatomical variations between individuals are common.

- The right coronary artery (RCA): provides blood to the right atrium, the right ventricle, the posterior portion of the left ventricle and the interventricular septum.
- The left coronary artery (LCA): typically runs for 1 to 25 mm and then bifurcates into the Left Anterior Descending (LAD) artery, that supplies blood to the left atrium and the lateral and posterior of the left ventricle, and the Left Circumflex Artery (LCX), that supplies blood to the anterior and inferior of the left ventricle and front of the septum (*Figure I.1*) (Ramanathan and Skinner 2005). Stents are typically implanted in vessels 2-4 mm in diameter (Morlacchi and Migliavacca 2013).

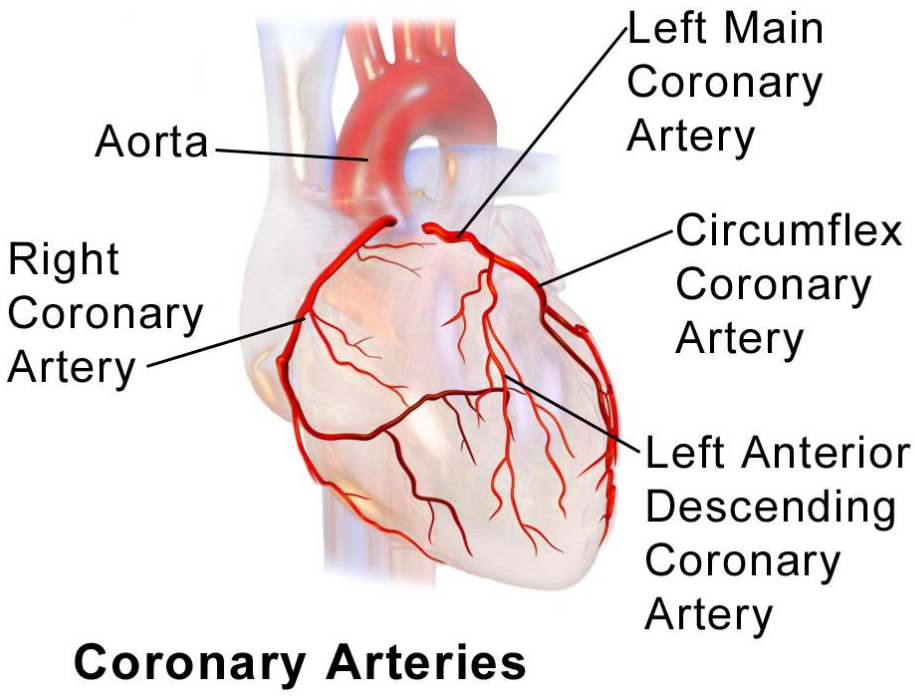

Figure I.1 – Anterior view of the heart showing coronary arteries. Figure reproduced with permission under CC BY-SA 3.0 via Wikimedia Commons - By BruceBlaus (Own work)

Figure I.2 shows the complex structure of a normal artery wall which is composed of a number of different layers, each of which has a different role and contributes differently to the vessel properties:

- The tunica intima is composed of a single layer of endothelial cells (ECs), a selectively permeable barrier between blood and tissues, over a basement membrane composed of collagen IV, fibronectin, laminin, and the internal elastic lamina (IEL), a fenestrated sheet of elastic fibers (Lusis 2000). It has an important physiological role, but it contributes negligibly to the mechanical properties.
- The tunica media is mainly composed of layers of nearly circumferentially oriented smooth muscle cells (SMCs): this layer represents the greatest volume of the artery wall. It is responsible for most of mechanical properties of the vessel, and can also relax or contract. It is composed of SMCs, elastin, collagen I, III, V and proteoglycans.
- The tunica adventitia contains many blood vessels to provide oxygen to the cells of the vessel wall, and is composed mainly of fibroblasts. The other components are collagen I, nerves and some elastin fibres (Evans, Lawford et al. 2008).

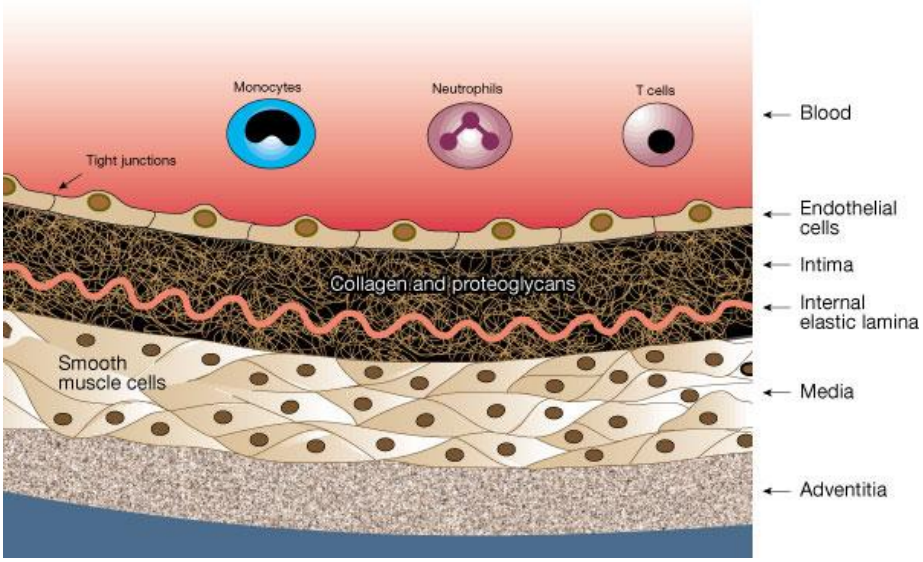

Figure I.2 - Structure of a general artery. Reproduced with permission from (Lusis 2000).

The description above relates to the anatomy and structure of normal, healthy coronary arteries; the changes which occur in these vessels during development of atherosclerotic disease are described in the following section.

1.2 ATHEROSCLEROSIS AND ARTERIAL STENOSIS

Atherosclerosis is a progressive disease of medium and large arteries that, through initial development of fatty streaks and changes in vessel wall stiffness, leads to more complex lesions which can result in reduction of the vessel lumen in the form of a local stenosis (Crowther 2005).

The earliest visible atherosclerosis lesions consist of an accumulation of 'foam cells' (cholesterol-engorged macrophages) in the intimal layer of the vessel. These 'fatty streaks' can be found even in the first decade of life, usually localised in the aorta, while in the second decade they tend to develop in the coronary arteries and in the cerebral arteries in the third or fourth decade (Lusis 2000).

More advanced lesions are characterised by a lipid-rich necrotic core and a fibrous cap, which is the distinctive sign of established atherosclerosis composed of smooth muscle cells (SMCs) and extra-cellular matrix (ECM) (Crowther 2005). Plaque composition can change over time with the development of calcification, growth of new vessels into the new tissue and subsequent ulceration and haemorrhage. Unstable plaques can break and detach, and the formation of the consequent thrombus provokes an acute occlusion: this may result in myocardial infarction or stroke (Lusis 2000).

Atherosclerosis is considered to be a mostly inflammatory process that starts decades before the formation of an established lesion. The first event is thought to

be a perturbation in the function of the endothelial barrier and a subsequent increase of cellular adhesion and permeability of macromolecules such as LDL, which diffuse passively though the endothelium and accumulate in the vessel wall (Lusis 2000, Crowther 2005). LDL molecules are therefore exposed to the oxidative waste of the surrounding cells and can become oxidised, making them particularly atherogenic. In this form, these modified molecules attract macrophages to the site, which, taking up the oxidised-LDL, lose mobility and become foam cells. These cells send inflammatory signals, provoking recruitment and proliferation of SMCs and enhancing the processes leading to the formation of new foam cells. The presence of SMCs and their production of connective tissue leads to the formation of the fibrous cap (Lusis 2000, Crowther 2005).

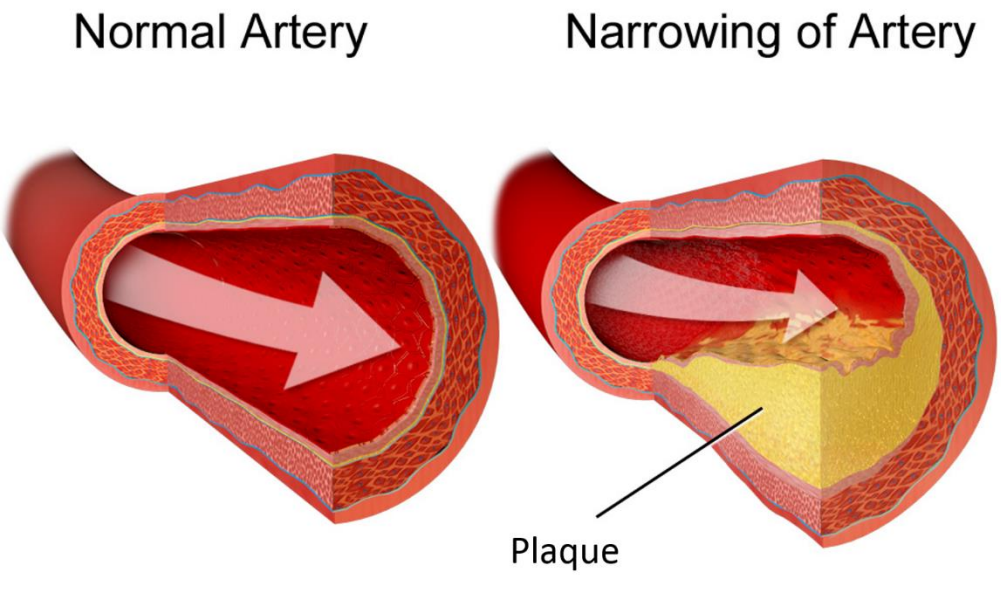

Figure I.3 - Atherosclerotic plaque that narrows the artery and reduces the blood flow. On the left: normal artery with normal blood flow. On the right: artery with plaque build-up. (Figure adapted with permission under CC BY-SA 3.0 via Wikimedia Commons - from Blausen.com staff. "Blausen gallery 2014". Wikiversity Journal of Medicine. DOI:10.15347/wjm/2014.010. ISSN 20018762)

In the advanced stages of atherosclerosis, the plaques that form in the vessel wall reduce the lumen of the artery, leading to a focal narrowing, or stenosis, which may

be either concentric or asymmetric. This narrowing of the artery may occlude blood flow within the vessel and deprive downstream tissues of oxygen (*Figure I.3*), while rupture of the plaque and subsequent thrombosis can lead to myocardial infarction or stroke. However, the risk of thrombosis depends more on the composition and vulnerability of the plaque rather than the severity of the stenosis (Lusis 2000).

The factors that have been associated with the risk of atherosclerosis are: high cholesterol, elevated blood pressure, cigarette smoking, obesity, lack of exercise, age, family history, diabetes and male sex (Lusis 2000).

The "gold standard" to evaluate coronary artery disease (CAD) is an angiographic assessment, which only gives information about the vessel lumen. Some information about the plaque anatomy can be obtained from other techniques such as coronary computed tomography angiography (CTA) or magnetic resonance imaging (MRI), while functional testing such as exercise ECG can give a support to the diagnosis of stable CAD, helping to find its correlation with the occurrence of the symptoms (Members, Montalescot et al. 2013).

The decision to treat the patient is aimed at reducing the symptoms and at preventing events such as myocardial infarction (Members, Montalescot et al. 2013). Following the decision to treat an atherosclerotic lesion, a number of clinical approaches are available; these are described in the following section.

1.3 HISTORY OF STENTS AND TYPES

Treatments: from open surgery to bioresorbable scaffolds

Prior to the development of minimally-invasive procedures, treatment of coronary artery lesions was based on open surgery, such as coronary artery bypass grafting (CABG). In the 1960s the development of catheter-based therapies introduced the concept of minimally-invasive procedures (Duraiswamy, Schoephoerster et al. 2007). In 1977 percutaneous transluminal coronary angioplasty (PTCA) was introduced: catheters were used to open stenoses by means of a balloon expanded with saline solution. The main issue with this intervention was acute occlusion: the change in vessel diameter caused by inflation of the balloon was not maintained following removal of the balloon due to the elasticity of vessel wall and of some atherosclerotic plaque components (Serruys, Garcia-Garcia et al. 2012).

During the same period coronary stents were also under development, with the first implantation in a human performed by Sigwart *et al.* in 1986 (Sigwart, Puel et al. 1987); but the first balloon-mounted vascular stent approved by the United States FDA was the Palmaz-Schatz® stent (Johnson & Johnson) in 1987 (Iqbal, Gunn et al. 2013). Since then, stents have gradually become the percutaneous coronary interventional procedure of choice, with both angioplasty and stenting used in the vast majority of interventional cases (Iqbal, Gunn et al. 2013).

A stent is a small tube-like structure that surrounds the deflated balloon and expands during balloon inflation, undergoing plastic deformation (*Figure I.4*). It expands into the artery wall, dilates the narrowed lumen and maintains an open configuration, improving blood flow (Duraiswamy, Schoephoerster et al. 2007). The

presence of the metallic cage avoids recoil and constrictive remodelling, as observed with balloon angioplasty alone. However, the phenomenon of in-stent restenosis (ISR), due to proliferation and migration of vascular smooth muscle cells (VSMCs), was observed in 20-30% of cases of BMS during clinical medium and longer term follow-up of stented patients (Iqbal, Gunn et al. 2013). ISR is a biological response to stent implantation, described in detail later this Chapter, which represents a clinically significant and unsolved issue, involving the development of a neointima within the stent. The amount of neointima generated after stent implantation is greater than that provoked by angioplasty alone. In addition, the presence of the metallic stent material leads to an increased risk of subacute and late stent thrombosis (Serruys, Garcia-Garcia et al. 2012) (Top part of *Figure I.5*).

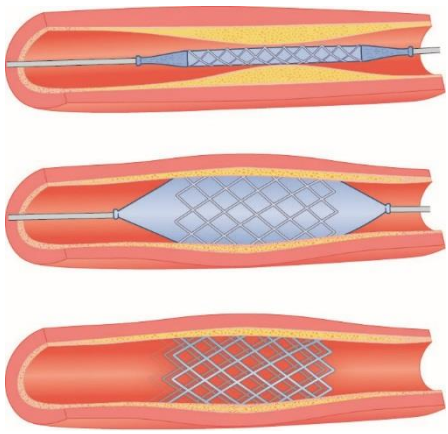

Figure I.4 – The catheter with the stent crimped on the balloon is positioned in the narrowed artery; the balloon is inflated, generating stent plastic deformation; the expanded stent maintains the vessel open, improving blood flow. Used with permission from Morris P, Warriner D, Morton A. Eureka Cardiovascular Medicine. London: JP Medical Ltd, 2015.

The next technological evolution in the field involved the idea of covering the stent with cytostatic and cytotoxic drugs, with the aim of reducing the ISR response. This new generation of stents consists of a bare-metal stent coated with a polymer that continuously releases a drug to reduce new tissue growth and prevent significant stenosis development (Serruys, Garcia-Garcia et al. 2012, Bangalore, Toklu et al.

2013). These devices are referred to as Drug Eluting Stents (DES). The downside of this approach was the increased risk of late and very late stent thrombosis, which has been associated with late persistent or acquired malapposition of the stent struts to the vessel wall. The latter might be caused by the weakening effect of the drugs on the vessel wall in contact with the stent struts, which provokes a retraction of the tissue (Serruys, Garcia-Garcia et al. 2012, Bangalore, Toklu et al. 2013). Another provoking factor is considered to be the delay in re-endothelialisation due to the anti-proliferative drugs (van Beusekom and Serruys 2010) (Bottom part of *Figure I.5*).

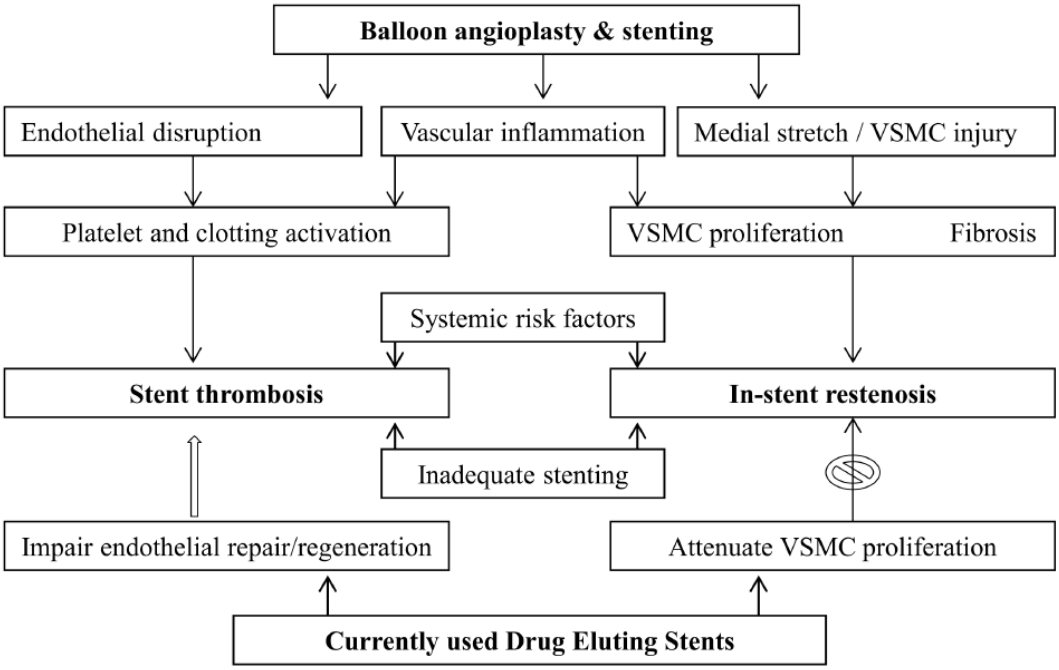

Figure I.5 - Scheme of the possible outcomes of the current forms of intervention. Reproduced with permission from (Iqbal, Gunn et al. 2013).

To avoid the chronic effects associated with stent implantation, recent research has developed the concept of designing a device that would disappear once its structural function was not needed anymore. This has included experimentation with polymer stents, starting with implantation of biostable polymeric stents in pigs in the early 1990s, progressing to commercially available bioresorbable scaffolds (BRS). There

are 20 stents currently undergoing pre-clinical or clinical testing and 3 have been already approved with a CE mark (Iqbal, Onuma et al. 2014). The challenge with use of such stents arises due to their poor expansion properties, concerning in particular polymeric scaffolds, resulting in a higher risk of stent fracture (Serruys, Garcia-Garcia et al. 2012).

The following section describes the characteristics of an ideal stent and discusses how stent geometry design and material properties influence the ability to meet these needs.

Stent classifications

Coronary artery stents have been developed with various materials, technologies and geometric designs to be able to meet some fundamental guidelines to obtain an easily usable device, able to sustain its function but with the lowest possible impact on the biological environment of the vessel. These can be summarised by the points in *Table I.1* (Butany, Carmichael et al. 2005):

Table I.1 - Desirable stent characteristics. Reproduced with permission from (Butany, Carmichael et al. 2005)

Low crossing profile
High flexibility
High stent/host biocompatibility
High radial strength
Low metallic surface area
Favourable radiographic properties
Good trackability (ability to conform to tortuous vessel)
Easy deployment

Stents can be divided into different categories based on the design choices. The main design categories are (Butany, Carmichael et al. 2005);

- a coil shape formed by wires;

- a tubular mesh formed by wires wound together;
- a slotted tube, obtained by laser-cutting a metal tube

Other categories are based on the nature of expansion, dividing stents between self-expanding or balloon expandable (Butany, Carmichael et al. 2005), and the cell configuration, which can be open-cell and closed-cell. Closed-cell stents are preferred for DES for a more homogeneous release of the drug to the vessel thanks to the small changes of cell geometry even when bent (Hara, Nakamura et al. 2006). Stent strut thickness has been shown to influence the biocompatibility of the stent, with thinner struts reducing neointimal hyperplasia as they create less vascular injury. Thicker struts, on the other hand, offer more radiopacity and radial force, hence better arterial support (Hara, Nakamura et al. 2006).

The choice of stent material has an impact on the design, as novel material types have provided more radial resistance with thinner struts. This is the case with the use of cobalt-chromium alloy instead of 316L stainless steel for BMS (*Figure I.6.a*), which was initially chosen for being biologically inert. The newest material developed for commercially available BMS is a platinum-chromium alloy, which also has higher radiopacity and conformability (Iqbal, Gunn et al. 2013). Attempts to cover stents with materials such as polytetrafluoro-ethylene (PTFE) to increase biocompatibility have not shown any improvement in ISR rates, but as changes in the surface can affect biological reactions such as cell adhesion, treatments such as electropolishing can improve the response for steel stents; coatings such as gold, silicon carbonide, heparin or phosphoricholine have been attempted with the same aim, but the same improvement has not been reached (Hara, Nakamura et al. 2006).

In case of DES, the most commonly used drugs whose release can help reducing ISR are sirolimus, everolimus (*Figure I.6.b*) and paclitaxel. Finally, a new generation of stents is currently under development for clinical use, the Bio-Resorbable Stent (BRS). The first BRS design implanted in humans during a preliminary study in 1998 (Tamai, Igaki et al. 2000) was made of poly-L-lactic acid (PLLA), with no coating; current designs are made of either a metallic alloy, usually based on iron or magnesium, or a polymer, usually PLLA and poly-DL-lactic acid (PDLLA) (*Figure I.6.c*) (Iqbal, Onuma et al. 2014).

a. **b.** **c.**

Figure I.6 – Examples of different types of commercial stents a. BMS: Direct-Stent Cobalt Chromium (InSitu Technologies) b. DES: PROMUS Element™ Plus Platinum Chromium Everolimus-Eluting Stent System (Boston Scientific); c. BRS: Absorb Bioresorbable Vascular Scaffold, everolimus-eluting BRS composed of PLLA and PDLLA (Abbott)

Section 4 describes more in depth in-stent restenosis: what it is, how it evolves and why it is clinically important.

1.4 EVOLUTION OF IN-STENT RESTENOSIS

Restenosis is the arterial healing response that limited the success of PTCA, creating the need for a device that would have a better long-term outcome, maintaining the new lumen provided by angioplasty, the stent (Schiele 2005).

Since their first introduction in the 1980s, stents have been applied with increasing enthusiasm, with 3 million stents implanted every year in the world (van Beusekom and Serruys 2010), thanks to their efficacy in restoring an adequate blood

flow in arteries occluded by an atherosclerotic lesion. Unfortunately, stented lesions can experience an inflammatory and reparative reaction which leads to in-stent restenosis (ISR) within a few months (Gunn and Cumberland 1999). As introduced in the previous section, the extent of this phenomenon is considerable, with ISR occurring in 20% of cases of bare metal stent implantation (Kim and Dean 2011); this outcome is reduced to less than 10% in case of DES (Stettler, Wandel et al. 2007). This prompts the need for further studies of the causes of the phenomenon, of its evolution and of the possible factors able to limit its onset and development.

In some cases the risk of ISR becomes even higher, with up to 50% incidence in diabetic patients, totally occluded vessels or if the implanted stents are small (< 3 mm in diameter), long, overlapping or multiple (Moore and Berry 2002).

The main difference between restenosis following balloon angioplasty and ISR is observed in the type of response to the treatment. Restenosis following angioplasty is caused mainly by early elastic recoil and negative remodelling, while in ISR neointimal hyperplasia plays the main role (Schiele 2005).

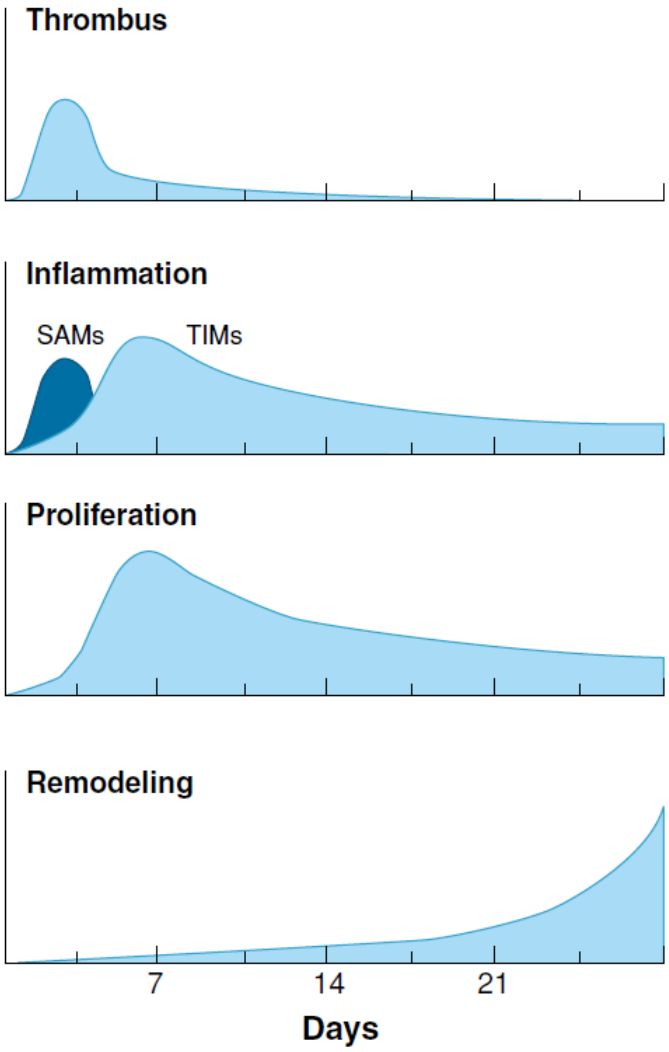

Figure I.7 – Distinct components of the biological response to stent implantation vs time. For the inflammatory response, the two peaks represent the heightened activity level of two different types of monocytes. Reproduced from (Duraiswamy, Schoephoerster et al. 2007), permission was not required.

In-stent restenosis is caused by neointimal hyperplasia (NIH) and develops over a period of several months. The reaction to stenting is complex with many participating factors, but it has been described in four main phases (*Figure I.7*): thrombosis, inflammation, proliferation, and remodelling (Edelman and Rogers 1998).

- Thrombosis: this acute reaction, occurring within the first few days, begins with the adhesion of platelets transported to the stent location by the blood flow (Duraiswamy, Schoephoerster et al. 2007). This does not contribute to

significant lumen loss, but the extent of this response has been shown to be affected by the amount of vessel injury (Edelman and Rogers 1998).

- Inflammation: within the first few days inflammatory cells are recruited and deposited on the stent and between the stent struts. Specifically, surface-adherent monocytes (SAMs) and tissue-infiltrating monocytes (TIMs) are delivered by the blood flow (Duraiswamy, Schoephoerster et al. 2007). The adhesion of SAMs decreases 3-7 days after stenting, with increased adhesion of TIMs (Edelman and Rogers 1998).
- Proliferation: both smooth muscle cells (SMCs) migrating from the intima towards the lumen and inflammatory cells contribute to the build-up of neointima (Duraiswamy, Schoephoerster et al. 2007). The stimulus for tissue growth in this phase has been associated with the high stresses on the wall provoked by the presence of the stent, but also with cellular reactions provoked by low wall shear stress (Duraiswamy, Schoephoerster et al. 2007). SMCs are responsible for the production of proteins of the extra-cellular matrix (ECM), which constitutes a considerable volume of the neointimal tissue.
- Remodelling: this phase starts about 3 weeks after stenting. Collagen is deposited in the adventitia and media (Moore and Berry 2002) as part of the adaptation to the new environment post-stenting, changing the vascular geometry and material properties (Duraiswamy, Schoephoerster et al. 2007). In the later stages of the process ISR formation is characterised by ECM formation, rather than cell proliferation (Schiele 2005).

Since neointimal growth is the main contributor to ISR and it consists of cell migration, proliferation and ECM production, it is important to understand how these

processes occur within the cell cycle of SMCs. In fact, the phase of the cycle the cell is in and which phenotype is expressed will influence intracellular signal transduction, which effects on all sort of processes, like proliferation and migration (Schiele 2005). *Figure I.8* illustrates the phases of the cell cycle: SMCs in a mature and healthy blood vessel are in their resting state, in which the differentiated phenotype is expressed. The cell exhibits contractile behaviour and does not divide: this state is called quiescent, *G0* (Rzucidlo, Martin et al. 2007). Stimuli like vessel damage, provoked by events such as angioplasty, can provoke a de-differentiation of the cell, which switches to the synthetic phenotype, characterised by events such as proliferation, migration and ECM production (Beamish, He et al. 2010). In this case, the cell re-enters the first gap phase of the cell cycle, *G1*, which is a growth phase. *S* is the synthetic phase, in which the DNA is duplicated, and *G2* is the second gap phase, where the cell growth continues until it doubles in size. *G1/S/G2* are all part of the *interphase.* The final stage, *M*, is the mitotic state, where a *mother* cell divides into two *daughter* cells (Jones and Chapman 2012). Migration is possible during the transition to *G1* and *S* (Schiele 2005). The knowledge of the cell cycle and the cell signalling process allows development of drugs which intervene in the most effective way on the proliferation of the SMCs.

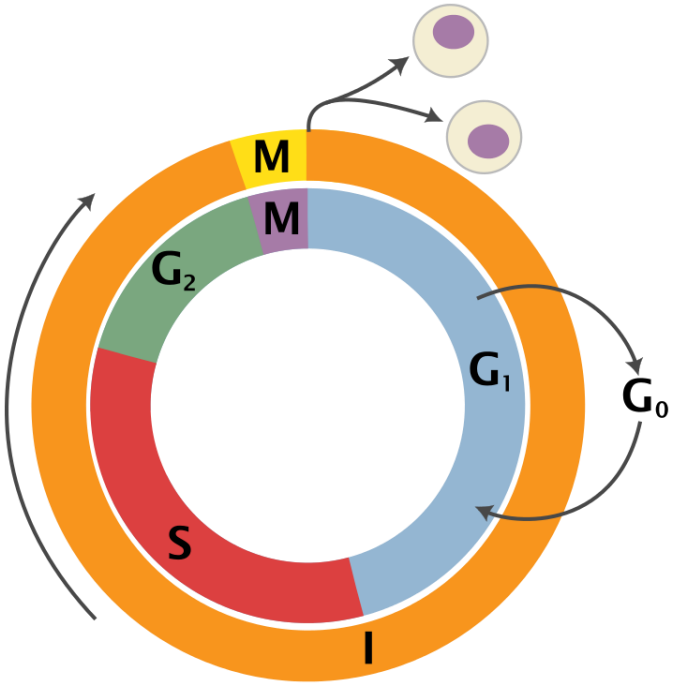

Figure I.8 - Diagram of the phases of the cell cycle (Figure used with permission under CC BY-SA 3.0 via Wikimedia Commons - from "Cell_Cycle_2.png": Zephyris at en.wikipedia derivative work: Beao derivative work: Histidine (Cell_Cycle_2.svg))

The types of ISR have been classified into the following categories, based on the length of the stenosed region and the pattern of growth, which are not only descriptive, but also used to define the clinical prognosis (Schiele 2005):

I. Focal: ISR ≤ 10 mm length

II. Diffuse: ISR > 10 mm length within the stent

III. Proliferative: ISR > 10 mm exceeding the length of the stent

IV. Occlusive.

This classification has been proposed for bare metal stents, while the outcome of DES implantation is mainly focal restenosis (Ong, Aoki et al. 2004).

The treatment of ISR consists in single or combined techniques which aim to re-open the vessel (repeat balloon angioplasty, repeat stenting, drug-eluting stents), to act on the plaque (directional coronary atherectomy, rotational coronary

atherectomy, brachytherapy) or both at the same time (cutting balloon angioplasty) (Ong, Aoki et al. 2004). The use of systemic drug therapy or mechanical treatments of ISR has been shown to be ineffective, while better results have been obtained mainly through vascular brachytherapy and repeat stenting with DES (Schiele 2005). The latter is the current standard treatment for ISR due to BMS, while the best approach for restenosis after DES implant is less clear (Kim and Dean 2011).

The differences in biological response observed between stent designs suggest a relationship between the magnitude of the ISR response and local alterations to the mechanical environment of the vessel wall, arising from stent implantation (Gunn and Cumberland 1999). Examination of these effects using numerical models of stent/vessel interactions is reviewed in Section 6. The following section describes the mechanotransduction mechanisms which have been identified in vascular cells and the relevance of these mechanisms to the development of ISR.

1.5 MECHANOTRANSDUCTION MECHANISMS

The translation of mechanical forces acting on cells into chemical signals is called "mechanotransduction" (Serruys, Garcia-Garcia et al. 2012).

Blood vessel cells are constantly subjected to mechanical forces in the form of stretch, cyclic mechanical strain and shear stress. These mechanical stimuli influence particular cells to maintain tissue homeostasis, regulating cell function such as gene activation, protein synthesis, cell growth, death and differentiation (Wang and Thampatty 2006).

Alterations in stretch or shear stress have been shown to provoke a reaction in the vessel leading to an adaptation to the new mechanical conditions. Stent

implantation is an example of such an alteration in loading as it generates high concentrations of stress behind the stent struts (Lehoux and Tedgui 2003).

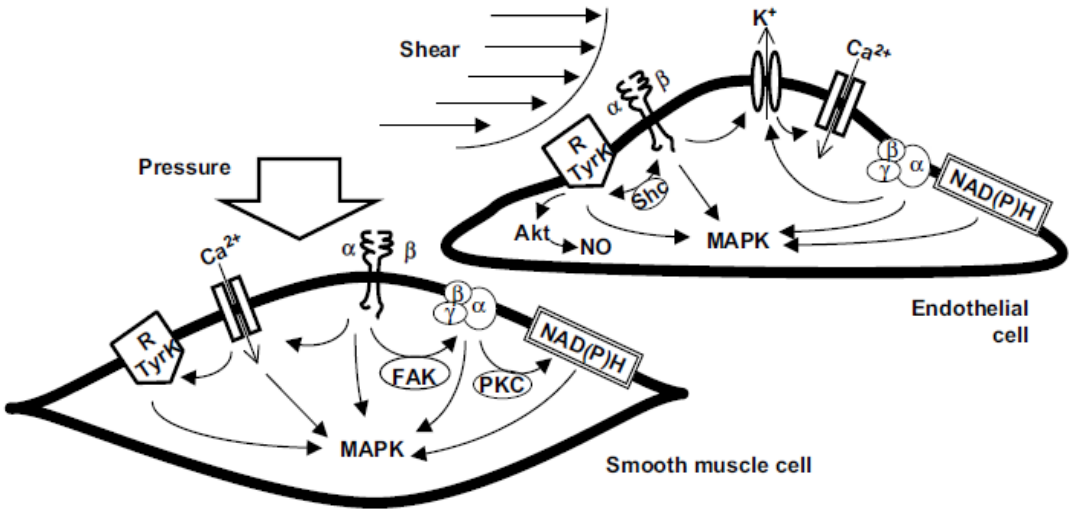

Figure I.9 - Schematic representation of receptors involved in initiating cascades in vascular cells stimulated by pressure (stretch) or shear stress, in particular in smooth muscle cells and endothelial cells. Reproduced with permission from (Lehoux and Tedgui 2003).

The extra-cellular matrix (ECM), which provides structural support to the tissue and an adhesive surface to the cells, is also responsible for the transmission of the mechanical stimuli to the cells (Gupta and Grande-Allen 2006).

As shown in *Figure I.9*, in arterial vessels the cells that respond most significantly to mechanotransduction effects are smooth muscle cells (SMCs), which respond to changes in transmural pressure, and endothelial cells (ECs), which respond to changes in shear stress.

Below the level of a single cell, the individual cellular components involved in mechanotransduction mechanisms are as follows:

- The cytoskeleton is a network of microfilaments, microtubules and intermediate filaments that determines the mechanical properties of the cell, connects nearly all

cellular structures and, through changes in its structure, transduces mechanical loads into biological signals (Wang and Thampatty 2006).

- Integrins (represented as α and β in *Figure I.9*) are cell surface protein receptors that act as an interface between the extracellular matrix and the cytoskeleton of the cell. The mechanotransduction role of integrins is specific to the individual integrin-extracellular matrix interaction (Lehoux and Tedgui 2003).
- Heterodimeric G proteins are another type of membrane proteins: composed of three subunits (α, β, γ in *Figure I.9*), they couple membrane receptors to the intracellular signalling cascade. Shear forces deform the cytoskeleton acting on integrins, in turn activating a G protein, which activates further downstream signalling cascades (Lehoux and Tedgui 2003).
- Receptor tyrosine kinases are membrane proteins that work as secondary messengers, activated by G proteins, whose major role is in integrin-mediated signalling; it also induces the activation of mitogen-activated protein kinases (MAPK) (Wang and Thampatty 2006).
- Mitogen-activated protein kinases (MAPK) is an important pathway that leads from mechanical forces to gene expression and protein synthesis (Lehoux and Tedgui 2003).
- Stretch-activated ion channels, whose activation allows the movement of ions such as Ca^{2+}, Na^{+} and K^{+} inside the cell. For instance, the level of Ca^{2+} in a cell regulates processes such as cell growth, cell motility, contraction, apoptosis (programmed cell death), differentiation (Wang and Thampatty 2006).

The response of vascular cells to mechanical stimuli, in particular, is the modulation of the synthesis of the majority of the ECM components, like collagen,

elastin, enzymes such as matrix metalloproteinases (MMPs) and growth factors (Gupta and Grande-Allen 2006).

The sequence of events that lead to vascular remodelling as a result of these stimuli is shown in *Figure I.10*.

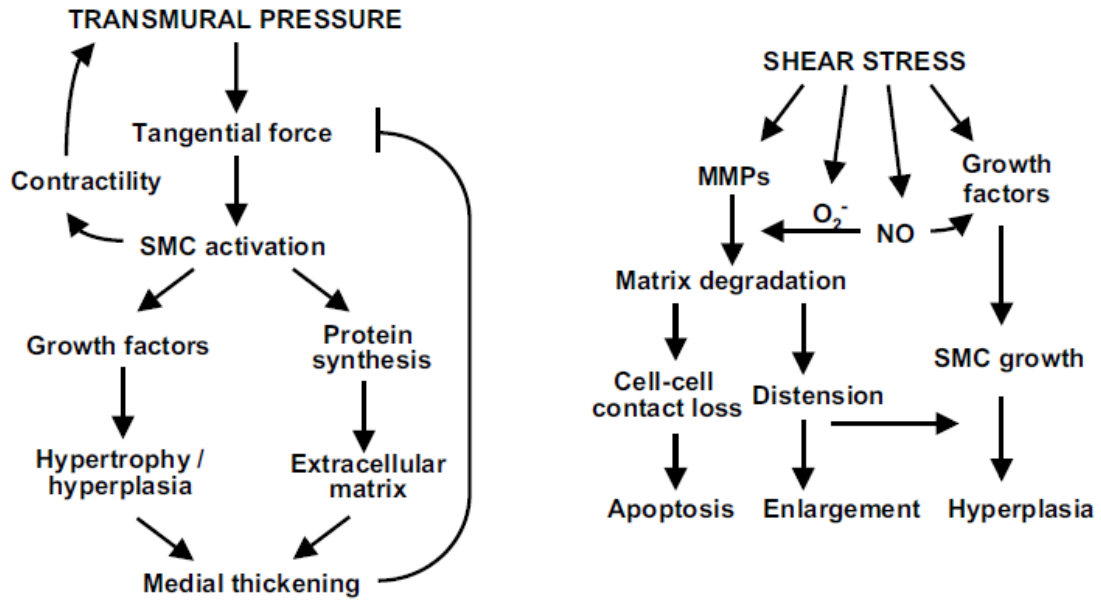

Figure I.10 – Sequential events that, from increased transmural pressure or shear stress, lead to vascular remodelling. Reproduced with permission from (Lehoux and Tedgui 2003).

Wang *et al*. (Wang and Thampatty 2006) provide an extensive review of the main mechanotransduction effects for different cell types. In particular, results of experimental studies on endothelial cells and SMCs subjected to static and cyclical stretches and strains were reported.

Cyclic mechanical stretching on endothelial cells have been shown to provoke cell reorientation, actin cytoskeleton remodelling and affect the productions of MMPs and DNA; cyclic stretches on SMCs would increase the production of collagen, proteins in general and proteoglycans, and regulate MMPs and mRNA (Wang and Thampatty 2006).

In order to examine the relationship between cellular mechanotransduction effects and stent design it is necessary to describe the changes which occur in the mechanical environment of the vessel due to stent implantation. The final section of this review provides an overview of the application of numerical modelling to examine the links between stent design, structural and fluid dynamic stresses and biological response.

1.6 MODELS OF STENT-VESSEL INTERACTION

Considering ISR as an excessive healing response to the injury of the vessel during stent implantation, the study of the mechanical interaction between the stent and the vessel can give a useful insight to the focal mechanical environment where the neointimal growth takes place. In particular, numerical modelling techniques allow study of the behaviour of the device and the loads it needs to bare during and after its deployment, giving an indication on the properties it needs to have for it purpose. Modelling techniques can also predict changes in the solid mechanics and fluid dynamics induced by the presence of the stent and therefore the creation of a situation prone to ISR. Specific features include the magnitude of the stresses in the vessel due to its radial compression by the stent struts and its circumferential stretching (Timmins, Miller et al. 2011) and the change in the dynamics of the blood flow (Chiu, Chen et al. 2004). However, as for any model, assumptions and simplifications are required according to the final aim of the simulation. Therefore, model validation is essential in order to be able to interpret the results (Morlacchi and Migliavacca 2013).

Stent/vessel interaction models have been used to examine structural mechanics, fluid dynamics and drug elution. Many commercial and non-commercial

software packages allow simulation of the mechanical behaviour of structures under a specific load and the flow in defined geometries with specified boundary conditions, though the use of finite element analysis (FEA or FEM, finite element method). This method has been used to explore the disturbance of physiologic blood flow by the stent and the influence of stent design on their expansion, either freely or in a more or less complex model of a vessel.

The following section describes particular strategies to represent vessel/stent interaction in different studies, according to the final aim of the simulation.

- **Stent only**

Some studies aim to evaluate the best methodology to create stent models, to reduce computational resource requirements and still obtain valuable results. De Beule *et al*. explored different model implementations for the study of free stent expansion, deploying a stent through three different scenarios: applying an increasing pressure directly on the inner surface of the stent; through a radial displacement-controlled expansion of a cylindrical balloon; through a trifolded balloon expanded with an increasing pressure. The aim of this study was to evaluate how changes in the final expansion are due to the various simplifications such as the final expanded shape of the stent, the ability to capture features such as the typical transient dog-boning effect given by the pattern of the balloon expansion and the pressure needed for the deployment. The result is that, while the first scenario results in an unrealistic fusiform expanded shape of the stent, the second scenario provides an accurate representation of the final expanded shape of the vessel; the third is also able to capture features such as the typical transient dog-boning effect given by the pattern of the balloon expansion and provides data on the pressure needed for the

deployment, at the cost of considerable computational power (De Beule, Mortier et al. 2008).

However, most of the computational studies with stents aim to improve the understanding of ISR causes and mechanisms; consequently, the simulations need to include the vessel, either with an idealised or complex model, in order to evaluate stent and vessel interaction.

- **Idealised artery, simplified stent design**

To investigate specific issues relating to stent performance, a simplified and controllable environment in which to expand the stent model aids interpretation of the results. Whilst such models will not represent the complexity of the nature of individual atherosclerotic lesions, the use of an idealised artery allows clear comparison of the effects of two different stent designs.

Timmins *et al*. created a model of a thick straight cylinder to represent a healthy porcine artery, in order to compare the effect of a high-stress and a low-stress stent. These represent two commercial stents for which the design was imported from CAD data and computationally implanted by applying a pressure in the artery and subsequently releasing it onto the expanded stent (Bedoya, Meyer et al. 2006). This allowed comparison of the stress imposed by the two designs with the restenosis observed in an *in vivo* porcine model of restenosis where the corresponding stents had been implanted. The results show that a higher amount of hyperplasia has been generated by the implantation of the high-stress stent (Timmins, Miller et al. 2011).

A similar approach has been used in a study by Chen *et al*. to analyse the effect of mis-sizing the stent on the fluid dynamics, the consequent wall shear stress and circumferential wall stress. A straight cylinder was used to represent the artery,

while the stent was reconstructed from a pattern that is typical of some commercial stents (J&J Cordis Bx Velocity and Guidant-Boston Scientific Multi-link Penta). Model results were then compared with data obtained from stented pig models. Correlation has been found between both fluid and structural stress and neointimal growth, but more significant relation has been found between the combinations of some of these values, like the ratio of circumferential wall stress and wall shear stress, and neointimal growth: this suggests that the variation of fluid dynamics and the stresses imposed on the wall by the presence of the stent have a simultaneous effect of the ISR (Chen, Sinha et al. 2011).

The use of an idealised artery geometry corresponds to representing a healthy vessel: this is not only simpler to model, but also allows a closer comparison of the results with experimental studies, where stents are implanted into healthy porcine arteries, so they do not contain atherosclerotic disease prior to stent implantation.

- **Idealised artery with presence of a plaque, idealised stent**

In some studies the complexity of the model is increased by refining either the stent or the vessel model. Takashima *et al*. report model refinement aimed at a more accurate evaluation of the contact area between the struts and the vessel. This was addressed within their model as the presence of a plaque was also taken in consideration, although plaque and vessel geometry was still idealised in order to be reproducible both experimentally and computationally. More specifically, the objective was to evaluate the influence of stent design, particularly between high or low number of cells and links. The results show that a higher number of cells and links increases the contact area and consequently decreases the stress concentration, and could decrease the stimulus for ISR (Takashima, Kitou et al. 2007).

- **Realistic arterial geometry from image data, idealised stent**

The use of a realistic arterial geometry model could be particularly useful to evaluate the effect of a specific treatment on a specific patient. This scenario was considered by Gijsen *et al*. through the use of biplane angiography and intravascular ultrasound to reconstruct the geometry of a mildly stenosed coronary artery and obtain a 3D model of the vessel wall. Models of a commercially-available unexpanded stent with various strut thicknesses were deployed in the artery in order to evaluate the deformation patterns and stress distribution in the artery of the specific patient. The peak stresses in the arterial wall were found in the locations behind the stent strut and where the wall was thinner (*Figure I.11*); the peak stresses for the stents were found close to the connectors between the struts (Gijsen, Migliavacca et al. 2008).

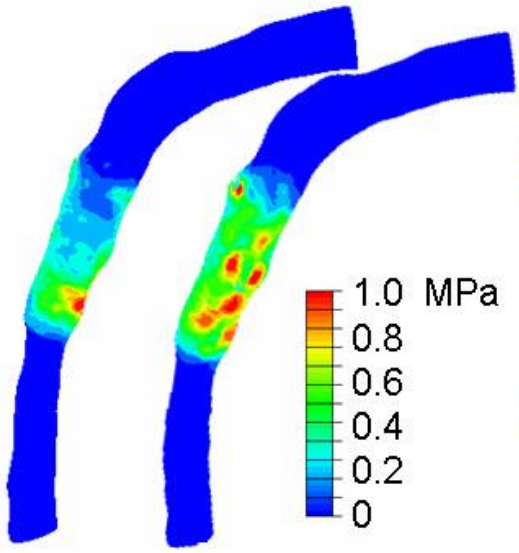

Figure I.11 - Simulation of stent-vessel interaction: von Mises stress in the vessel model. Adapted with permission under Creative Commons Attribution Licence from (Gijsen, Migliavacca et al. 2008).

- **Ideal artery, realistic stent**

A feature that is really difficult to capture by computational simulation of stent deployment is the real deployed geometry of the stent. Under ideal conditions,

within a straight cylinder and a uniformly distributed expansion pressure, the deployed stent has an even symmetric cylindrical shape. Stent expansion in a real vessel leads to uneven, asymmetric final geometry, with a transient dog-boning effect (Wang, Liang et al. 2006), prolapse of the vessel (Prendergast, Lally et al. 2003) and changes in local blood flow, like spatial WSS distribution (Morlacchi, Keller et al. 2011). In a study by Morlacchi *et al*., a realistic 3D model of a stent implanted in an *in vivo* porcine model was reconstructed from micro-CT images. A FEM simulation was used to create the final vessel geometry using an idealised initial vessel geometry to obtain the vessel lumen geometry for a computational fluid dynamics (CFD) simulation. This allowed a comparison between the fluid dynamics post stenting and the biological response through examine of the correlation between low wall shear stress values and the magnitude of ISR (Morlacchi, Keller et al. 2011).

SUMMARY

Whilst angioplasty with stenting aims to re-open a stenosed artery and restore sufficient blood flow to the downstream tissues (the heart, in case of coronary arteries), in-stent restenosis remains a common negative outcome.

Over the last decades evolution in stent design, materials and drugs has attempted to improve outcomes for patients, but in some cases, where the rate of restenosis is reduced, thrombosis constitutes another problem.

Evidence of a correlation between the change in the local mechanical environment and the incidence of ISR has been found and is explained by the mechanotransduction mechanisms that govern the cell cycle, the synthetic capabilities and the signalling functions of cells. Many studies attempt to analyse the magnitude of these changes through finite element modelling (from both a structural and fluid dynamic point of view) in an attempt to describe the situation immediately after stenting. In some cases the outcomes of modelling studies have been directly compared with results from experimental and *in vivo* models.

The next Chapter will analyse the physiological mechanical stimuli that a healthy vessel has to sustain and how these change in the presence of a stent with the aid of a simple MATLAB model. Chapter 2 also provides an overview of the small number of recent computational models in literature that attempt to describe the evolution of ISR under the influence of these structural and fluid dynamics stimuli.

CHAPTER II – INTRODUCTION TO ISR MODELLING

INTRODUCTION

In Chapter 1 the stenting procedure and the consequent problem of in-stent restenosis have been introduced, with the subsequent importance of having a better understanding of the factors contributing to this phenomenon. The brief review of mechanotransduction mechanisms provided in Chapter 1 shows the complexity of these effects and the need to approach the study of ISR from multiple points of view, including both mechanical and biological aspects. Finally, some examples of stent-vessel interaction models were presented to provide an overview of the literature related to this problem.

This Chapter focusses on the problem of modelling the relationship between the mechanical stimuli and the biological growth in ISR. In Section 1 the physiologic mechanical stimuli in a healthy vessel and the changes following stent implantation are described, to show how such changes might contribute to the regulation of neointimal growth. In Section 2 the problem of how to represent the mechanical properties of arteries is discussed and two examples of models commonly used to describe their behaviour, linear elastic and hyperelastic, are presented. Section 3 provides an estimate of the significance of the change in the mechanical environment of the vessel after a stent expansion through a simple mathematical model. This simple model will be refined in the following Chapters

for a detailed analysis of structural effects of stenting on ISR. Finally, in Section 4 a review of existing models of the evolution of tissue growth during ISR identifies how the various stimuli described in Section 1 have been represented by other authors, to explore specific hypotheses.

2.1 MECHANICAL ENVIRONMENT OF HEALTHY AND STENTED VESSELS

This thesis will not consider the influence of vessel disease on the interactions between the stent and the vessel. The motivation of this study is to inform numerical models of ISR using data from an *in vivo* porcine model of ISR (Gunn, Arnold et al. 2002, Dean, Morton et al. 2005). In this porcine model the ISR, response is generated by inducing a more or less severe injury in a healthy coronary artery by intentionally over-sizing the stent; at a chosen time-point after stenting, the animal is sacrificed in order to remove the stented vessel and analyse the eventual ISR with various techniques such as histology (Malik, Gunn et al. 1998).

Porcine models are commonly used to study human diseases of the cardiovascular system, in particular for coronary arteries. The suitability of this animal model has been established due to the similarity between the two systems in terms of anatomy, branching and blood supply of coronary arteries (Sahni, Kaur et al. 2008). In particular, porcine coronary stenting is considered the model of choice for the study of ISR because of the close resemblance with human restenosis. This has allowed detailed study of the early reactions to stenting, in particular the events occurring between the first 24 hours and 1 month (Schiele 2005). Experimental porcine studies (Gunn, Arnold et al. 2002) provide more controlled data and extra possibilities for measurement of vessel anatomy and the neointimal growth over a series of time-points.

The advantage of investigating the biological response to stent implantation with such an approach is that the data can provide a better understanding of the contribution of mechanical stimuli without the additional variability introduced by

the pre-stenting disease of the vessel. Such data provide a powerful validation tool for computational studies (Tahir, Hoekstra et al. 2011, Timmins, Miller et al. 2011).

What happens in clinical reality is much more complicated, as the vessel is not healthy but atherosclerotic, with the presence of a plaque obstructing the blood flow and with mechanical properties dependent on its components.

Modelling the experimental studies of ISR on pigs introduces less complexities and unknown variables: the animal is healthy and a stent is inserted and over-expanded with the aim of creating a damage that could be associated with the damage provoked in the clinical case (Gunn, Arnold et al. 2002).

The introduction in Chapter 1 to mechanotransduction mechanisms occurring in a vessel to maintain its physiologic functions shows how both structural and fluid dynamic stimuli generate a reaction from the vascular cells. This section aims to provide a description of the main mechanical loads healthy vessels are subjected to, and how these change with the presence of a deployed stent. As previously described, changes in mechanical loads from typical physiological values can trigger compensatory biological responses, which, through receptors on the surface of cardiovascular cells, induce them to adapt their synthesis of ECM molecules, resulting in ECM remodelling (Gupta and Grande-Allen 2006).

Healthy vessel, pre-stenting

Coronary arteries are constantly subject to mechanical forces, even in their normal healthy state, due to their function of supplying the heart muscle with oxygenated blood. These mechanical forces can be summarised as follows:

- Cyclic changes in pressure

The blood, whilst flowing through the artery, exerts a pressure in the radial direction, perpendicular to the vessel wall, which tends to distend the vessel. The circumferential tension is borne across the vessel thickness (Lehoux and Tedgui 2003). The mainly affected cells are SMCs, which undergo cyclic tensile strain due to the hoop strain of the vessel and compressive strain due to the thinning of the wall in the radial direction (Gupta and Grande-Allen 2006). Changes in pressure have been shown to increase SMC size and collagen and elastin production (Lehoux and Tedgui 2003). All the cells within the vessel wall undergo these cyclic strains at each heartbeat at a pulsatile frequency of around 1 Hz in humans (Gupta and Grande-Allen 2006). In the porcine case the heart rate is higher, almost double at 112±35 beats per minute (bpm) (Stankovicova, Szilard et al. 2000)

- Pulsatile changes in shear stress

The friction of the blood on the endothelium results in a stress that is parallel to the direction of the flow, the shear stress (τ), which is dependent on the blood viscosity and velocity gradient at the wall (Lehoux and Tedgui 2003). Shear stress is mainly experienced by ECs (Gupta and Grande-Allen 2006). Physiologic values of wall shear stress (WSS) vary within the circulatory system, with an average around 0.1-0.6 Pa in the venous system and values around 1-1.5 Pa or higher in the arteries (Mongrain and Rodes-Cabau 2006). Endothelial cells have been shown to react differently to different ranges of WSS, with a protective effect in the presence of normal or high values of WSS (Mongrain and Rodes-Cabau 2006).

Blood flow in arteries is often computed using Poiseuille's law, which describes the pressure drop for a constant laminar flow of a Newtonian fluid, through a pipe of constant circular cross-section and a length considerably higher than the

diameter. The equation, $\Delta P = \frac{8\mu L Q}{\pi r^4}$, can be used for flows whose variation in time is slow enough to be assumed steady state. In other cases, the Womersley number is used to evaluate the relative effect of transient inertial force and viscous force: $W_0 = R_0\sqrt{\frac{\rho\omega}{\mu}} = R_0\sqrt{\frac{\omega}{\nu}} = \frac{transient\ inertial\ force}{viscous\ force}$. With a very small Womersley number (<1), the inertial force is negligible and the velocity profile is approximately parabolic, while for higher numbers the inertia of the fluid generates a delay between the phase of the pressure gradient and the oscillation of the velocity profile, which has a significant influence on the shape of the velocity profile.

- Axial pre-stretch and circumferential residual stretch

The vessel is subject to an *in-vivo* axial pre-strain of around 40-60% (Dobrin 1990, Cardamone 2009). The result of a physiological axial strain is the presence of a pressure-invariant axial force, which means that the axial force needed to maintain the axial stretch constant is independent of the internal pressure (van den Broek, van der Horst et al. 2011).

The presence of a circumferential residual stretch of the vessel is observable in its load-free state by cutting the vessel in the longitudinal direction. Following the cut, the vessel will assume an open configuration, with the opening angle used to describe the undeformed reference configuration of the artery. This residual stress results in an homogenization of the stress through the thickness and an increased arterial compliance (Driessen, Bouten et al. 2005).

Axial pre-stretch and circumferential residual stretch combine to determine the mechanical behaviour of the coronary artery, as illustrated in *Figure II.1*.

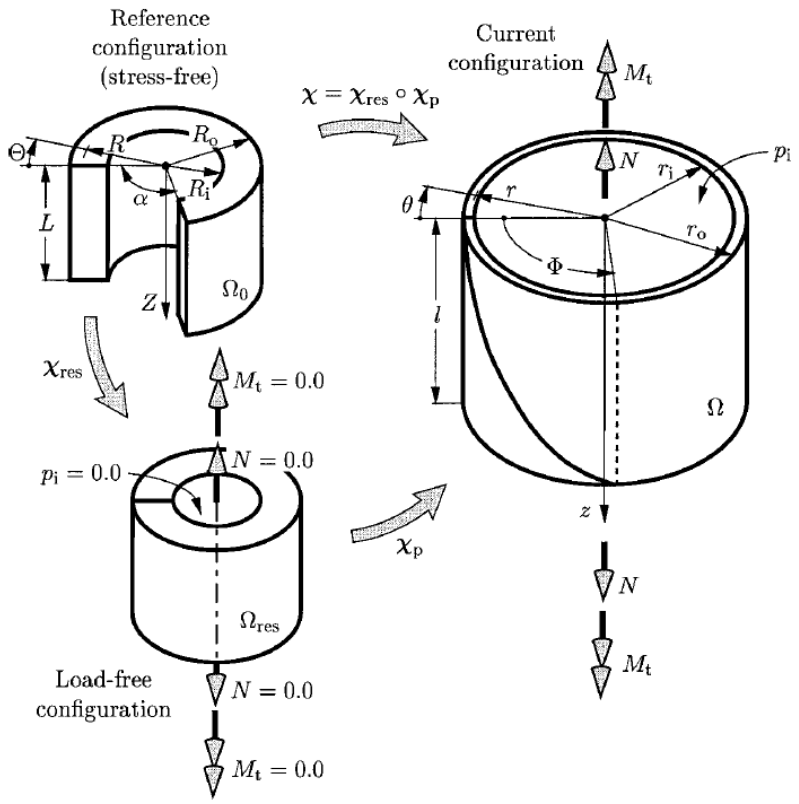

Figure II.1 – Arterial ring in the (stress-free) reference configuration Ω_0, the load-free configuration Ω_{res} and the current configuration Ω. Reproduced with permission from (Holzapfel, Gasser et al. 2000).

For the purpose of this thesis, the effects of axial pre-stretch and circumferential residual stretch are neglected: the models used in the following Chapters are kept simpler, as the focus is more on the local effects of stent/vessel interaction.

Stented vessel

Following stent implantation, the presence of the stent struts disrupts the mechanical environment of the arterial wall more than the angioplasty alone, with the introduction of a permanent structure interacting with the vessel (Moore and Berry 2002). Once a stent is deployed, a series of changes in the mechanical loads immediately affect the vessel, demonstrated schematically in *Figure II.2* where the pre-stented vessel is shown as a uniform cylinder; these are discussed in more detail below.

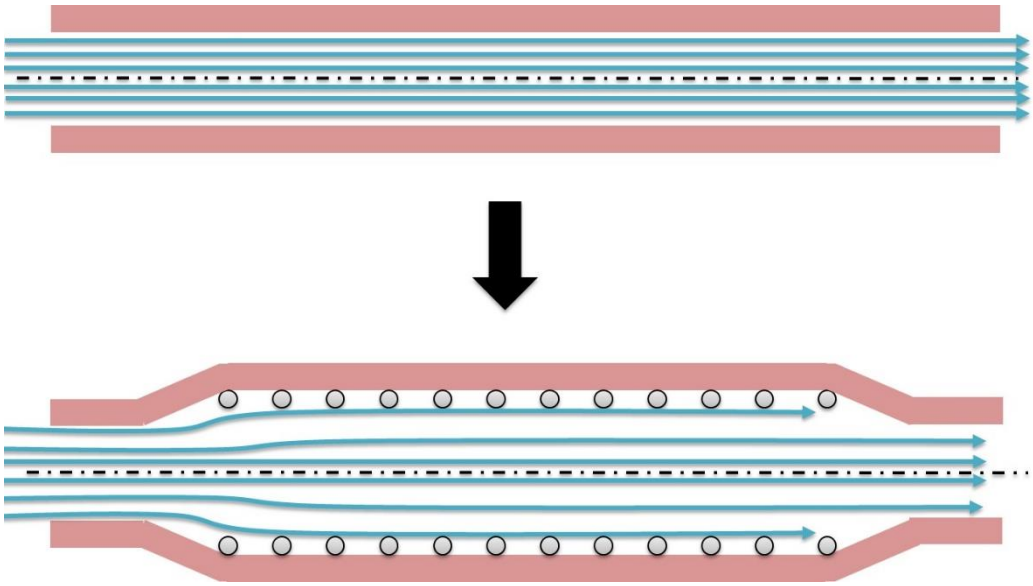

Figure II.2 - Schematic representation of the effect of stenting: the stent struts push the tissue radially, creating local compressive stress at the struts, tensile stress between the struts and changing the shear stress acting on the vessel wall.

- Radial forces due to angioplasty and stent implantation

In order to deploy the stent, push any coronary plaques against the vessel wall and obtain plastic deformation of the stent struts, the balloon is inflated inside the coronary artery at pressures up to 15 atm (more than 100 times the average blood pressure of 100 mmHg). After this, the balloon is removed and the stent imposes a contact stress on the vessel wall at the stent struts. This stress acts to prevent recoil of the vessel wall, with the purpose of maintaining the lumen aperture reached during angioplasty (Moore and Berry 2002). As a consequence, a high compressive stress is localised in the region behind the stent struts (Boyle, Lennon et al. 2011).

- Circumferential stretch

The aim of stent implantation is to restore physiological blood flow by obtaining an expansion of the artery, which results in considerable circumferential tension in the vessel wall. This high hoop stress has been shown to be the highest in magnitude,

usually representing the first principal stresses of a stented artery (Timmins, Miller et al. 2011).

- Variation in shear stress

The presence of an expanded stent in a vessel has an effect on the blood flow, not only in the region local to individual stent struts, but also in the overall fluid dynamics (Moore and Berry 2002). The change in fluid dynamics following stent deployment results in a variation in the wall shear stress sensed by the vascular cells. As introduced in Chapter 1 changes in wall shear stress have been shown to influence the regulation of cellular activity. In particular, an inverse correlation has been observed between neointimal proliferation, leading to ISR, and WSS (Mongrain and Rodes-Cabau 2006).

- Compliance mismatch

Introducing a metallic cylindrical structure into the artery creates an interaction between two entities with very different material properties. In particular, compliance mismatch between the non-stented artery and the stented region has been shown to result in changes to blood flow dynamics and generate a considerable stress concentration at the ends of the stent (Berry, Manoach et al. 2002).

2.2 VESSEL MATERIAL MODELS

Arteries have a long history of study, from a variety of perspectives: morphology, physiology, anatomy, mechanical properties (Ozolanta, Tetere et al. 1998). Initially, studies used animal models and then progressed to humans. With the introduction of computational models, the analytical description of the behaviour of vascular tissue has become of increasing importance. As introduced in Chapter 1, the evolution of

computational power provides increased potential for the definition of more accurate and more complex models. If a computational model is well validated, it constitutes a powerful tool to better understand complex phenomena and to compare the use of various devices in a controlled environment, providing savings in material costs and time compared with *in vivo* and *in vitro* experimental tests.

The constitutive equation used to describe material behaviour represents the relationship between an imposed stress and its response in terms of the resulting strain. The mechanical behaviour of a blood vessel can be described in more or less detail appropriate to the focus of the study, and may include heterogeneity, incompressibility, residual stresses, smooth muscle contractility and pressure-related dynamic wall motion (Vito and Dixon 2003).

An important choice when dealing with a blood vessel is whether to treat it as homogeneous, for which locally averaged properties can be assumed, or heterogeneous, with the introduction of the influence of the different components to the resulting material properties, which constitute a network of SMCs, elastin and collagen fibres. For example, describing a material as isotropic means assuming that its response to a load will be the same no matter which direction the load acts, while taking into consideration the orientation of the fibres of a vessel means recognising its anisotropy (Holzapfel and Ogden 2010).

A feature that is very typical of soft biological tissues is their hyperelastic behaviour; the remainder of this section outlines the distinction between elastic and hyperelastic constitutive models.

Linear elastic model

The simplest constitutive law to describe the behaviour of a material is with a constant elastic Young's modulus or modulus of elasticity, defined as the slope of the stress-strain curve in the elastic region. The elastic Young's modulus describes elastic deformation of the material along an axis when a force is applied along the same axis *x*:

$$E = \frac{\sigma_{xx}}{\varepsilon_{xx}}$$

where E is Young's modulus, σ_{xx} is the stress and ε_{xx} is the strain, for an uniaxial load. As arterial composition and structure is different at each level of the arterial tree, experimental data for elastic moduli specific to the coronary arteries are required to produce a model of these vessels.

Even with such data, the elastic properties of the vessels are observed to change during the lifespan of a person, becoming more rigid with time, even in absence of any specific disease. This evolution in vascular properties with time was studied by Ozolanta et al. (Ozolanta, Tetere et al. 1998) who reported changes in mechanical properties, biomechanical constituents and wall structure of the human coronary arteries with age and sex, in subjects without any reported pathology. Stretching tests were performed on cylindrical sections of the left (LCA) and right (RCA) coronary artery of groups of people of different ages. The tangential elastic modulus varied from 1.06 MPa for the right artery of neonates (<1 year old) to 4.11 MPa for the left artery of the oldest group (> 60 years old). *Table II.1* summarises the results of these tests, divided by age group and coronary artery section.

Table II.1 - Tangential elastic moduli [MPa] of left and right coronary arteries of six groups of people of different ages. Data adapted with permission from (Ozolanta, Tetere et al. 1998).

Age groups	<1	1-7	8-19	20-39	40-59	60-80
LCA	1.17±0.41	1.12±0.26	0.9±0.48	1.57±0.58	2.19±0.74	4.11±0.89
RCA	1.06±0.24	1.64±0.28	1.22±0.68	2±0.78	2.08±0.64	2.85±0.76

Hyperelastic models

The mechanical behaviour of coronary arteries is more complex than a linear stress/strain relationship. This is caused by the inherent complexity of the vessel wall which is comprised of many different constituents. These can be divided into a cellular component responsible for the active properties, mostly smooth muscle cells (SMCs), and the extracellular matrix (ECM) whose major components are elastin and collagen. The elastin and collagen are both proteins synthesised by SMCs and have a predominant role in determining the passive mechanical properties of the artery (Roy, Boss et al. 2010).

Elastin has rubber-like characteristics with a low elastic modulus of around 0.4 MPa (Dobrin 1978) and the ability to sustain large deformations (Kalita and Schaefer 2008). Its fibres are organised into concentric sheets that constitute layers of the media; this structure provides the compliance necessary to bear load at low pressures, including the physiologic cyclic blood pressure (Roy, Boss et al. 2010).

Collagen is the responsible for the non-linear elastic behaviour of blood vessels, with an elastic modulus that increases with strain and varies between around 10 and hundreds of MPa (Kalita and Schaefer 2008). Its elementary units, procollagen fibres, are organised in wavy bundles distributed in the media. When physiological pressures are applied to the artery, most of the load is borne by the

elastin while the collagen straightens and incrementally takes up load, increasing the total mechanical properties of the artery, as shown in *Figure II.3.b* (Roy, Boss et al. 2010).

Smooth muscle cells are oriented in the circumferential direction of the artery and play a role in the constriction of vessels under physiologic conditions, called vasomotion (Kalita and Schaefer 2008). This effect acts to either reduce the vessel lumen or to prevent excessive dilation, but their presence contributes little to the passive material properties of the vessel wall when inactive (Dobrin 1978).

Figure II.3.a is a schematic representation of these three components, while *Figure II.3.b* plots results of experimental tests and a fitting model showing the change of stiffness of the artery wall with increasing strain, due to the reaction of first elastin and then collagen.

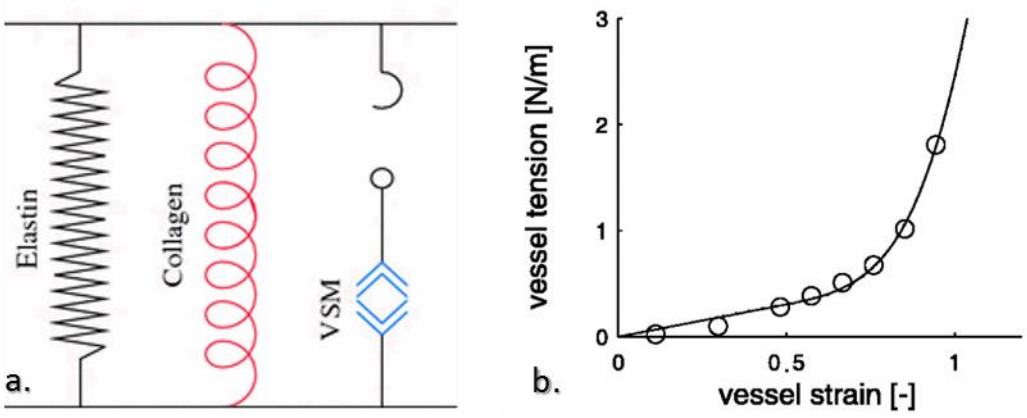

Figure II.3 – (a) Schematic representation of the parallel arrangement of collagen and elastin. Vascular smooth muscle is neglected in the passive state. Reproduced with permission from (Roy, Boss et al. 2010). (b) Curve describing the behaviour of arteries, through experimental data (dots, rat small arteries) and a fitting model: the first reaction is due to load bearing by the elastin, giving a less stiff response; when the collagen is recruited, the stiffness increases. Adapted from (VanBavel, Siersma et al. 2003), permission was not required.

In order to represent this arterial strain-stiffening non-linearity, a Strain Energy Density Function (SEDF) approach is commonly used to relate the strain energy of the vessel to its deformation. SEDF are commonly used for biological tissues: they

can be used for materials that exhibit hyperelasticity and path independence between the initial and final states. A benefit of this approach is the ease of writing the stress-strain law as a single scalar function (Vito and Dixon 2003).

A typical Strain Energy Density Function is given by *Equation 1* in terms of the strain invariants for an isotropic hyperelastic material:

$$\boldsymbol{W(I_1, I_2, I_3) = \sum_{i,j,k=0}^{\infty} a_{ijk} \cdot (I_1 - 3)^m (I_2 - 3)^n (I_3 - 3)^o}$$

$a_{000} = 0$, a_{ijk} are the hyperelastic constants and I_1, I_2, I_3 are the strain invariants, which can be defined as:

$$I_1 = \lambda_1^2 + \lambda_2^2 + \lambda_3^2; \qquad I_2 = \lambda_1^2\lambda_2^2 + \lambda_1^2\lambda_3^2 + \lambda_2^2\lambda_3^2; \qquad I_3 = \lambda_1^2\lambda_2^2\lambda_3^2$$

where λ_1, λ_2 and λ_3 are the principal stretches of the material (Maurel 1998). An example of values that have been used in previous studies for coronary arteries is

$$U = 0.04 \cdot (I_1 - 3) + 0.003 \cdot (I_2 - 3)^2 + 0.085 \cdot (I_2 - 3)^3$$

which generates a stress-elongation curve that is similar to curves obtained by experimental tests on arterial tissue (Gijsen, Migliavacca et al. 2008).

This section has introduced both linear elastic and hyperelastic models for arterial behaviour. In the following section a simple model of stenting is introduced which uses a linear approximation to estimate changes in the mechanical environment of the artery following stent deployment, with data based on experimental tests found in literature. Hyperelastic models of the artery are discussed in further detail in later Chapters.

Due to the structure of the arteries, with collagen fibres helically wound in their circumferential direction, blood vessel tissues can show anisotropic behaviour, with

different reactions for loads in different directions (Holzapfel, Gasser et al. 2000). A number of material models have been developed to include the anisotropic behaviour (Vito and Dixon 2003); however, this aspect has been not been considered in this thesis.

2.3 A SIMPLIFIED REPRESENTATION OF CHANGES IN MECHANICAL STIMULI IN CORONARY ARTERIES FOLLOWING STENT DEPLOYMENT

From a purely mechanical point of view, the effect of a stenting procedure can be described as an increase in the radius of a section of a vessel. Even small changes in the geometry of the vessel can provoke a considerable difference in the stimuli that are sensed by the cells. Although this simplification does not take in account the complex phenomena occurring at the areas at the ends of the stent, where the diameter of the vessel suddenly changes, it can represent the mechanical behaviour in a more central area of the stented vessel, as illustrated schematically in *Figure II.4*. In this region the flow is expected to be more developed and the influence of the structural bending effects on the vessel wall due to the end of the stent will be less significant.

This section describes a simple MATLAB model which was developed to provide a gross estimate of the magnitude of these effects, including the variation of both the fluid dynamic and structural environment through changes in the velocity profile and resulting shear stress at the wall and structural stress and strain in the circumferential, radial and axial direction within a thin-walled cylinder.

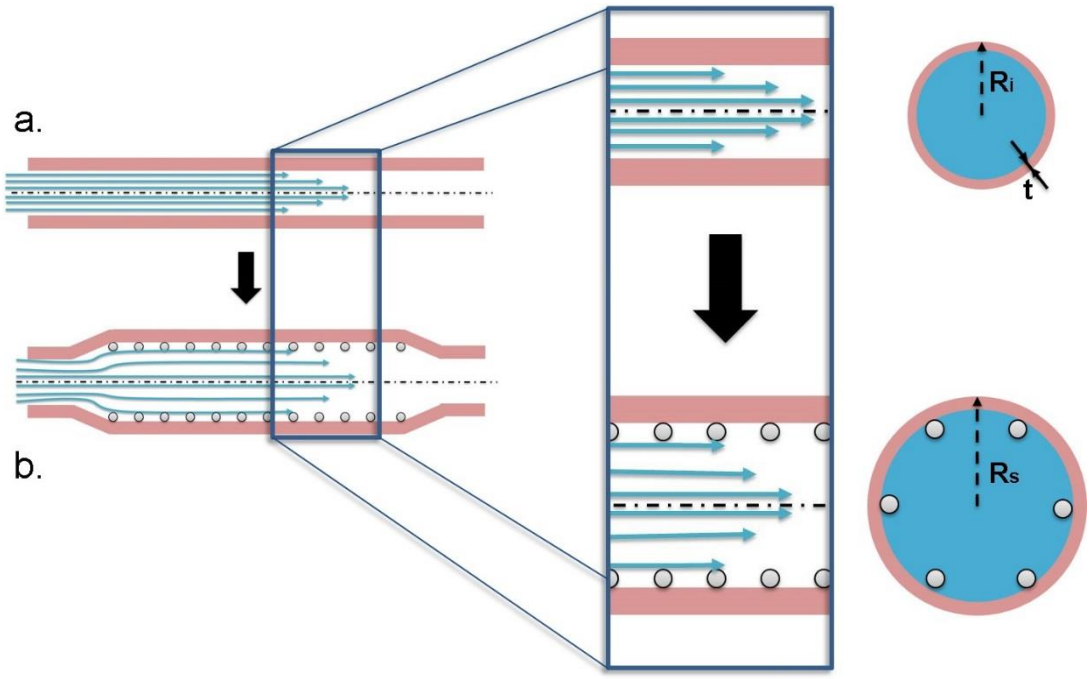

Figure II.4 - Representation of the vessel before (a) and after (b) stenting. The zoomed area shows the area considered in the model. R_i and R_s indicate the initial radius and the post stenting radius, t is the thickness of the vessel.

Methods

Deformation caused by stent deployment: The initial vessel geometry (*Figure II.4.a*) and a set of pressure and flow conditions are used to compute the fluid dynamic and structural stimuli acting on the vessel wall prior to stent deployment. The stent deployment is assumed to increase the vessel radius from R_i to R_s by an expansion ratio defined by R_s/R_i:1. The change in geometry shown in *Figure II.4.b* is used to compute the change in fluid dynamic and structural stimuli following stenting. The detail of the fluid dynamic and structural mechanics equations, and associated assumptions, is provided in the following sections.

An initial vessel radius of 1.4 mm is assumed, measured as the value of the lumen of a right porcine coronary artery *in vivo* from pre-stenting angiography images, while the thickness was imposed to be of 0.1 mm (Keller, Amatruda et al.

2014). An expansion of 1.4:1 was assumed, to provide results representative of the porcine stent expansion experiment (Morlacchi, Keller et al. 2011).

Fluid Dynamics: The velocity profile and wall shear stress in a straight vessel can be calculated for varying radius. The value of radius following stent deployment, R_s, can be altered to represent different stent expansion ratios. The value of flow is assumed to remain constant after stent expansion, which is consistent with what happens *in vivo* due to the vaso-regulation of the blood vessels (Tahir, Bona-Casas et al. 2013). The blood can be treated as a Newtonian fluid for tubes with diameter bigger than 1 mm, which is the case for the vessels taken in consideration (Huo, Choy et al. 2009).

Blood at 37° normally has a viscosity, μ, of 3-4 centipoise (cP), which corresponds to 3-4×10^{-3} Pa·s: for this model blood viscosity was assumed to be μ = 4e-3 Pa·s (Cheng, Lai et al. 2004). The blood is incompressible (Poisson's ratio: ν = 0.5), the flow is laminar and is represented in a straight tube with constant radius; for this geometry Womersley number is equal to *0.72* (<1), so for simplicity Poiseuille flow was assumed.

The velocity is considered constant in time and a no-slip condition for the blood in contact with the wall means that the velocity in that point is zero, generating a parabolic velocity profile, with the peak velocity at the centre of the lumen. This can be described as $v_r = v_{max}\left(1 - \frac{r^2}{R^2}\right)$. The velocity is calculated from a value of flow in coronary arteries of 50 ml/min typical of values reported in the literature (Huo, Choy et al. 2009).

The shear stress τ is computed from the velocity profile as $\tau = \mu \cdot \frac{dv}{dy}$.

Structural Mechanics: Prior to stent deployment the vessel experiences a physiologic pulsatile tensile stress, which can be calculated assuming the coronary artery is represented by a thin wall cylinder. The thin-walled assumption is commonly used for structures where the wall thickness is less than one-tenth of the radius. A linear elastic material model is used to compute the relationship between stress and strain through $\varepsilon_\vartheta = \frac{\sigma_\vartheta}{E}(1-\nu^2)$; in this case a Young's modulus of 1 MPa was chosen (Ozolanta, Tetere et al. 1998).

During the cardiac cycle the blood pressure is assumed to vary between 80 and 120 mmHg. Given that the vessel wall is assumed to be thin, the corresponding hoop stress is assumed to be constant across the vessel wall and can be calculated as $\sigma_\vartheta = \frac{PR_i}{t}$, where P is the pressure, R_i the radius of the unpressured vessel and t the thickness. The hoop strain is $\varepsilon_\vartheta = \frac{\sigma_\vartheta}{E}(1-\nu^2)$, where $\nu = 0.5$ as the vessel is assumed to be incompressible. R_i was calculated to make sure that the radius of the artery would be R_o = 1.4 mm with the imposition of an average blood pressure of 100 mmHg. A plane strain condition, $\varepsilon_z = 0$, is considered, which means that the vessel is constrained at its ends; the axial stress is calculated as $\sigma_z = PR_i/2t$. The radial stress corresponds to $\sigma_r = -P/2$ on the centreline of the vessel and the radial strain is calculated through $\varepsilon_r = \frac{1}{E}\left(\sigma_r - \nu(\sigma_\vartheta + \sigma_z)\right) = -\frac{1}{E}\nu(\sigma_\vartheta + \nu\sigma_\vartheta) = -\nu\frac{\sigma_\vartheta}{E}(1+\nu)$, as the radial stress is assumed to be small compared to the other two components.

During stent expansion a high pressure is exerted by the inflating balloon onto the stent in order to generate plastic deformation of the stent struts and increase the lumen radius. The resulting stress acting on the coronary artery will depend on the cyclic pressure variations over the cardiac cycle before stent expansion and on the reaction force between the stent and the vessel after the expansion. In this case it

is assumed that that the cyclic pressure does not change the stress between the vessel and the stent, as the stent effectively shields the vessel from changes in pressure. This simple model assumes that stent expansion is a displacement-driven process, which means that the final expansion radius is defined. The final expansion radius is used to compute the final hoop strain of the vessel, through $\varepsilon_\vartheta = \frac{R_s - R_i}{R_i}$ and consequently the hoop stress is $\sigma_\vartheta = \varepsilon_\vartheta \cdot E/(1-\nu^2)$.

Results

Fluid Dynamics:Figure II.5.a shows the velocity profiles for an expansion ratio from 1 to 1.4. The green line represents a ratio of 1 (unstented vessel) and the red line represents a ratio of 1.4. The results demonstrate how small changes in vessel radius have a strong impact on the velocity of the blood, with 50% reduction in peak velocity for a 40% increase in radius.

Figure II.5.b shows the results of the shear stress along the normalised radius (r/R) as it varies with the expansion rates. The peak value is at the vessel wall and this value decreases significantly with a small change in the radius of the vessel. The wall shear stress varies considerably with a 40% increase of radius, with peak values, which correspond to the area in contact to the surface of the inner vessel, that reduce by more than 50%.

Structural Mechanics: Figure II.6 shows the stresses and strains generated by the cardiac cycle and after the stent expansion. Being an expansion of a cylinder, it is expected that the highest stress generated is hoop stress, which comes from the resistance of the vessel to the stretching of the tissue in the circumferential dimension. The axial stress is generated by the reaction to the shortening of the vessel, as it is constrained at its ends; the radial stress is small compared to the other

two components, constituting less than 5% and 10% of hoop and axial stress respectively: these proportions are valid also after expansion. The deployment of the stent in the vessel at time 5 s, modelled as the equivalent increase in radius, generates stresses that are 4.6 times higher than during the cardiac cycle, with a value of hoop stress that is around 766 kPa. The radial strain is the same magnitude as the hoop strain, but with opposite sign: this is because ν = 0.5, $\varepsilon_r = -\nu\frac{\sigma_\vartheta}{E}(1+\nu) = -\frac{3}{4}\frac{\sigma_\vartheta}{E}$, and $\varepsilon_\vartheta = \frac{\sigma_\vartheta}{E}(1-\nu^2) = \frac{3}{4}\frac{\sigma_\vartheta}{E}$. With the expansion, the strain goes from 12.5% to 57.4% accordingly to their sign.

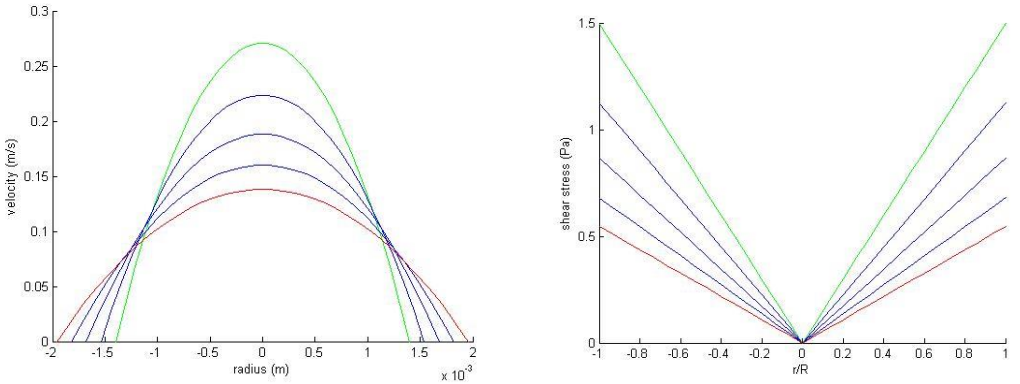

Figure II.5 – a. Velocity profile for various lumen expansions. The green line represents the unstented vessel, the red line represents a stenting with a ratio of 1.4:1. b. Shear stress for different lumen expansions. The green line represents the unstented vessel, the red line represents a stenting with a ration 1.4:1.

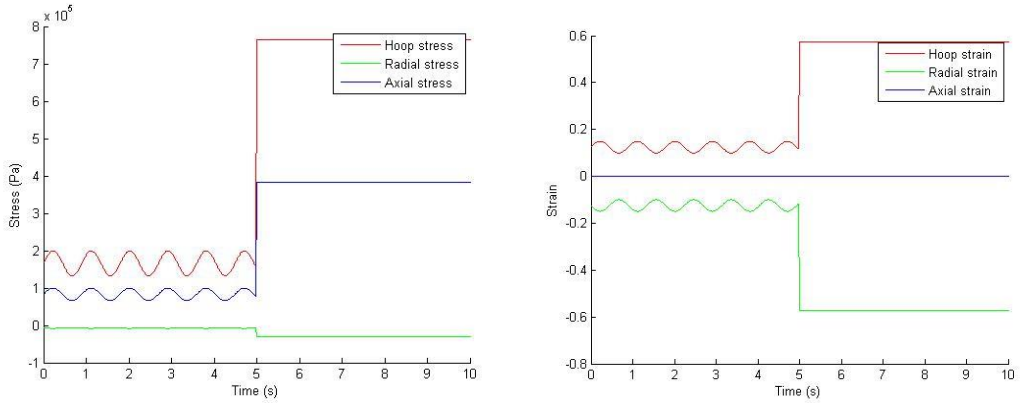

Figure II.6 – Hoop (red), radial (green) and axial (blue) stress (left) and strain (right) in a vessel before and after the stent expansion, which occurs at time 5 s.

Discussion

This simple MATLAB model is able to capture some features of the variation of mechanical stimuli acting on a vessel before and immediately after stent implantation. As discussed earlier in this Chapter, this study will focus on the changes due to stent implantation within a healthy vessel, appropriate for model validation with data from porcine models of ISR. A computational simulation of this kind of test allows investigating more accurately the influence of a single parameter, like the effect of expanding the same stent to different final radiuses, as reported in this model.

As previously reported, the cells are particularly sensitive to change of loads, both in form of WSS and structural stress, generating a series of mechanotransduction mechanisms.

This simple model will be used for two purposes in this thesis:

i) To clarify the nature of the stimuli that have been considered by other authors when considering the evolution of ISR.

ii) To provide a reference framework to examine more complex structural effects resulting from stent/artery interactions and how these might change during the development of ISR, as explored in Chapter 3, 4 and 5.

More detailed reports of the variation of structural and fluid dynamics post-stenting have been reported in the literature, as described in Chapter 1. In this Chapter, the assumptions used to compute WSS magnitude do not capture the complexity of a stented vessel; a more detailed investigation of fluid and structural mechanics within a 3D geometry immediately post-stent implantation is reported in Chapter 4 of this

thesis. Chapter 3 and 5 of this thesis focus on the development of 2D models to describe local stress concentrations in the region of the stent struts and the evolution of the structural environment of the vessel during the development of ISR.

Development of models of ISR has been the focus of a number of recent studies, which aim to model not only the immediate effect of stenting, but also the evolution of ISR based on mechanical stimuli. The final section of this Chapter provides an overview of these studies with reference to the concepts explored in the simple MATLAB model.

2.4 MODELS OF EVOLUTION OF ISR

Several recent studies have developed models of ISR evolution using one or more of the mechanical stimuli described in the previous section. In addition to mechanical effects, biological parameters also inform such models including features such as the cell cycle. As described at the end of Chapter 1, the use of computational models provides a detailed description of the mechanical environment the artery is subject to, which, with appropriate assumptions, allows estimation of the level of injury to the vascular tissue (Gijsen, Migliavacca et al. 2008). Moreover, the computational power can be essential to predict the response of the tissue to these stimuli: in fact, ISR is a very complex phenomenon that occurs on multiple scales. The spatial scale ranges from the smooth muscle cell dimension, which can be as small as approximately 30 μm in diameter, to the vessel dimension, which is typically around 1.5 mm of radius for a coronary artery; for the temporal scale, the orders of magnitude vary from seconds for stent deployment to hours for cell division to weeks for ISR development (Evans, Lawford et al. 2008). As such, multi-scale models are essentials to represent even just a part of such complexity.

To represent the behaviour of the biological components and the mechanics of the system a number of modelling approaches have been employed in literature. For the cellular components of the system the most commonly used technique involves the development of a discrete approach, such as an agent-based model (ABM) (Evans, Lawford et al. 2008, Tahir, Bona-Casas et al. 2013) or a lattice-based approach (Boyle, Lennon et al. 2013). For the macroscopic tissue-level properties a continuum approach, such as the finite element method (FEM), is often used to study the grade of injury as a result of tissue stress and strain (Zahedmanesh and Lally 2012, Boyle, Lennon et al. 2013). Exchange of information between the cell-level and tissue-level representations, based on rule sets derived from mechanotransduction hypotheses, is employed to link these representations to provide a model for cellular evolution.

The review that follows details how previous studies have broken down the complexity of problem and modelled components of the system with different techniques, through the use of appropriate hypotheses. In fact, a representation including all components of the system in detail and all biological and physical variables would not only be extremely computational expensive, but would also introduce uncertainty in the initial conditions for the model and make interpretation of the results challenging. To avoid this, previous studies tend to focus on specific stimuli, to improve their representation in the model and aid the interpretation of the results.

The main aspects taken into consideration in this review are:

- Source of the mechanical stimuli considered:

  Structural (e.g. von Mises stress), Fluid dynamic (e.g. wall shear stress)

- Dimension of the model domain (e.g. 2D / 3D)
- Biological components described (e.g. VSMCs / ECM / IEL)
- Types of computational models (e.g. Continuum / ABM / lattice-Boltzmann)
- Focus of investigation (e.g. effect of strut thickness on neointimal growth)

A recent paper by Boyle et al. (Boyle, Lennon et al. 2013) describes the application of an ISR model to the evaluation of clinically used stents within an idealised 3D artery. The stimulus taken into consideration is structural, specifically, the von Mises stress of the vessel is used to calculate fatigue-induced damage to the tissue; fluid dynamic effects were not considered in this study. The stents are an idealised 3D representation of three commercially available stent designs, which are deployed into the vessel model. The constituents of the vessel represented are smooth muscle cells (SMCs) and extracellular matrix (ECM).

The models interacting in this study are:

1. Injury model: a 3D finite element analysis performed using ABAQUS (SIMULIA) is used to compute the vessel stresses following stent deployment, using a hyperelastic isotropic model for the arterial tissue. The resulting stresses are used to calculate the damage accumulation in the artery, relating the rate of damage formation, dD/dt, to the von Mises stresses using constants σ_0 and σ_f, which represent the boundaries of stress below which no damage accumulation occurs and above which the failure strength is reached, respectively.
2. Inflammation model: ordinary differential equations are used to model the response to injury in terms of tissue degradation, through matrix degrading factors whose production is dependent on the amount of injury, and growth

factor production, that is linearly related to the damage and decays exponentially with time.

3. SMCs activity model: cells occupy a lattice-based structure and phenotype regulation, proliferation, migration and ECM production are included. The cell phenotype is defined using a score that represents the status between fully contractile and fully synthetic; this score is dependent on the local concentration of ECM. Proliferation is regulated by contact-inhibition and the local presence of growth factors.

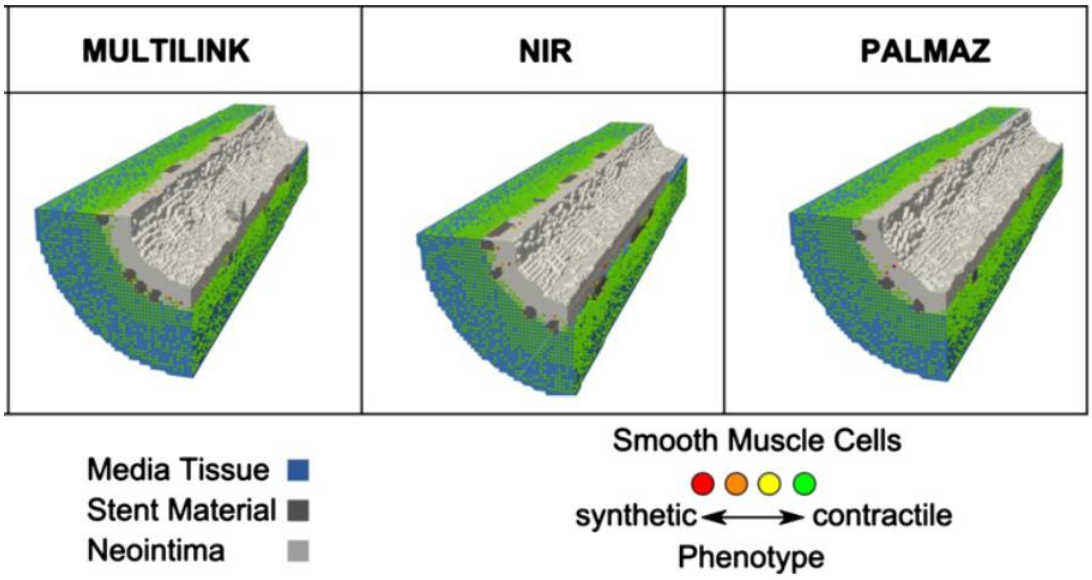

Figure II.7 - A plot of 1/8 of the lattice models at the end point of the simulation. Adapted with permission from (Boyle, Lennon et al. 2013).

The resulting neointimal growth predicted by this model for the three types of stent is shown in *Figure II.7*. The differences between the ISR generated by the three different types of stent are similar to what was observed *in vivo*. The sensitivity of the model to stent design was found to be influenced by the value chosen for the inflammatory response parameter, which relates the amount of the matrix degrading factor produced to the injury level.

Zahedmanesh et al. (Zahedmanesh, Van Oosterwyck et al. 2012) developed a model of ISR with the aim of evaluating the influence of the expansion ratio and of stent strut thickness to the neointimal formation process. The model is 2D axisymmetric and comprises a continuum FEM developed in ABAQUS to determine the injury of the vessel immediately after stenting and an ABM for the SMCs which includes an algorithm for ECM degradation and production. The biological response is compared between two different stent designs, with thin and thick struts, and for three expansion ratios of a single stent design.

The models interacting in this study are:

1. Injury model: the stent is simulated as a rectangular rigid stent strut displaced into the vessel, which is modelled with homogeneous hyperelastic material properties, within a FE analysis. The post-stenting damage is calculated from the von Mises stress as a value between 0 and 1 with a sigmoid function, where 0 is assigned to stresses lower than the physiological blood pressure (120 mmHg) and 1 is assigned for stresses higher than the ultimate tensile strength of the medial layer (252 kPa). The damage value is calculated at the centroid of each finite element and reported in a matrix that corresponds to coordinate points for the cellular model.
2. ABM lattice-free model: the biological components represented include SMC migration and proliferation, ECM concentration, represented by its collagenous constituent, and EC proliferation. The model defines relationships between the values of the damage matrix and the behaviour of the SMC at each coordinate point. High damage stimulates matrix-degrading metalloproteinases (MMPs) synthesis, which cause ECM degradation and reduction of the damage value at the following model iteration. SMCs are

initially in a contractile phenotype, but they switch to synthetic if collagen density in ECM is below normal; migration and proliferation have random directions and contact inhibition is set to avoid superimposition. A SMCs switches back to contractile if either, it finds itself close to ECs, the local ECM value becomes normal again or maximum VSMC density is reached.

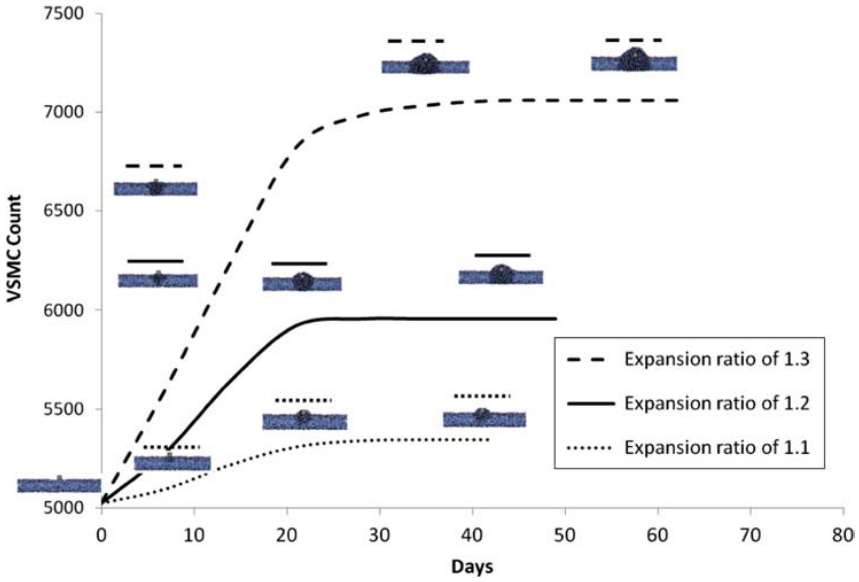

Figure II.8 – The evolution of the model for different stent expansion ratios. Reproduced from (Zahedmanesh, Van Oosterwyck et al. 2012), permission was not required.

Figure II.8 shows results from the study which compare the different expansion ratios for a single stent strut geometry. The influence of the factors considered on the development of ISR was evaluated in terms of the total final SMC count and re-endothelialisation time. Increasing the expansion ratio from 1.1 to 1.3 produced a non-linear increase in maximum von Mises stress, the final SMC count rose up to 40% more than the initial state and the time for complete re-endothelialisation increased from 3 to 6 weeks. Increase in strut thickness resulted in an increase in final SMC count; as a result, this factor was identified as a possible independent predictor of ISR.

Tahir *et al*. (Tahir, Bona-Casas et al. 2013) report a multi-scale model of ISR which uses contact inhibition between SMCs and WSS thresholds as the main regulators of the biological response. The model is applied to investigate the influence of the presence or absence of a functional endothelial layer on the evolution of neointima. The fluid dynamics are represented as they evolve with tissue growth through the tracking of the vessel lumen. The vessel is not modelled using a continuum approach, but is composes of layers of densely packed agents, representing smooth muscle cells. The structural forces are calculated by means of potential functions (Caiazzo, Evans et al. 2009) and there is no extra-cellular matrix. The model domain is described in two dimensions, specifically the longitudinal section of the system, and the stent is represented by a square strut displaced into the agents which form the vessel wall.

The models interacting in this study are:

1 ABM lattice-free model: The vessel wall (SMCs and IEL) deformation is modelled using agent-agent potentials. The deployment of the stent is simulated by pushing two square struts into the vessel; the endothelium is assumed to be completely removed by the balloon angioplasty, while IEL rupture represents an index of the injury of the wall and is dependent on strut penetration. The position of the cells at each time-step is computed from equilibrium between cell-cell attractive and repulsive forces and the frictional force of the blood flow.

2 Lattice-Boltzmann flow simulation: steady state flow in the domain is simulated, assuming that the blood volume flow remains constant throughout the development of ISR, due to vaso-regulatory effects. The flow simulation is used to compute the magnitude of wall shear stress acting on each agent in contact with the blood flow.

3 Cell-cycle model for SMCs: cells behave according to their state, which can be quiescent, growth or mitotic and depends on their cycle and a set of conditions such as wall shear stress and contact inhibition. At the end of each cell state update, information about the new domain is sent to the flow processor for a new simulation.

4 Re-endothelialisation: different initial percentages of coverage of ECs are chosen to represent different levels of injury and a probability function of EC migration and proliferation based on data found in literature establishes its expansion. The ECs are not directly included in the ABM as it is assumed that the thin endothelial layer does not influence the WSS, which is directly sensed by the first layer of SMCs. The WSS on the ECs regulates the production of nitric oxide (NO), which can affect the SMC cell cycle leading towards quiescent state: an increase in shear stress corresponds with a higher concentration of NO.

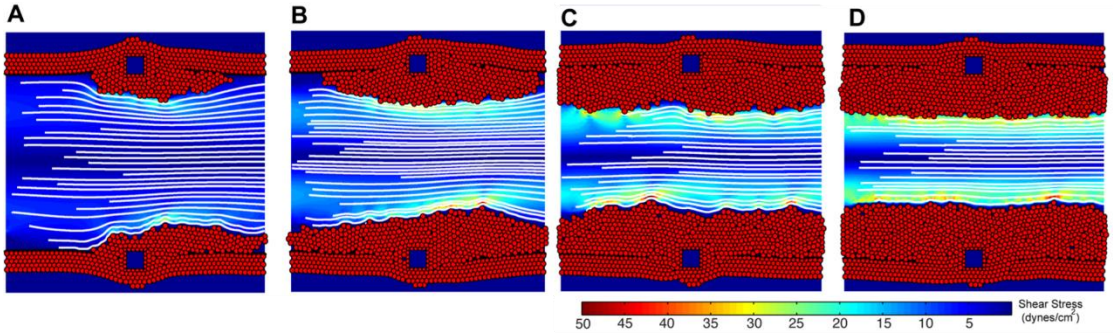

Figure II.9 - Evolution of ISR 50 days post stenting with 4 different hypotheses about NO release and re-endothelialisation: both fully effective within 15 days (A), NO fully effective within 23 days (B), full re-endothelialisation within 23 days (C) and old model where these effects were not considered (D). Adapted with permission under Creative Commons Attribution Licence from (Tahir, Bona-Casas et al. 2013), formatted horizontally for better representation.

The results of the simulations 50 days after stenting relative to four different hypotheses about NO release and re-endothelialisation are represented in *Figure II.9*. A positive correlation was found between stent penetration depth into the vessel and

the amount of ISR. In the cases where endothelial coverage is assumed to occur in the early stages (*Figure II.9(A)* and *Figure II.9(C)*), lower amounts of ISR were observed.

Discussion

Table II.2 summarises and compares the main characteristics of the studies presented in this section. One of main model features compared is the type of stimuli used to determine the neointimal growth, which can be distinguished between primarily structural mechanics (von Mises stress) in the case of Boyle *et al.* and Zahedmanesh *et al.* and primarily fluid dynamics (wall shear stress) in the case of Tahir *et al.* The structural stimulus captures the vessel stress immediately after stenting, whereas the fluid stimulus considers evolution of the wall shear stress with the ISR growth.

Table II.2 – Main characteristics of the reviewed ISR models. Glossary: SMCs = Smooth Muscle Cells, ECM = Extra-Cellular Matrix, FEM = Finite Element Model, ODE = Ordinary Differential Equations, ABM = agent-based model, LBM = lattice-Boltzmann method

	Stimuli	Elements	Models	Dim	Investigation
Boyle	Post-stenting von Mises stress	SMCs, ECM	FEM, ODE, lattice-based	3D	Comparison between stent types
Zahedmanesh	Post-stenting von Mises stress	SMCs, ECM, ECs	FEM, ABM lattice-free	2D	Influence of deployment diameter, strut thickness, re-endothelialisation
Tahir	Evolution of wall shear stress	SMCs, IEL, ECs	ABM, LBM	2D	Effects of re-endothelialisation and nitric oxide release

Another important distinction between these models is which constituents of the wall and the neointima they comprehend. Whilst all models consider the contribution of smooth muscle cells, not all studies include the influence of ECM and ECs on the evolution of restenosis. As introduced in Chapter 1, ISR is mainly due to the neointimal growth process, which consists of SMC migration, proliferation and ECM production. However, the presence of ECM contributes to the mechanical properties

of the neointima, which has an effect on the stimulus that was chosen in these two studies to model the restenosis process; however, in none of the two cases the production of new ECM is taken into account by updating the computation of the structural stimulus based on the regions of new tissue. This underlines the importance of continuing investigating through continuum models. Moreover, the constitution of a mature ECM might be essential to the stopping mechanism of ISR (Zahedmanesh, Van Oosterwyck et al. 2012), which is not yet completely understood.

The studies have been developed in both 2D and 3D, according to the complexity of the models developed and the focus of each study; while it was essential to have a 3D representation of the stent to compare different commercial stents (Boyle, Lennon et al. 2013), a comparison of the influence of stent strut shape can be analysed with a 2D model in the first instance (Zahedmanesh, Van Oosterwyck et al. 2012).

It should be noted that these models use a continuum model purely to inform the starting point for neointimal growth post-stenting. Once cells start proliferating, new extra-cellular matrix is produced and the neointima starts invading the lumen. The structure of the vessel undergoes a considerable change which may affect the resulting stresses. Although stress is considered to be a stimulus for tissue growth in these models, they are not able to follow evolution in structural stresses throughout the growth process.

This overview of ISR models shows the complexity of representing all phenomena occurring after a stent has been implanted, even considering the "simpler" case of ISR in a controlled animal model without the presence of disease.

In order to be able to analyse the outcomes of such studies the problem is broken down into smaller contributing elements and simplifications are necessary.

SUMMARY

Arteries constantly bear various loading conditions throughout a person's life, even in the absence of significant disease. Through systems of regulation, such as cell orientation and proliferation, arterial loads play a role in maintaining normal function. The presence of a stent dramatically changes the magnitude and distribution of stress imposed on the vessel; some studies which attempt to quantify these changes have been presented in Chapter 1.

One of the issues to face while attempting to model such a system is how to simplify the problem in order to obtain a stable, interpretable model whose outcomes are reliable. The choice of how to accurately represent the complex material properties of the arterial wall is related to the nature of the research question. The computational representation of experimental animal models offers a chance to reproduce the response of a healthy artery rather than a diseased one. The properties of diseased vessels are extremely variable and less well-known, and an easier validation of the results obtained on healthy animal models is reproducible or available in the literature.

The modelling of in-stent restenosis is inherently complex, as shown in the review of ISR models present in literature. It is accepted that both the change in wall shear stress and the structural damage provoked by the high wall stresses generated by the deployment of the stent play a role in the evolution of the neointimal growth, but the representation of all these factors in the same model remains challenging. The problem has been broken down in previous studies in order to consider specific factors, as yet these models do not describe the neointima using both "discrete" and "continuum" methods, which may be appropriate to consider cell and extracellular

matrix behaviour respectively. This problem will influence the structural stimulus considered in the evolution of the model: if structural stresses are believed to regulate the evolution of ISR, then the evolution of the geometry of the structure should be considered throughout the process, as it will influence the structural stress itself.

The aim of the next two Chapters is to build a structural model which is able to capture this evolution: Chapter 3 presents an explorative study of a 2D model of stent-vessel interaction, Chapter 4 studies the interaction through a 3D model while Chapter 5 describes a model to link stress distribution within the neointima with tissue growth.

CHAPTER III – 2D STENT/VESSEL MODEL

INTRODUCTION

In Chapter 2 a simple model of stent expansion in a vessel, represented by an even pressure in a cylinder, was presented. In this Chapter, the model is refined in order to represent the effect of the presence of the stent struts, both as local compression and as change in hoop stress. The first section of this Chapter considers the variation in loading following symmetric deployment of the stent struts into the vessel wall. To provide an estimation of the change in stress with the number of struts present in each section of the vessel, a 2D model of a transverse section is first developed analytically. The results of the analytical model are compared with a 2D finite element model which captures the detail of local stress concentration in the region of the strut itself, providing the distribution of the compressive stress under the strut. The second section of this Chapter develops a more realistic representation of a stented vessel section which considers an uneven distribution of stent struts. The strut distribution used for this model is based on observations from histological images of explanted coronary arteries. The Chapter concludes with a discussion of these results in the context of vascular injury due to stent implantation and the implications of this as a stimulus for neointimal growth.

3.1 DEVELOPMENT OF A SYMMETRIC MODEL OF STENT DEPLOYMENT

In the previous Chapter, a simple model of stent and vessel interaction was considered, with stent expansion represented by a pressure applied on the inner surface of the artery. Despite this considerable simplification, this model provides an estimate of the magnitudes of stresses acting on the vessel following stent deployment.

This 2D model can be improved by considering the presence of the stent struts rather than representing the expansion by a uniform pressure. The difference between the two models is represented in *Figure III.1*: a discrete number of struts are assumed to distend the vessel creating a polygonal shape, where the tissue between two struts becomes straight. It is expected that the two models will produce similar results as the number of stent struts increases and the polygonal shape approaches the circular shape resulting from expansion by a uniform pressure.

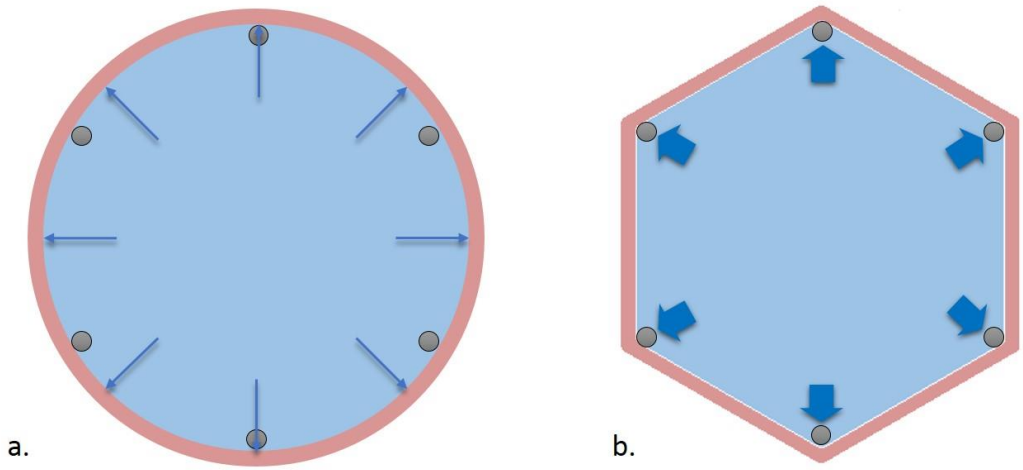

Figure III.1 - Different models of stent expansion, represented as a uniform pressure (a) and as a discrete number of stent struts pushing the vessel wall (b).

This discrete strut model can be represented using an analytical approach, allowing a large number of calculations to be performed to evaluate the influence of a particular

parameter on the results, for example, how the hoop stress changes as the number of stent struts varies. However, a finite element analysis provides a more detailed description of the stress variation, allowing inclusion of the effect of geometric and material non-linearity and capturing the detail of the distribution of the stresses along the circumference and through the thickness of the vessel.

This model is relatively simple compared to all the possible refinements of the representations of stent and vessel seen in Chapter 1, which report use of realistic 3D geometry, obtained through analysis of balloon unfolding (De Beule, Mortier et al. 2008) or from imaging data of either the vessel (Gijsen, Migliavacca et al. 2008) or the stent expanded in a vessel (Morlacchi, Keller et al. 2011). However, this model is similar in complexity to those used by several other authors to study the evolution of ISR from a multi-scale perspective, as discussed in Chapter 2 (Zahedmanesh, Van Oosterwyck et al. 2012, Tahir, Bona-Casas et al. 2013). As most of these models assume symmetric stent deployment, this section considers the variation of vessel stress under these conditions.

The following section describes the development of an analytical model within Matlab and a finite element model through ANSYS.

Methods

Matlab model: This model represents the cross-section of an artery, with the same properties as described in Chapter 2. The symmetric expansion is represented by a varying number of stent struts in order to analyse the effect of the transition from a homogeneous expansion, given by a pressure, to a discrete expansion. The initial vessel radius is R_i, and the stent struts are all displaced to a final radius of R_s; the expansion ratio is defined by R_s/R_i:1. The initial radius is 1.4 mm, the thickness of

the vessel, *t*, is 0.1 mm and the elastic modulus, *E*, is assumed to be 1 MPa. The Poisson's ratio is ν = 0.5, assuming incompressible behaviour of the tissue.

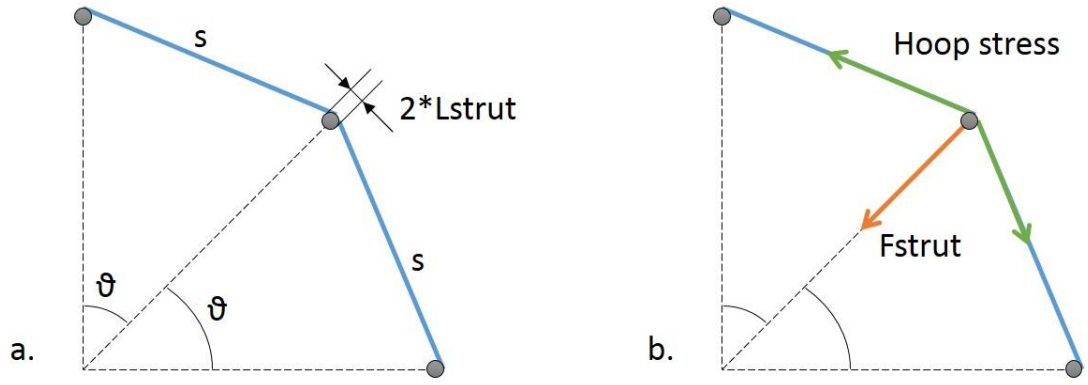

Figure III.2 – 1/4 scheme of the stent/vessel model developed in Matlab. a. Geometry of the model: ϑ represents the angle between two neighbouring stent struts, *s* is the segment connecting two stent struts; the dimension of the contact, *Lstrut*, correspondent to the radius of the strut. b. Direction of the main loads: the hoop stress acts along the vessel wall, while the reaction force to the strut is directed to the centre of the vessel.

The configuration of the vessel following stent strut contact is shown in *Figure III.2.a*: ϑ represents the angle between two neighbouring stent struts, *s* is the segment between them and *Lstrut* represents the dimension of the contact between the strut and vessel wall, assumed, for this model, to correspond to the radius of the strut. The expanded circumference of the vessel is given by the sum of the segments of vessel between the stent struts, where each segment length is given by $s = 2R_s \sin(\vartheta/2)$ as represented in *Figure III.2*.

For this model, the strain values will not be calculated as *engineering strain*, which corresponds to $\varepsilon = \Delta L/L_0$, but as *logarithmic strain*, which is commonly used for analysis of large deformations, given by $\varepsilon_{logarithmic} = \log(1-\varepsilon)$. This convention allows direct comparison with the ANSYS results, where logarithmic strain is used.

Figure III.2.b represents the main loads acting on the system: the hoop strain is calculated as $\varepsilon_\vartheta = \log(1 - \frac{C_{fin}-C_{in}}{C_{in}})$, while the hoop stress is given by $\sigma_\vartheta = \varepsilon_\vartheta \cdot$

$E/(1-\nu^2)$, and it acts along the vessel wall. The reaction force per unit axial length on the stent struts is directed toward the centre of the vessel; it can be calculated as the projection of half of the hoop stress on the two segments that are adjacent to the strut multiplied by the thickness of the wall: $F_{strut} = \frac{1}{2}\sigma_\vartheta(\sin(\vartheta/2) + \sin(\vartheta/2))t = \sigma_\vartheta \sin(\vartheta/2)\, t$. The radial stress given by the contact of the stent strut can be calculated from $\sigma_{strut} = F_{strut}/L_{strut}$, where L_{strut} corresponds to the contact region between the strut and the wall; in this case, it is assumed to be the radius of the strut, equal to 0.045 mm. A non-frictional contact is assumed between strut and wall.

ANSYS model: The geometry used for the Matlab model was generated in ANSYS Mechanical APDL version 14.0 (ANSYS Inc.) in order to explore different variables and parameters of a controlled simulation of stent expansion using a finite element approach, for comparison with the results of the analytical model. Vessel parameters were the same as for the Matlab model, with an initial radius of 1.4 mm and a thickness of 0.1 mm.

The vessel was again represented in cross-section and an assumption of symmetry was made. This allows only a fraction of the vessel to be modelled, according to the number of stent struts considered, *n*. Each fraction contains one stent strut and the angular extent of the model is given by 360/*n*. *Figure III.3* represents an illustration of a model with 6 stent struts: the mesh represented has a lower number of elements for clarity purposes.

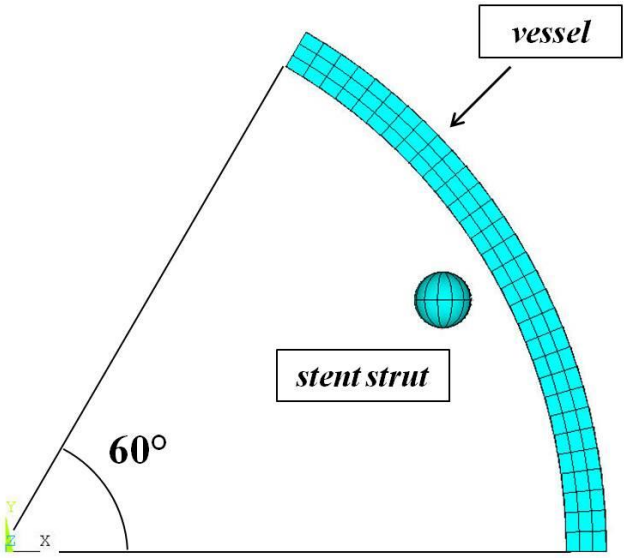

Figure III.3 – Scheme of a 2D finite element model of a section of a vessel and a stent with 6 evenly distributed stent struts. Symmetry is assumed and only a 1/6 section is simulated. The stent strut is a target element that gets in contact with the inner layer of the artery; the wall is composed of 2D plane elements. The figure only represents the type of elements used for the mesh, not the density used in the model.

To evaluate the influence of the vessel wall material model, the same simulations were performed with both a linear elastic and a hyperelastic material model. It is useful to understand how well the simple linear elastic approximation captures the variation in stresses during stent expansion to allow the results of the analytical model to be considered in the context of the more complex finite models described in the following Chapters. The linear elastic model has the same Young's modulus of 1 MPa as the Matlab model and Poisson's ratio of $\nu = 0.499$. The hyperelastic material model, described by a strain energy density function, was chosen based on previous computational studies (Gijsen, Migliavacca et al. 2008):

$$U = 0.04 \cdot (I_1 - 3) + 0.003 \cdot (I_2 - 3)^2 + 0.085 \cdot (I_2 - 3)^3 \quad [\text{MPa}]$$

where I_1 and I_2 represent the first and second invariants of the Cauchy-Green tensor; the coefficients are in MPa.

The stent was represented as a target element with a circular geometry with contact defined between this element and the inner layer of the vessel. The stent expansion was simulated by radial displacement of the stent strut towards the vessel, with vessel expansion occurring following initial contact between the stent strut and the vessel. For the comparison described in this section, four models were developed, constituted by a 1/6, 1/8, 1/10 and 1/12 symmetry, representing a cross-section with 6, 8, 10 and 12 struts, respectively (*Figure III.4*).

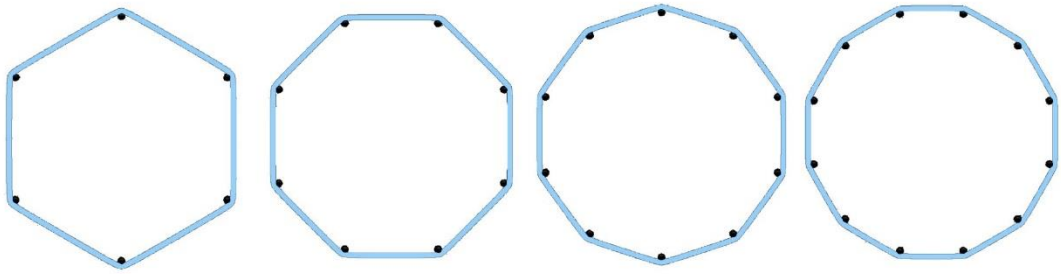

Figure III.4 - Expansions of symmetric models with 6,8,10 and 12 stent struts through finite element simulations.

The stent strut was assumed to have a radius of 45 μm, similar to the dimension of some clinically used stents, in particular the Biodivisio stent, which will be described in more detail in the next section and in Chapter 4.

For the vessel, 2D 4-Node Structural Solid (PLANE 182) plane elements were used, 32 through the thickness and 4 elements/degree along the circumference, resulting in 240, 180, 144 and 120 elements along the inner surface of the vessel with a total of 7680, 5760, 3840 and 2880 elements for the 1/6, 1/8, 1/10 and 1/12 symmetry models respectively. The stent strut was a circular 2D Target Element (TARGE169), which corresponds to a rigid body, while the corresponding contact at the inner surface of the vessel was modelled using 2D 2-Node Surface-to-Surface Contact elements (CONTA171). The mesh density was chosen after performing different sensitivity tests relative to the number of elements on the two directions of

the vessel, based on the strut stress detected through the thickness underneath the location of the stent strut. The 1/6 symmetry model was used, for a test-expansion similar to the one applied in this study. The number of elements was increased from 8 to 32 through the thickness and from 120 to 480 for the circumferential direction. The change in stress found at the node underneath the stent strut is 5% varying between 16 and 32 elements though the thickness, so the latter was chosen. For the circumference sensitivity, while the increase in stress is significant doubling the elements from 120 to 240, it becomes lower than 2% with further refinements, so 240 elements were chosen for the 1/6 symmetry model and the same proportion was kept for the other models.

Results

Matlab model: the results of the model are presented in *Figure III.5*. The first two plots (*Figure III.5.a*) represent hoop stress and strut stress for symmetric models with increasing number of stent struts, from 2 to 20, for four different expansion ratios, from 1.1:1 to 1.4:1. These show clearly how the number of struts has a significant effect on the reported stresses at the beginning of the curve, from 2 to 10, and how this effect is greater for bigger expansion ratios. The stresses are zero in cases where the deployed circumference, calculated as the sum of the segments between the stent struts, is not bigger than the initial circumference. The hoop stress ramps up quickly for the first part of the curve, but approaches a plateau with more than 10 struts. The strut stress value increases significantly up to 7 stent struts, reaching a peak, and then starts decreasing. The third and fourth plot (*Figure III.5.b*) show how the results approach those predicted for a uniform pressure expansion, represented by the straight line, as the number of stent struts approaches 200. The comparison for the hoop stress is made with the hoop stress calculated for a homogeneous pressure and

the same expansion ratio, from $\sigma_\vartheta = \varepsilon_\vartheta \cdot E/(1-\nu^2)$, with $\varepsilon_\vartheta = \log(1-\frac{R_s-R_i}{R_i})$. The strut stress is compared to the radial stress on the vessel wall, $\sigma_r = -P$.

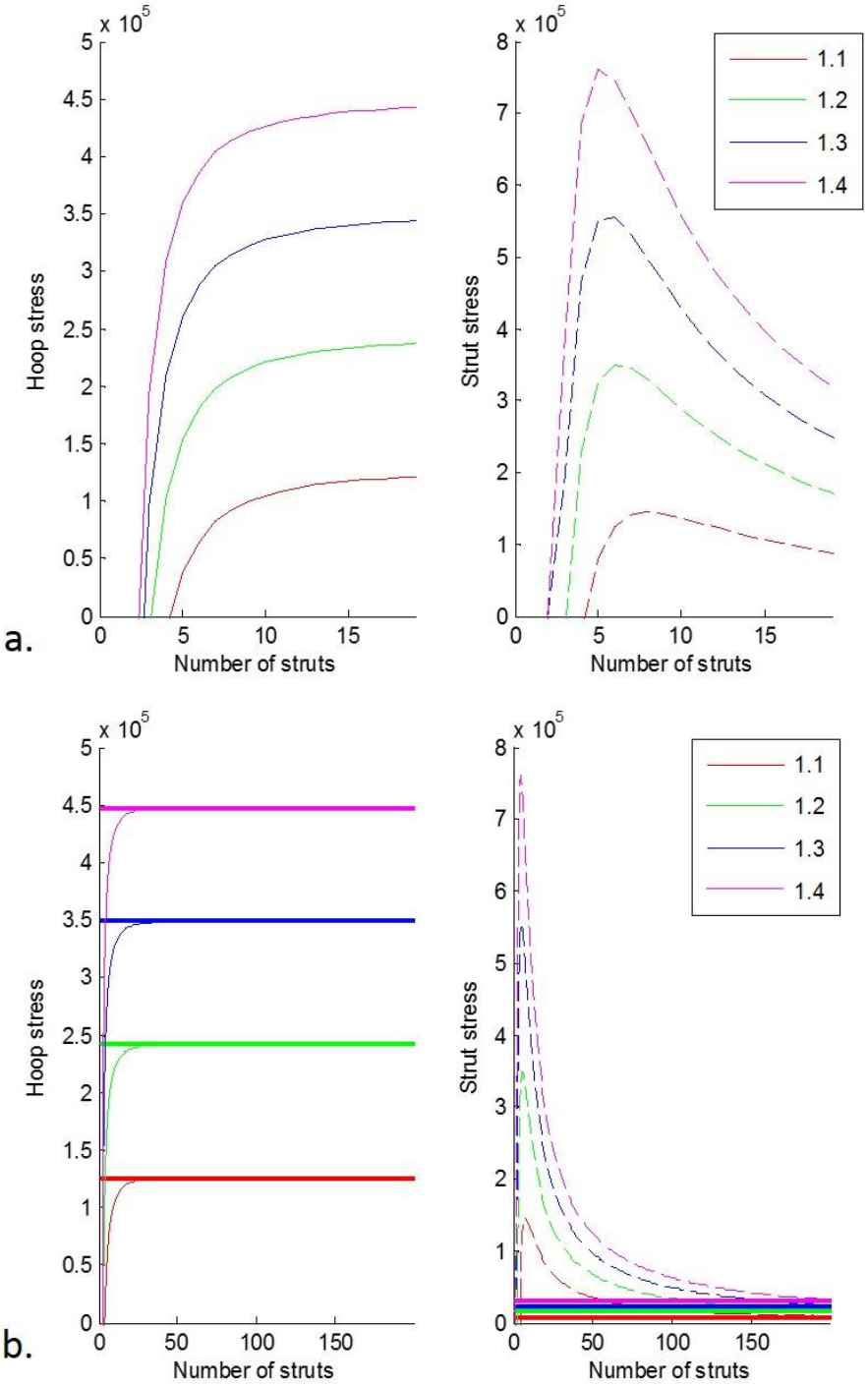

Figure III.5 - Hoop stress and strut stress calculated with increasing number of struts using the analytical model, presented for four different expansion ratios, from 1.1:1 to 1.4:1. a. Plots of hoop and strut stress for struts increasing up to 20. b. Plots of hoop and strut stress for struts increasing up to 200, compared with the pressure results (straight line).

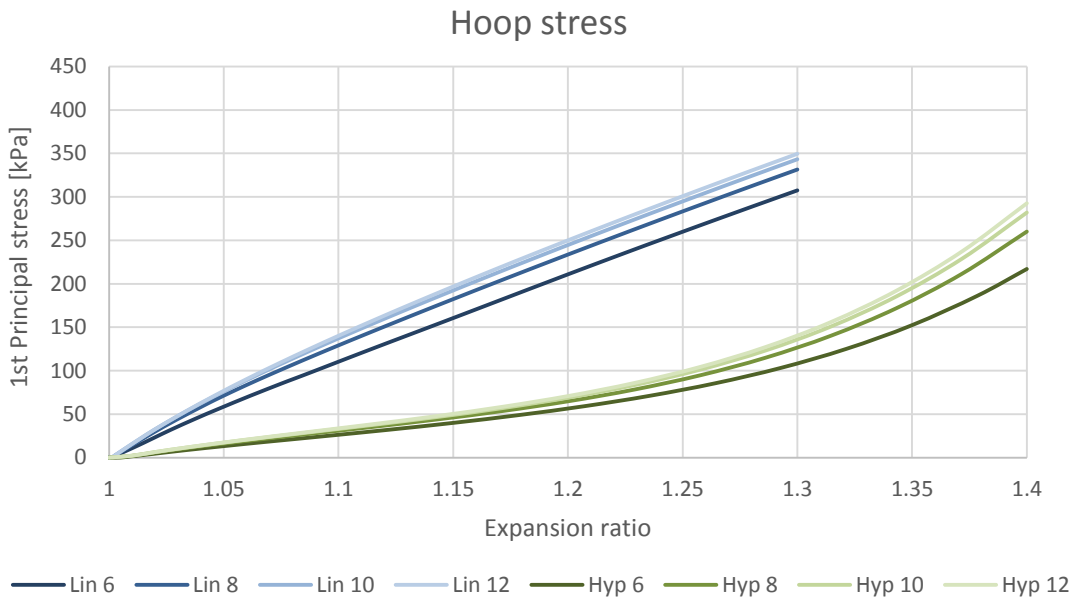

Figure III.6 – Different behaviour during expansion for the two materials chosen for the finite element models: hoop stress during the expansion for the linear elastic models (Lin: blue lines) and for the hyperelastic models (Hyp: green lines). The number in the legend indicates the number of stent struts for each model.

ANSYS model: Figure III.6 represents the results from the ANSYS solution for increasing expansion ratio. In particular, only the hoop stress was reported to illustrate the differences of behaviour of the two material models, linear elastic (blue lines) and hyperelastic (green lines). The results refer to a node on the inner surface located half way between two stents struts. It is noted that, due to convergence problems, only results for expansion ratios up to 1:1.3 are reported for the linear elastic finite element model.

Comparison between the analytical and finite element results: Results from the analytical model developed in Matlab and the finite element models developed in ANSYS are compared in *Figure III.7*, which reports the evolution of hoop stress and strut stress for increasing expansion ratio. *Figure III.8* and *Figure III.9* represent the change in hoop and strut stresses with increase in the number of stent struts, respectively. To provide a better comparison of the area where the biggest changes in the trend of the lines occurred for the analytical model, further simulations were

performed, using a linear elastic material and 15 struts and two hyperelastic models, with 4 and 15 struts.

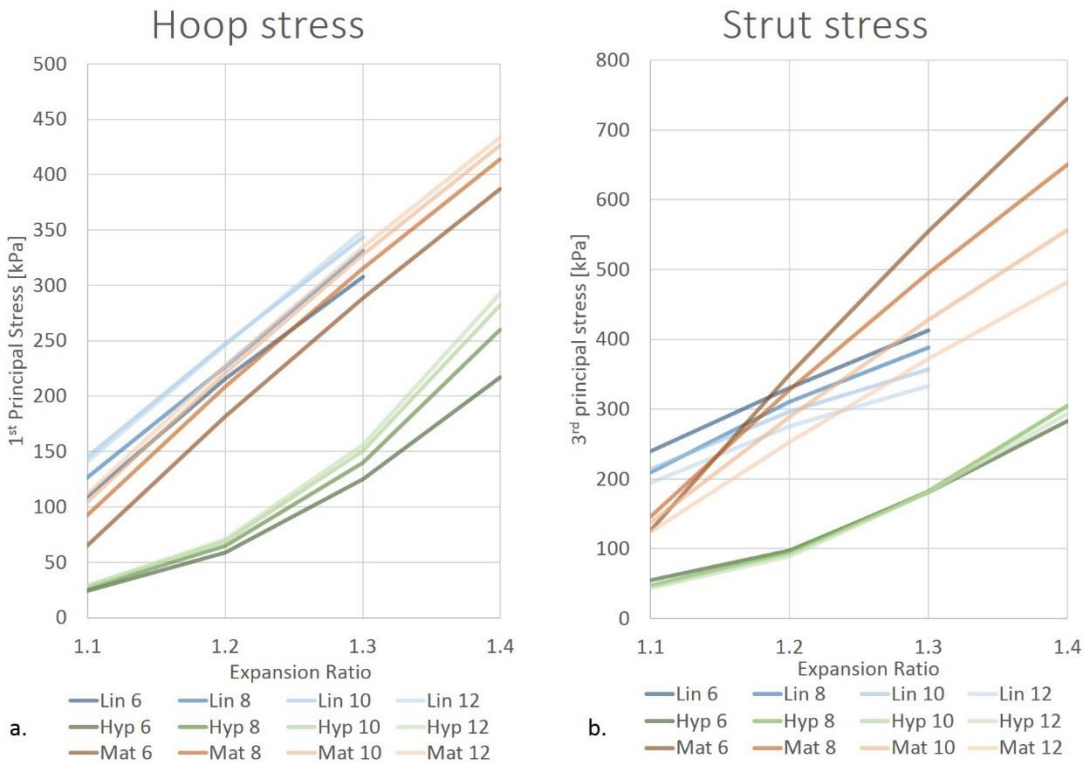

Figure III.7 - Evolution of hoop stress (a) and strut stress (b) during the expansion time for the analytical model developed in Matlab (red lines), for the finite element models, linear elastic (Lin: blue lines) and hyperelastic (Hyp: green lines). The number in the legend indicates the number of stent struts for each model.

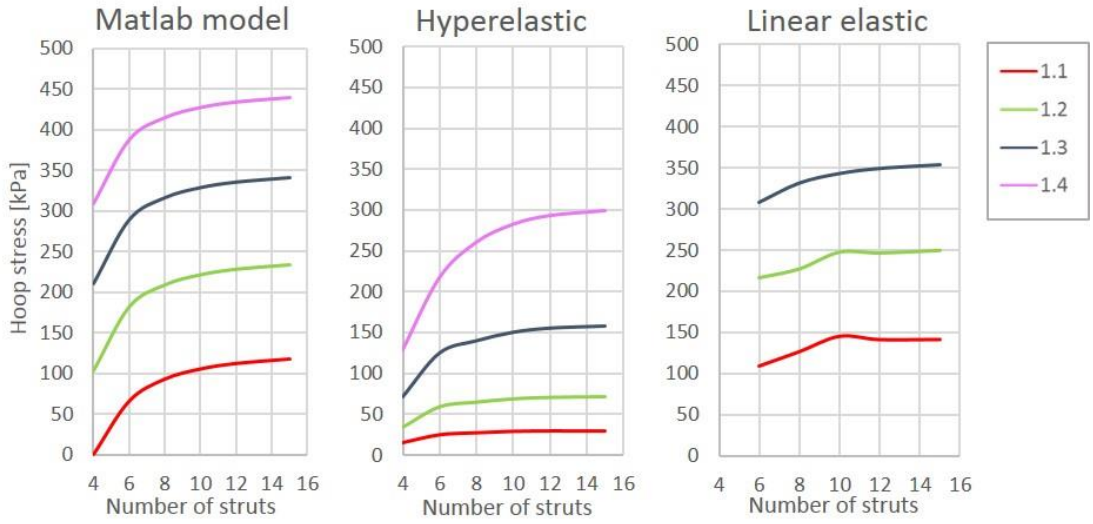

Figure III.8 - Hoop stress with increasing number of struts for the analytical model (left), hyperelastic (centre) and linear elastic (right) finite element models. The colour of the lines indicate the expansion ratio.

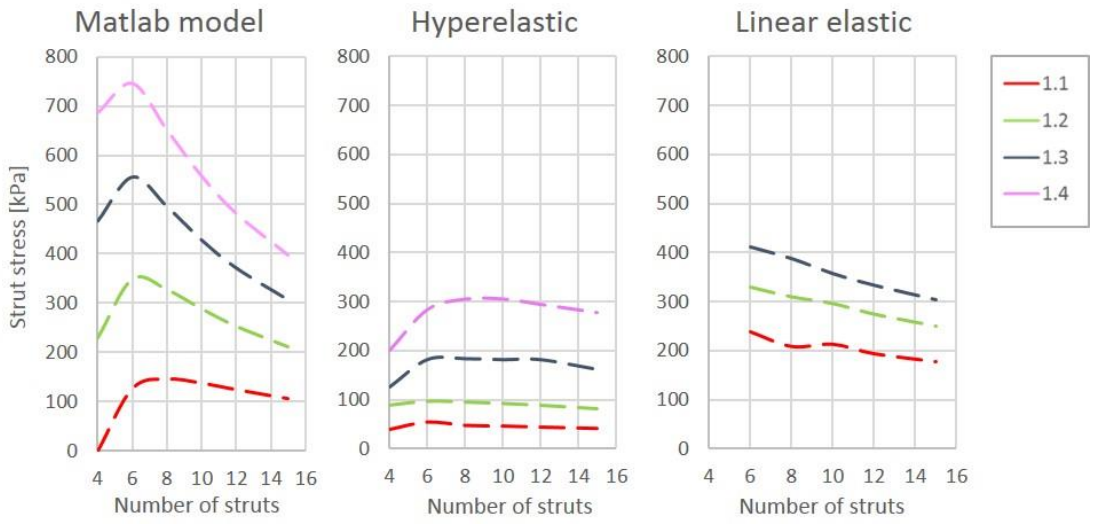

Figure III.9 - Strut stress with increasing number of struts for the analytical model (left), hyperelastic (centre) and linear elastic (right) finite element models. The colour of the lines indicate the expansion ratio.

Discussion

The results reported the outcomes of the analytical model and the finite element model of a vessel with evenly distributed stent struts, first separately and then compared.

Matlab model: the results with a smaller variation in number of stent struts (*Figure III.5.a*) allows a deeper understanding of the quick change in the stresses on the stented vessel with a little change in number of strut, in the first part of the curve. The results with the higher variation in number of struts (*Figure III.5.b*) gives some confidence on the model, as the stress results get closer to the uniform pressure ones with a larger number of stent struts. It has to be taken in consideration that an increase of stent struts for this comparison only has meaning until the struts start overlapping; in other words, when the number of struts multiplied by the contact length equals the circumference of the vessel. For the parameters reported here this occurs at a value between 200 and 300 struts, according to the expansion (275 for the 1.4:1 rate).

ANSYS model: linear elastic and hyperelastic model results show noticeably different behaviours for increasing expansion ratio, although both with increasing hoop stress (*Figure III.6*). It can be noticed how the results for the hyperelastic model better represent the non-linear behaviour of arteries described in Chapter 2.

Comparison between the Matlab and ANSYS results: Comparing results between the analytical and finite element approaches for increasing expansion ratio (*Figure III.7*) demonstrates that, whilst for all the models the stress increases with the expansion rate for a given number of struts, the gradient is positive for the hyperelastic model and negative for the linear elastic model, while the analytical model reports a linear stress increase. The nonlinearity of the linear elastic finite element model results from the non-linear geometry effects included in the ANSYS simulation: it has to be noted that the linear elastic model has been used outside its range of validity, which is only up to a circumferential strain of 5-10% (van Andel, Pistecky et al. 2003, Holzapfel 2006).

Comparing the results with increasing number of struts for both the hoop and strut stress, it appears that all the models follow the same trends (*Figure III.8* and *Figure III.9*), although, due to convergence issues, limited data can be obtained for the linear elastic model for smaller numbers of struts and at larger expansion ratios. For the hoop stress, the values of the linear elastic model are quite similar to the analytical model, while for strut stress they appear to be much higher. This might be due to the difference in contact area: the hoop stress for the analytical model is calculated with the assumption of a constant contact area, while in the finite element model it changes and the stress reported is only the peak stress, rather than the average of the distribution on the strut. Another difference that needs to be taken in consideration is the non-linear geometry assumption for the ANSYS model.

This section showed how very different types of model can give the same trends of results for a simple symmetric model of stent expansion. The next session explores the variation in results for a more realistic model of a stented vessel, with an uneven distribution of stent struts in the cross-section.

3.2 DEVELOPMENT OF A MODEL WITH UNEVEN STRUT DISTRIBUTION

When considering a 2D model of a cross-section of a stented vessel, a discrete representation of the expansion with stent struts is more realistic than a uniform pressure. But analysing histological images of explanted animal models (Gunn, Arnold et al. 2002), it is also observed that in most cases the distribution of the struts is not even in a cross-section.

Figure III.10 shows an example of a 3D stent geometry obtained from uCT data from a porcine model of stent expansion; further details of the methods used to obtain this geometry are provided in Chapter 4. From analysis of cross-sections of the stent geometry it is clear that some sections contain a fairly even distribution of struts, as highlighted in the red cross-section, while some show a more uneven distribution, as shown in the green cross-section, despite being taken from the same stent deployment.

The aim of the second section of this Chapter is to analyse the impact of an uneven strut distribution on the magnitude and distribution of the stresses in the vessel. The implications of the results of both sections are then discussed as this forms the basis for the stimuli considered to drive the evolution of ISR in the next Chapters.

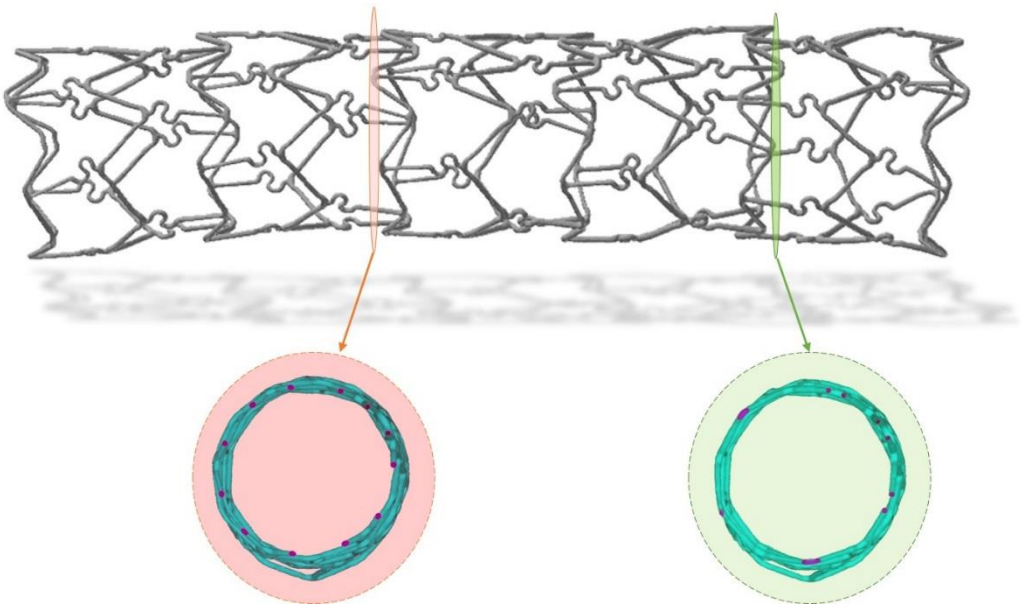

Figure III.10 – 3D geometry of a Biodivisio stent obtained through uCT imaging. The two cross-sections show even (red) and uneven (green) distributions of stent struts within the same stent.

Methods

This section is based on the approach presented in the previous section, but with a variation in the inter-strut angle rather than an equal spacing. In order to choose the distribution of the stent struts, histological images (courtesy of Dr. Julian Gunn) obtained as described in Chapter 4, were analysed to provide realistic stent strut distributions (*Figure III.11*). These images come from the same porcine restenosis model used to obtain the 3D geometry of the stent in *Figure III.10*, which will be used in Chapter 4 for the development of a 3D stent/vessel interaction model. Use of this data to inform the 2D model presented here allows later comparison between 2D and 3D results.

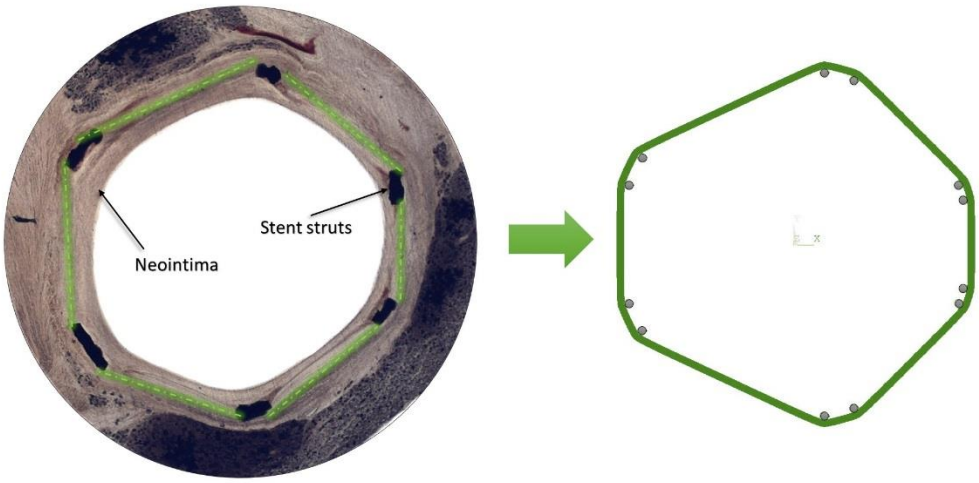

Figure III.11 – On the left, histological cross-section of a stented vessel with neointimal growth (courtesy of Dr. Julian Gunn) which was used as an example to design the finite element model of a stent/vessel cross-section on the right.

Given the nature of the BioDivysio stent design, the models that will be compared are composed of 12 struts each. A comparison between the analytical model developed in Matlab and the finite element model developed in ANSYS is again undertaken, also to provide a comparison between even and uneven distribution of the struts with both models. Within the ANSYS model, only the hyperelastic material model was considered, as the difference in behaviour between the two materials was explored in the previous section and the linear elastic model shows instability for high expansion ratios.

Matlab model: the model is similar to the one described in the previous section. It represents the cross-section of an artery, with initial vessel radius R_i = 1.4 mm, thickness t = 0.1 mm, elastic modulus E = 1 MPa and Poisson's ratio ν = 0.5. The symmetric expansion for comparison is defined by a constant angle between the struts $\vartheta_i = 360/Nstruts = 360/12 = 30°$ (*Figure III.12.a*). For the uneven model, the position of the stent struts are defined with varying inter-strut angle, ϑ_i (*Figure*

III.12.b), but they are each displaced to the final radius R_s through the same expansion ratio R_s/R_i:1 of 1.4:1.

The hoop strain is calculated as $\varepsilon_\vartheta = \log(1 - \frac{C_{fin}-C_{in}}{C_{in}})$, with C_{fin} being the sum of the segments of vessel between the stent struts, which in this case are not of constant length and are given by $s_i = 2R_s \sin(\vartheta_i/2)$. The hoop stress is $\sigma_\vartheta = \varepsilon_\vartheta \cdot E/(1-\nu^2)$.

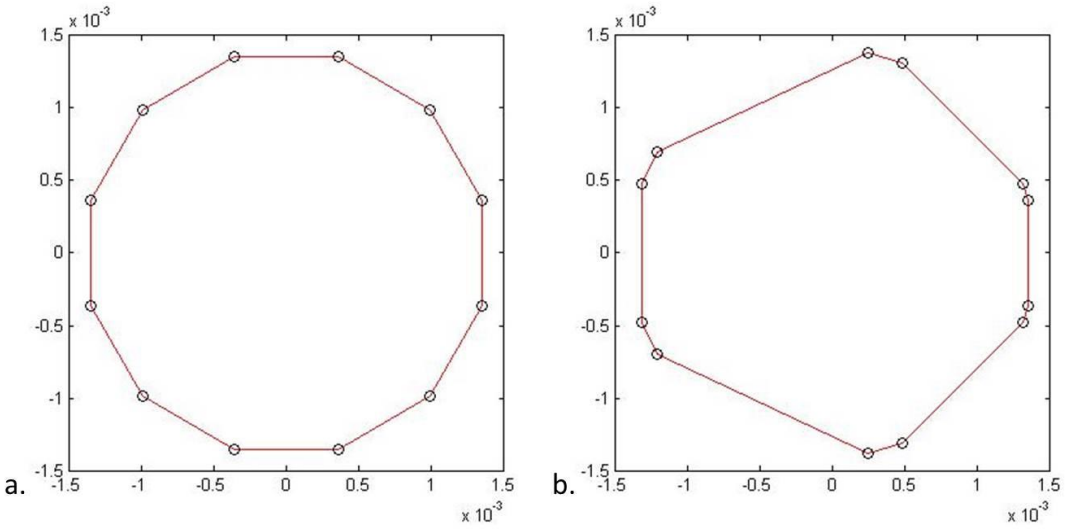

Figure III.12 - Two stent/vessel analytical models with even (a) and uneven (b) distribution of 12 stent struts.

The reaction force per unit axial length on the stent struts changes slightly, as the angles that divide each strut to the two neighbouring ones are not constant, so it becomes: $F_{strut_i} = \frac{1}{2}\sigma_\vartheta(\sin(\vartheta_i/2) + \sin(\vartheta_{i+1}/2))t$. The strut stress is $\sigma_{strut} = F_{strut}/L_{strut}$, where *Lstrut* is 0.045 mm, corresponding to the radius of the stent strut.

ANSYS model: ANSYS Mechanical APDL version 14.0 (ANSYS Inc.) was used to generate the same 2D geometries that were explored through the analytical model (*Figure III.13*). The model is similar to the ANSYS model in the previous section, but, in order to generate the cross-section with uneven distribution of struts,

the symmetry was reduced to ½. A hyperelastic material model was used as described previously, where $U = 0.04\cdot(I_1 - 3) + 0.003\cdot(I_2 - 3)^2 + 0.085\cdot(I_2 - 3)^3$. Initial vessel radius and thickness are 1.4 mm and 0.1 mm respectively.

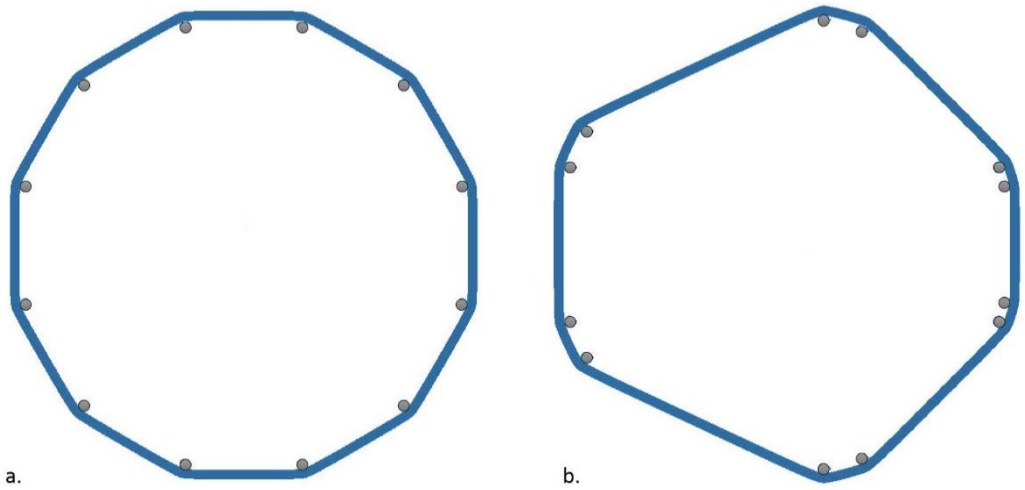

Figure III.13 – The two stent/vessel finite element models with even (a) and uneven (b) distribution of 12 stent struts.

The six stent struts for each ½ symmetry have a radius of 45 µm and are modelled using circular 2D target elements (TARGE169) with 2D contact elements (CONTA171) defined on the inner vessel wall. For the vessel, 23040 2D solid elements (PLANE 182) were used, with 32 elements through thickness and 720 elements along the circumference.

Results

Matlab model: the results of the analytical model are reported in *Figure III.14*. Specifically, *Figure III.14.a* shows the results for the symmetric model, with evenly distributed stent struts: the hoop stress for expansion ratio and the strut stress for each strut. *Figure III.14.b* shows the same information for the model with uneven strut distribution with inter-strut angles chosen to match the finite element model. For both models, the different lines represent the results for different expansion ratios, from 1.1:1 to 1.4:1.

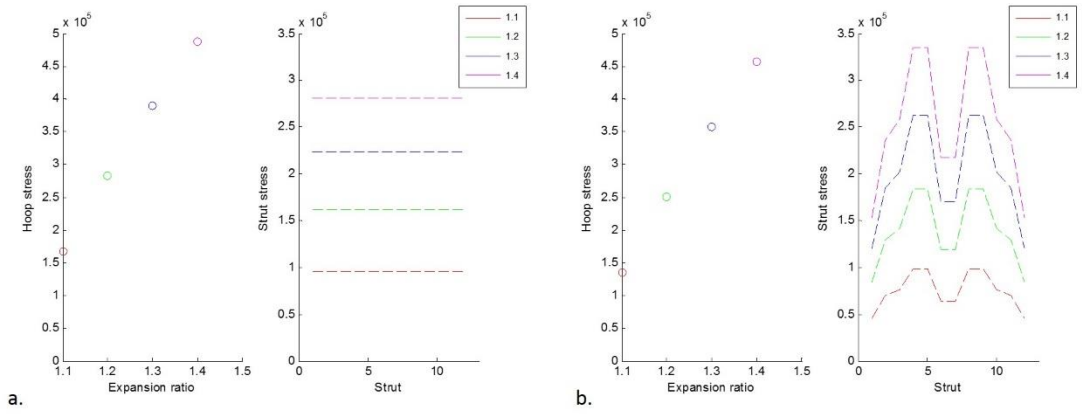

Figure III.14 – Variation in hoop stress and strut stress with expansion ratio for each strut for the even (a) and uneven (b) strut distribution models (red = 1:1.1, green = 1:1.2, blue = 1:1.3, magenta=1:1.4).

ANSYS model: the results for the models with even and uneven stent strut distribution have been plotted and reported in *Figure III.15*. The distribution across the thickness of the strut stress, which is negative because it is a compressive stress, is similar in the two models, but the peak stress is higher for the 1/12 symmetry model, while the distribution along the circumferential direction shows some variation in the asymmetric model.

Due to the relatively small variation in the magnitude of the peak stress a more detailed analysis is provided in *Figure III.16* and *Figure III.17*, which report the 3rd Principal stress results at all the nodes of the inner layer of both models.

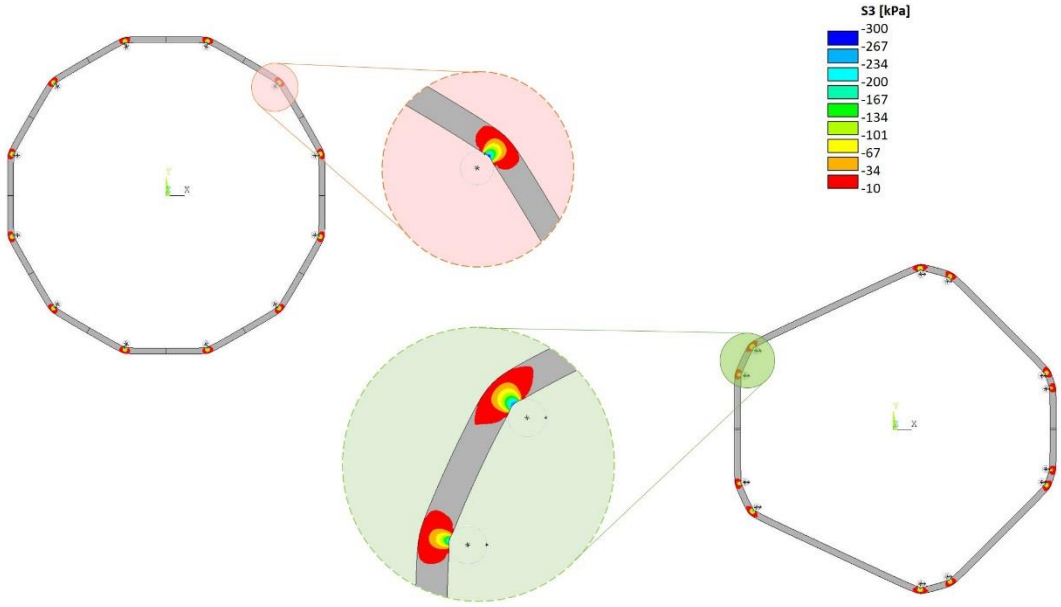

Figure III.15 - Plot of the distribution of the 3rd Principal stress for the models with even and uneven stent strut distribution in ANSYS, with a zoom-in of some strut areas.

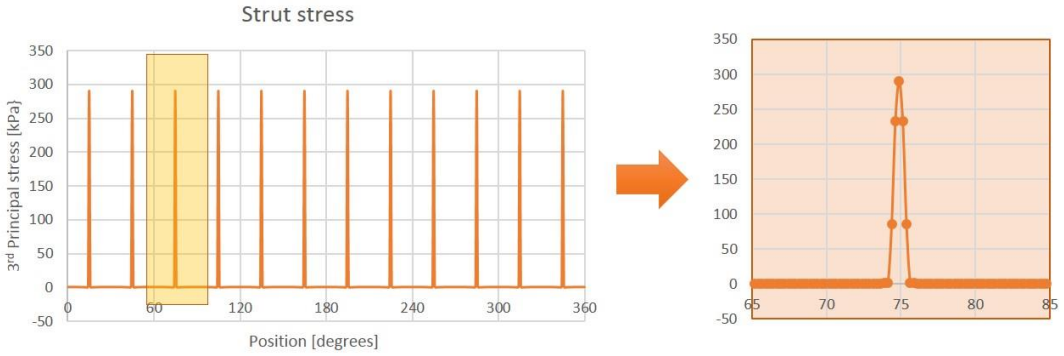

Figure III.16 - Strut stress at the inner nodes of the symmetric model and more detailed plot of the stress for one of the struts

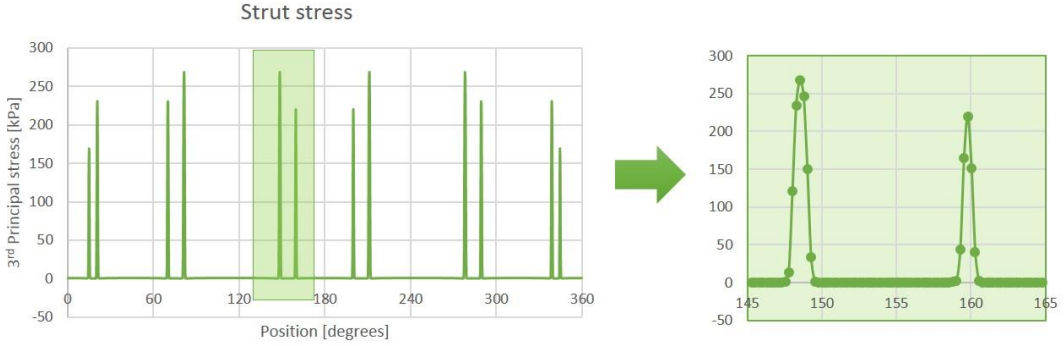

Figure III.17 - Strut stress at the inner nodes of the asymmetric model and more detailed plot of the stress for two of the struts, number 5 and 6, including the one that presents the peak stress.

Comparison between the Matlab and ANSYS results: *Figure III.18* reports a comparison of the strut stress results at the strut locations for the asymmetric case between the analytical and the finite element model. The differences in the values are due to the use of different material models, but the two follow the same trend, with higher values for the same struts. Specifically, these are found for the struts observed above, number 4 and number 5, separated by an inter-strut angle of 70°, these peaks represent an increase of 31% and 16.4% above the average strut stress for the Matlab model and ANSYS model respectively.

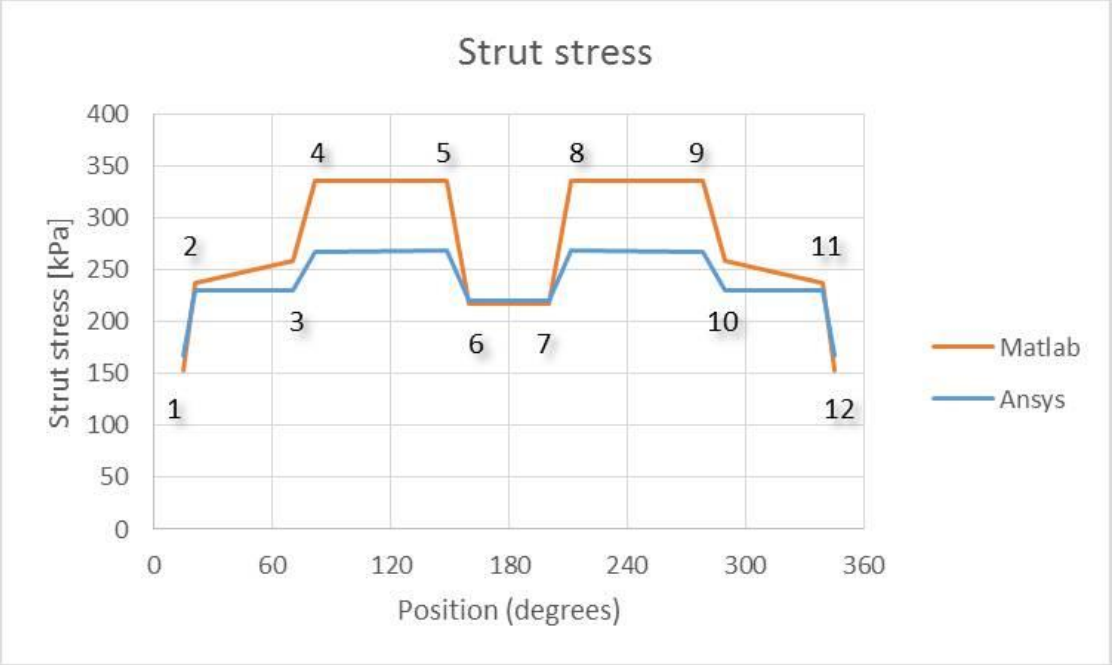

Figure III.18 - Comparison between the strut stress results at the strut locations for each strut between the analytical and the finite element model, for the asymmetric case.

Discussion

In the results section, the outcomes obtained for a model of a stented vessel with uneven distribution of stent struts through the analytical model and the finite element model are presented, in terms of hoop stress and strut stress, first separately and then compared.

Matlab model: the results (left plot of *Figure III.14.a* and *Figure III.14.b*) show the hoop stress for the uneven strut distribution is lower than for the even one, which follows the trend seen moving from a uniform pressure to a discrete distribution of struts. The effect is due to the fact that, given the same number of stent struts, the even, symmetric distribution generates an expanded shape that is the closer to a circle, corresponding to a higher hoop strain. Specifically, for a 1.4:1 expansion, the hoop stress decreases from 488 kPa to 456 kPa. The strut stress (right plot of *Figure III.14.a*) is constant for all the struts in the symmetric model due to the symmetry condition; in the uneven model, on the other hand, the stress varies from strut to strut, and this variation becomes more substantial as the expansion ratio increases (right plot of *Figure III.14.b*). As a result the stress for a given strut can be considerably higher or lower than the corresponding strut stress for the symmetric model at the same expansion ratio.

The hoop stress is higher for the symmetric than for the asymmetric model at all expansion ratios, the percentage difference decreases from 19% to 6.5% from a ratio of 1.1:1 to 1.4:1. Consequently, the percentage difference of the average strut stress between the two models decreases with the expansion ratio, from 21% to 8%. The percentage difference between the strut stress for the symmetric model and the peak strut stress, observed under struts 4 and 5, for the asymmetric model increases with the expansion ratio from 3% for 1.1:1 ratio to 19% for 1.4:1 ratio.

ANSYS model: the results plotted in *Figure III.15* show similar peak strut stress magnitudes for symmetric and asymmetric model; the plots of stress distribution (*Figure III.16* and *Figure III.17*) confirm that the peak stresses do not vary by large amounts between the models, but they are slightly higher for the symmetric model, 290.5 kPa at each strut compared with a peak value of 267.9 kPa

for the asymmetric model. This is explained by the decreased hoop stress found for the asymmetric model, as discussed earlier in this Chapter, which contributes to the reaction force between the vessel and the stent strut. It is clear that the stress is distributed over an area, which suggests that the response of the vascular tissue may not be determined solely by the value of stress at the single node at which the stresses are reported in *Figure III.18*. This effect is more noticeable in the model with uneven distribution of struts. It should also be noted that, in this case, the expansion of the struts involves sliding between the strut and the inner layer of the vessel which changes the location of the peak stress as the stent deploys. An important observation for the asymmetric model is that higher stresses are found in regions where struts are separated by a larger distance, as is the case for stent struts 4 and 5, where values of 267.5 and 267.9 kPa are reported. To put these magnitudes of stress in context, in the literature a value of 35 kPa for compressive stress under the struts has been used as a threshold for vessel injury (Boyle, Lennon et al. 2010). This value corresponds to a pressure of 263 mmHg, far from the physiologic values and therefore not normally experienced by an unstented vessel. For all the models reported here, this threshold is exceeded only in the location of the stent struts, as can be seen from *Figure III.15*.

Comparison between the Matlab and ANSYS results: Both the analytical and finite element models report differences in the distribution of stress concentration in the more realistic case of a cross-section with an uneven distribution of stent struts. The significance of this distribution of stress as a stimulus for tissue growth will be explored further in Chapter 4.

The considerations reported above about the locations where the peak strut stress is found are valid for both models, as shown in *Figure III.18*. Whilst results

from the analytical and finite element model demonstrate similar trends, the finite element model allows the use of a more sophisticated material model which better represents the properties of arterial tissue: the hyperelastic model used in this Chapter allows to capture the distribution of the stresses that is closer to the reality of a biological vessel, in particular for higher expansion ratios. Furthermore, the finite element model allows the study of distribution of the stress values through the thickness and along the circumference, the local changes in hoop stress and the effect of local bending of the vessel, which can be more severe for high expansion ratios and particularly uneven strut distributions.

This section has reported how an asymmetric distribution of stent struts is a more realistic representation of a cross-section of a stented vessel. The results from the analytical and finite element models both show little difference in peak strut stress between the two models. This happens because an increase in asymmetry with the same number of struts results in higher local bending but a lower global hoop stress, which determines the reaction force between vessel and stent. However, the distribution of stresses between struts can differ significantly within the asymmetric model, resulting in higher values for stent struts with greater inter-strut distance.

SUMMARY

The choice of how to represent stent/vessel interaction within a 2D model can influence the stresses predicted by the model approximations. This may result in different predictions of development of ISR if the cellular model is based on the magnitude of these stresses. As it was observed from studies of *in vivo* stent deployment, the distribution of stent struts within each section of the stented vessel is not usually uniform, resulting in areas of focal bending and concentration of strut stress. The 2D representation is not able to capture out-of-plane effects, which might change the nature of the stent induced stresses significantly, particularly at the extremes of the stent. This effect is examined using a 3D model in Chapter 4.

The results reported in this Chapter, describing changes in hoop stress and strut stress with strut distribution and inter-strut distance, are useful to consider how such stress acts as a stimulus for growth at the level of an individual cross-section. Chapter 5 extends this analysis to include in the model introduced in this Chapter the evolution of the neointimal tissue resulting from the stress stimulus, including the influence of cellular level effects.

CHAPTER IV – 3D STENT/VESSEL MODEL

INTRODUCTION

In Chapter 3 a 2D model of stent/vessel interaction, represented by the vessel cross-section, was presented with the aim of exploring the variation of stress associated with stent expansion in a coronary artery, in terms of the number of stent struts and their distribution, through analytical and finite element methods. A 2D representation is a simplification of the model, which might not include important factors such as out-of-plane effects.

This Chapter describes a 3D model developed to gain better knowledge of the distribution of stresses in a vessel from the presence of a realistically deployed stent, as part of a framework developed across different research centres. The aim of the framework is to use data from the same *in vivo* model of ISR to develop various computational simulations and to compare their results. The focus of this Chapter will be on the structural mechanics, investigated through a finite element model formed by an idealised vessel and a realistic stent geometry post-expansion: this was obtained using detailed 3D geometric data from micro-CT images of a porcine ISR model. This method allowed to explore the differences in stress distribution at the level of individual struts and to compare the results to histological data from the same model and to the results obtained from a fluid dynamic simulation of the same stent/vessel geometry performed in another research centre. Finally, the results and

their correlation are discussed in the optic of a concurrence of the two stimuli to the development of neointimal growth.

4.1 DEVELOPMENT OF A FRAMEWORK ACROSS RESEARCH CENTRES

In the previous Chapters it was shown that several mechanical stimuli may contribute to the mechanobiology of the cells of an artery and influence the development of ISR. Any computational study designed to study the magnitude of these stimuli or any model that uses this information to predict cellular growth needs some experimental data for validation purposes. In order to study ISR *in vivo* studies are essential, although these are expensive and take a long time, so the ideal is to plan them carefully in order to provide data that can be used to inform as many computational studies as possible. This approach also allows comparison between computational studies that consider different types of mechanical stimuli with the same validation data, which opens the door to the evaluation of the combined effect of different stimuli and their relative influence on biological outcomes.

This Chapter introduces previous studies that have reported similar methods; it then describes a framework where various computational simulations were undertaken in different research centres, all using data obtained from a single experimental model (Amatruda, Bona Casas et al. 2014). Finally, it describes the results of one of these studies more in detail, with focus on the computation of the structural mechanics.

A number of previous studies have compared the findings of computational simulations with histology data in order to evaluate the effect of the considered stimulus with the *in vivo* growth of neointima (Chen, Sinha et al. 2011, Timmins, Miller et al. 2011).

An example that deals with structural stress is a study by Timmins *et al*. (Timmins, Miller et al. 2011): in this work, the hypothesis that a stent which

generates higher stress in the vessel wall will generate a more aggressive biological response was investigated. Two stent designs were implanted into healthy porcine coronary arteries with a expansion ratio of 1.4:1.0 and the neointimal growth was evaluated 28 days after, through histology, morphometric analysis and histopathologic analysis; the interaction of these two stent designs with an idealised model of the arterial wall was modelled using the finite element approach and the difference in stress distribution generated by the two stent designs was compared with the biological outcomes. In this study the circumferential stress was considered and the models of the struts were idealised, especially regarding the geometry of the expanded stent: these give a good measure of the difference of potential injury between two stent designs, but the method does not capture the realistic variability in local strut stress, as the peak stresses are homogenously distributed along the strut profiles.

Other studies have reported multiple contributions to neointimal growth by comparing simulations of different mechanical stimuli with experimental evidence. For example, Chen *et al*. (Chen, Sinha et al. 2011) compared experimental and computational data to test the effect of stent sizing on the development of ISR. Stents were implanted in 10 swine with various sizing ratios and restenosis was evaluated 1 month after using IVUS and, in some cases, histology. Finite element models reproduced the expansion of idealised stents at the same sizing ratios, followed by a fluid dynamic simulation of the stented vessel. Variations in the mechanical conditions (wall shear stress, WSS, and WSS gradient, oscillatory shear index and circumferential wall stress) were evaluated as possible promoters of neointimal hyperplasia and the strength of correlations between these values and the magnitude of restenosis over the range of deployment ratios were reported.

The methods used by Chen *et al.* provide a means for comparison between the mechanical environment and neointimal growth at the scale of the whole stent, but as the expansion of the stent is idealised, it is less likely to provide accurate information about the local mechanical stimulus at the individual strut level for balloon expanded stents.

The following section describes a framework that makes use of detailed 3D geometric data from experimental models of ISR to develop computational models of the local mechanical stimuli following stent deployment. The results of these simulations are compared with the levels of neointima observed in the region of individual stent struts. In a similar manner as the studies described above, the histology images are used for a comparison with the computational results; the main difference stands in the fact that, in this case, the experimental data are also used to obtain a realistic stent geometry for the computational models through the use of micro-CT images: this allows to capture a realistic variability in local strut stress.

Description of the framework

The description of the framework presented in this section and of the individual studies it refers to can be found in several publications (Morlacchi, Keller et al. 2011, Tahir, Hoekstra et al. 2011, Tahir, Bona-Casas et al. 2013, Amatruda, Bona Casas et al. 2014, Keller, Amatruda et al. 2014). This framework results from collaboration between three institutions: University of Sheffield, Politecnico di Milano and University of Amsterdam. After a brief overview of the whole framework, detailed reporting of the computational simulations performed at the University of Sheffield will be provided.

The method presented allows the use of multiple *in silico* models, developed in different research centres and validated though the same set of data coming from an *in vivo* porcine model, in an effort to better understand the dynamics of ISR, from the point of view of the influence of mechanical stimuli on the neointimal growth.

Figure IV.1 shows an overview of the approach used: micro-CT images and histology of the experimental model of ISR allow both monitoring of the growth and basis for the construction of the models. The experimental studies were performed at the University of Sheffield, where an *in vivo* porcine model of in-stent restenosis was developed (Morlacchi, Keller et al. 2011) (*Figure IV.1.a*). Micro-CT images provide the basis for reconstruction of the full geometry of a stent expanded in a vessel without the assumption of idealised expanded geometry. These data offer valuable support for the creation of a computational model of stent-vessel interactions, which was developed for structural analysis in University of Sheffield, Medical Physics group, and for a fluid dynamic analysis in Politecnico di Milano, LaBS (*Figure IV.1.b*). The results were post-processed to compare with histology data from the explanted stented vessel following the development of a neointima, in order to obtain an estimation of the influence, at the level of individual stent struts, of the structural and fluid dynamic environment on the local neointimal growth. The University of Amsterdam have developed a multi-scale model of ISR based on cellular growth over time, in 2D and 3D, with the inclusion of the effect of fluid dynamics, and the growth pattern was compared to the development of restenosis over time in the porcine study (*Figure IV.1.c*).

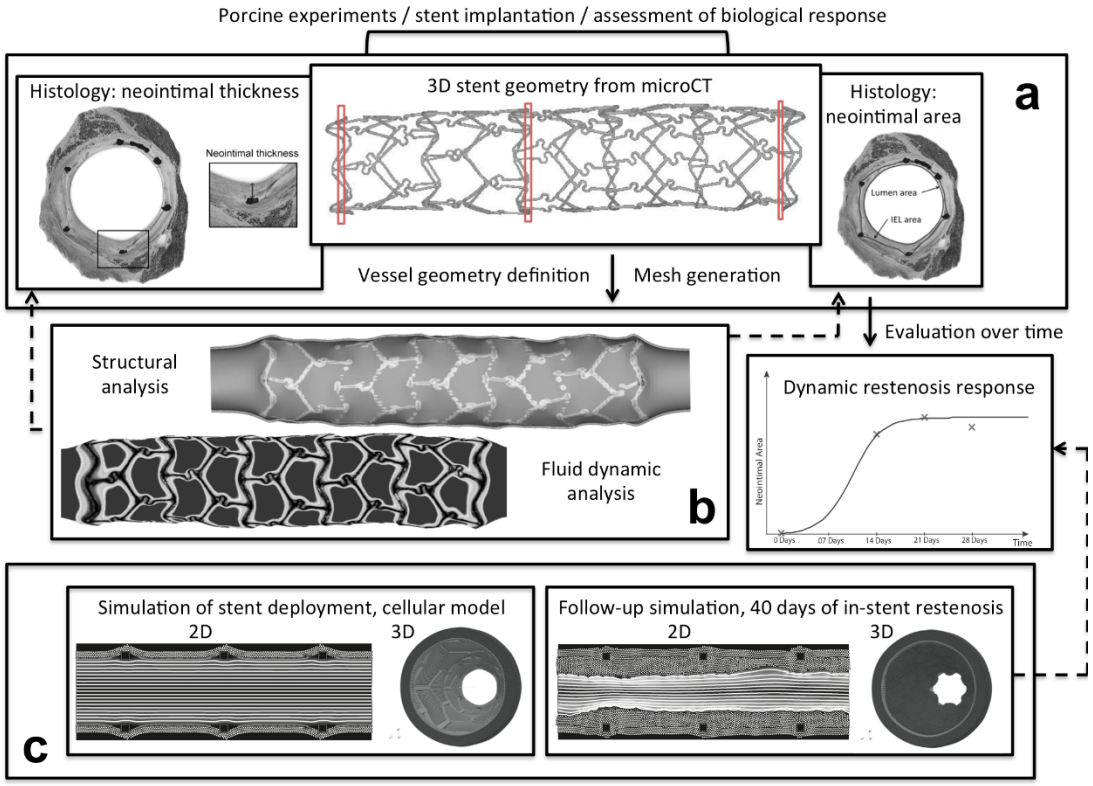

Figure IV.1 - Overview of the workflow developed across research centres: the *in vivo* porcine model of restenosis provides data to generate computational models (solid arrows) and to validate results (dashed arrows). (a) Micro-CT data allowed to obtain a 3D stent geometry; histology data were used to inform the growth model with growth evaluation over time and as a post-processing mean to evaluate results. (b) Structural and fluid dynamic analysis were developed from the stent geometry and the results were evaluated as local-to-strut stimuli post-stenting. (c) Multi-scale ISR model of cellular development over time. Reproduced with permission from (Amatruda, Bona Casas et al. 2014).

For the purpose of this thesis, the focus of this Chapter will mainly be on the methods, various approaches for data processing and results interpretation associated with the structural analysis. As one of the aims of this work was to understand the combined effect of spatial localization of structural and fluid dynamic stimuli on ISR immediately after stenting, the results are compared with the results of CFD simulations, produced by Politecnico di Milano, along with the histology data. A brief description of the CFD methodology is included to make the comparison more understandable to the reader.

The next section describes the method used to evaluate changes in solid and fluid mechanics following stent implantation, through the use of a common 3D stent

geometry obtained from micro-CT data and a set of histology images for comparison between stresses obtained and neointimal growth at stent strut locations.

Methods

This section refers to the study reported in Keller *et al*. (Keller, Amatruda et al. 2014), reported here in more detail, in particular regarding the structural simulations.

In the following sections, "*Histology Data*" describes the porcine model of restenosis and the imaging techniques used to obtain data from it. "*Structural Analysis*" introduces the methods concerning the finite element model, from import of the realistic stent geometry to the inclusion of an idealised vessel; "*Fluid Dynamic Analysis*" provides a brief overview of the methods used for CFD analysis, as the outcomes of the three methods will be compared in the last part of the Results section.

Histology Data:

An *in vivo* model of ISR, obtained through overexpansion of stents in healthy coronary arteries in order to observe the amount of neointimal growth at a set of time-points, was developed (Morlacchi, Keller et al. 2011) involving stent implantation in healthy Yorkshire white pigs. Typically, two stents were deployed in each animal, in both the right coronary artery (RCA) and left anterior descending artery (LAD). The procedure was performed in agreement with UK Animals (Scientific Procedures) Act, 1986; a more detailed description can be found in Malik *et al.* (Malik, Gunn et al. 1998).

For this study the stent used for implantation was the BiodivYsio® (Biocompatibles International Plc, Farnham, UK), a balloon expandable stent made

of 316L stainless steel. The expansion ratio used for this model is 1.4:1, so that there was enough overexpansion to observe a neointimal growth, but without provoking a considerable damage to the vessel. As already reported in the previous Chapters, the gold standard amount of expansion in clinical use is about 1.1:1 – 1.2:1.

The animals were sacrificed at different time points in order to determine the variation over time of the magnitude of restenosis, using stents with the same design and with the same degree of over-expansion in healthy arteries. The chosen time-points were 6 hours, 4, 7, 14, 21 and 28 days post-implantation.

For the study described in this Chapter, one data set was considered where the stent was implanted into an RCA and the stented vessel was excised for analysis 14 days after stenting. This specific specimen was chosen as the stent maintained its integrity, allowing an easier reconstruction of the geometry, did not provoke excessive damage to the vessel, and demonstrated sufficient levels of ISR to be suitable for histological assessment. After being embedded in a methacrylate resin, the vessel was scanned using ultra-high resolution micro-Computed Tomography (micro-CT) (Skyscan, Belgium): this allowed 3D reconstruction of the expanded stent (*Figure IV.2*).

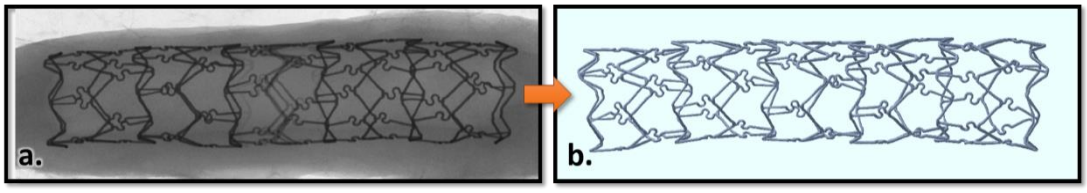

Figure IV.2 - From (a) embedded stented vessel projection image from micro-CT scan to (b) reconstructed 3D geometry of the expanded stent.

For the following histomorphometric inspection, the vessel was cut into 10-μm thick transverse sections using a high-speed precision saw. These were numbered and a subset were chosen for further analysis and quantitative measurements.

Matching between the locations of the 3D geometry of the stent and the histology images was achieved by comparing the longitudinal distance between the cross sections with the position of the stent struts in cross-section of both the reconstructed 3D stent geometry and the histology sections. The correspondence between the seven histology sections chosen for further analysis and the 3D reconstructed stent geometry is shown in *Figure IV.3*.

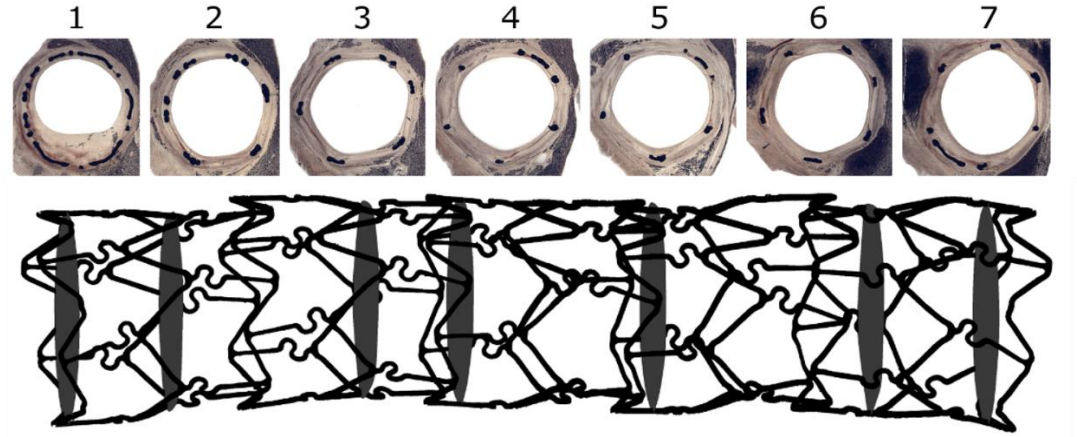

Figure IV.3 – The seven histology images (upper pane) correspond to seven cross-sections in the proximal, medial and distal areas of the stented vessel, as represented in the image of the micro-CT reconstruction of the stent geometry (lower pane). Reproduced with permission from (Keller, Amatruda et al. 2014).

The histology images were analysed to obtain a quantitative measure of the neointimal growth to be compared at the level of individual struts with the results obtained from the computational models. Seven of the cross sections were chosen, in order to provide data throughout the proximal, medial and distal areas of the stented vessel (*Figure IV.3*).

Observing the histological images, as shown in *Figure IV.4*, it is possible to notice that the stent struts are immediately recognisable. In most of the images it is also possible to trace the internal elastic lamina (IEL) which runs from one stent strut to the next one: it is then possible to evaluate the amount of neointimal growth as the area included between the IEL and the new lumen. In order to compare mechanical

stimuli and ISR at the individual stent strut location, the growth was quantified locally as neointimal thickness (NIT), the radial distance between the stent strut and the lumen (*Figure IV.4*).

The volumetric micro-CT data were segmented to define the 3D surface geometry of the expanded stent, which was then used to define a contact surface for analysis of the interaction of the stent with an idealised model of the vessel, a cylinder with constant radius and wall thickness, in order to perform solid and fluid mechanics simulations.

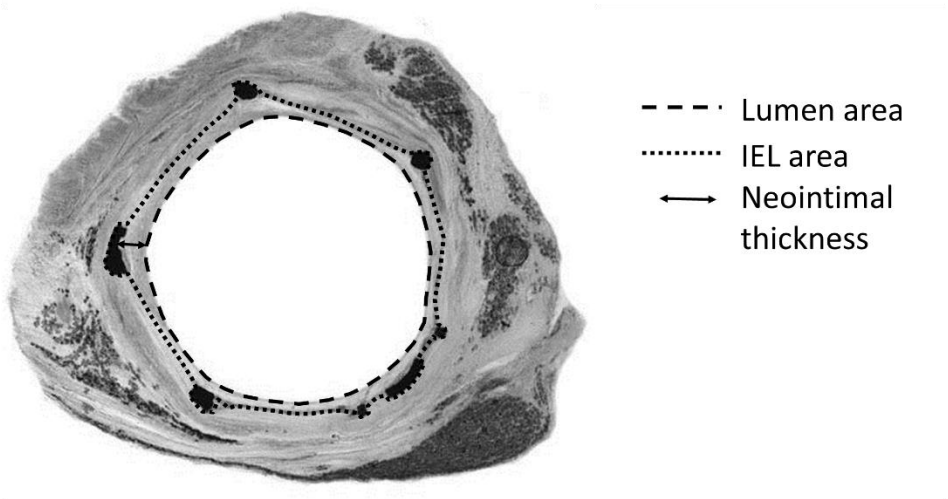

Figure IV.4 – Example of histology image. The stent struts are visible in black; the lumen area is contained by the coarse dashed line, while the fine dashed line follows the internal elastic lamina (IEL): the area included between these two lines is constituted by neointima. Neointimal thickness (NIT) is calculated strut by strut as the distance between the strut and the vessel lumen. Reproduced with permission from (Keller, Amatruda et al. 2014).

Structural Analysis:

As described in the previous paragraph, the 3D geometry of a realistic expanded stent was obtained by an imaging process that involves micro-CT scanning of stents explanted from a porcine model of ISR. In order to study the mechanical environment of the stented vessel, this stent geometry was imported into ANSYS Mechanical APDL (v14.0) (Ansys, Canonsburg, PA, USA). The model of the

coronary artery, on the other hand, was idealised and consisted of a straight cylinder. The dimensions were chosen to attempt to match as much as possible the *in vivo* vessel dimensions: the initial inner radius, r = 1.4 mm, was the lumen measured from the RCA of the *in vivo* model through angiography, before stenting and with physiological pressure applied, while the thickness, h = 0.1 mm, could not be measured, so it was estimated from the literature, through $h/2r$ = 0.04 (Nichols, O'Rourke et al. 2005).

The aim of the model was to provide a quantitative evaluation of the mechanical load in the local regions of stent struts to be compared with the seven histology images shown in *Figure IV.3*. For this reason, more accurate stress results were desired in the neighbourhood of the location of each histology image. This was achieved by creating seven shorter individual models of vessel, matching their central axial location with the position of the histology in the geometry and consequently the NIT measurements. This sampling method, compared to a full 3D model, provided the opportunity to increase the mesh refinement in the region of the cross-section. To obtain the desired accuracy in the central region whilst reducing the influence of the boundary conditions at the end sections of these short vessels, a length of 7.5 mm was chosen (*Figure IV.5*).

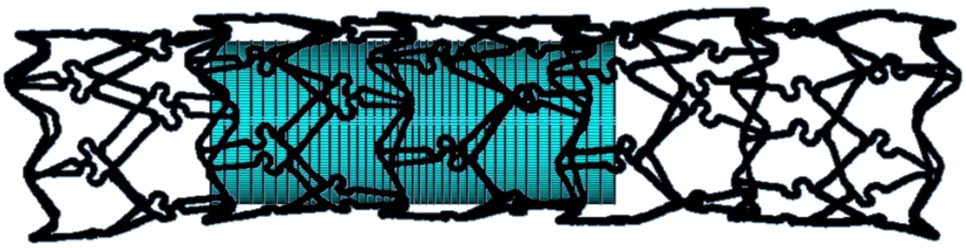

Figure IV.5 - One of the vessel sections, of a length of 7.5 mm, over the whole stent length.

The material model for the vessel was chosen according to what has been used in other models in literature (Gijsen, Migliavacca et al. 2008), as already introduced in Chapter 3. The hyperelastic properties of the vessel are described with a third-order strain energy density function:

$$U = 0.04 \cdot (I_1 - 3) + 0.003 \cdot (I_2 - 3)^2 + 0.085 \cdot (I_2 - 3)^3$$

where I_1 and I_2 represent the first and second invariants of the Cauchy-Green tensor; the constants are in MPa.

Meshing

For the meshing, solid elements SOLID185 were chosen for the vessel, designed for the three-dimensional modelling of solid structures. This element has 8 nodes each with 3 degrees of freedom each. Following mesh sensitivity tests, described in more detail below, the division of the solid vessel region into elements was chosen in the following way: 160 elements along the circumference, 3 through the thickness and 40 along the axial direction. The dimension of these elements is not constant, as a ratio between the dimension of the elements in the central region and the edges was specified, as shown in *Figure IV.7.a*. Elements were evenly distributed along the circumference, a ratio of 2 through the thickness produced thinner elements close to the edges, and a ratio of 0.5 along the axial direction created a finer mesh in the central area of the vessel.

Table IV.1 - Type and number of elements for the different parts of the finite element model

	Type	**Number**
Vessel	SOLID185	19200
- **Circumference**		- 160
- **Thickness**		- 3, ratio 2
- **Length**		- 40, ratio 0.5
Inner layer	CONTA173	6400
Stent	TARGE170	98102

To capture the interaction between the stent and the inner layer of the vessel within the finite element analysis, contact and target elements need to be defined. The element type assigned to the stent was TARGE170, which is used to define 3D target surfaces, with a total number of 98102 elements, while a set of 6400 contact elements CONTA173, used for deformable surfaces, overlay the inner surface of the vessel (*Figure IV.7.a*). A list of the type and number of elements can be found in *Table IV.1*.

The choice of mesh density was made following sensitivity tests to verify the independence of the outcomes of the model from refinements of the mesh in any direction. The values that will be evaluated from these simulations are the compressive stress and, at a later stage, the compressive force (*CF*), an integration of the compressive stress over a small region that includes the contact area of the stent strut with the vessel wall; this process will be described later in further detail.

With the chosen meshing, decreasing the size of the elements by half in each direction resulted in changes in compressive force of less than 2, 8 and around 2% of the maximum value of the model for the circumferential, axial and radial directions respectively. Moreover, the resulting element shape had a good element aspect ratio, improving the conditions to obtain convergence for all the simulations.

Further evaluations included the verification of the influence of model length on the results on the central section of the models and of the element type. By doubling the length of the vessel section and by substituting SOLID185 with SOLID186, a higher order element type, the change in compressive force resulted in the same order of magnitude changes as those reported for the mesh density tests.

The reported changes in value are low and do not noticeably affect the distribution of the values of interest over the artery (compressive stress, compressive force), which is the object of investigation in relation with the biological response.

Boundary conditions

The stent was assumed to be a rigid body fixed in all degrees of freedom; the longitudinal axes of vessel and stent were positioned in correspondence with each other. The constraints on the vessel were chosen so that it could expand and contract radially according to the applied loads without any rigid body motion and preserving the total length. The constraints in the *z* direction at the ends impede the axial displacement (*Figure IV.6.a*), while constraining motion in *x* direction at $x = 0$ and in *y* direction at $y = 0$ at the ends of the vessel (*Figure IV.6.b*).

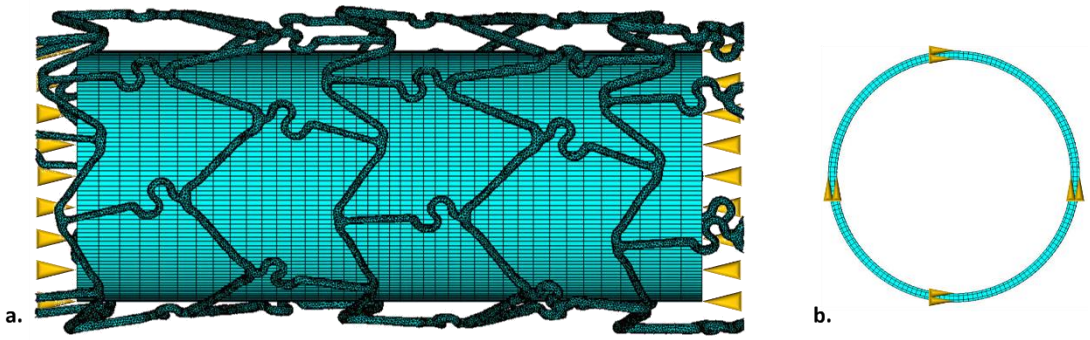

Figure IV.6 - Boundary conditions of the vessel: a. Constraints in z direction avoid axial motion, yet allowing free radial expansion; b. Constraint in x direction for x = 0 and in y direction for y = 0 avoid free body motion, allowing free radial expansion.

Loading conditions and solution

The dimension of the stress-free vessel model corresponds to the estimated dimensions of the real porcine vessel pre-stenting, under physiological pressure. Therefore, any pressure applied to the finite element analysis represents pressure above the mean physiological pressure. Due to the over-expansion of the stent the

initial radius of the vessel is smaller than the expanded stent radius. Representing the expansion of this stent to the final geometry could be inaccurate, computationally expensive and complicated and so a technique similar to the one used by Morlacchi *et al*. was used for this study (Morlacchi, Keller et al. 2011):

- any possible contact/target interaction is switched off between the stent/lumen;
- the vessel is radially over-expanded with an inner pressure load similar to the one used during angioplasty, 40 kPa, so that the vessel diameter is bigger than the stent at every point;
- the contact/target interaction between stent and lumen is re-established;
- the pressure load is gradually removed completely, so that the vessel deflates, interacting with the stent where it comes into contact, which keeps it expanded as observed in the *in vivo* model. (*Figure IV.7.b*).

The simulations were performed on a 64-bit desktop computer equipped with a 3.20 GHz quad-core processor and 16 GB RAM.

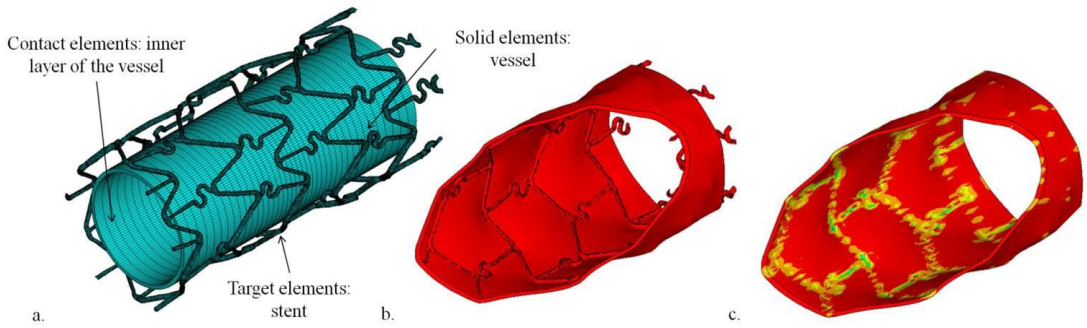

Figure IV.7 - Representation of one of the finite element analyses of stent/vessel interaction. a. Initial configuration of stent and vessel before vessel expansion; element types are indicated. b. Cut-through of the model after vessel radial expansion and release on the stent. c. Cut-through of the vessel with a plot of the compressive stress (3rd Principal Stress).

Fluid Dynamic Analysis:

The aim of this study was to compare different types of mechanical stimuli with local magnitude of ISR, to understand if there is any correlation between them and if any show particular significance. In order to obtain this comparison, fluid dynamic simulations were performed using the same stent geometry as starting point; the vessel was assumed to have the same radius (1.4 mm) and thickness (0.1 mm) as the structural analysis, with a length of 36 mm and a radius of curvature of 28 mm (Keller, Amatruda et al. 2014). This part of the study concerning the fluid dynamics immediately after stenting was performed by Brandis Keller at LaBS (Laboratory of Biological Structure Mechanics, Politecnico di Milano). *Figure IV.8.a* represents the boundary of the fluid domain, composed of the stent and vessel, which was obtained through an explicit dynamics approach (ABAQUS Explicit v6.10, Dassault Systems Simulia Corp., RI,USA) (Morlacchi, Keller et al. 2011). ANSYS CFX v.13.0 (Ansys Inc., Canonsburg, PA, USA) was then used for the fluid dynamics simulations. A hybrid meshing of the fluid domain was chosen (*Figure IV.8.b*). The assumptions used were: time-dependent simulation; blood considered as an incompressible fluid; the near-wall behaviour described by the Bird-Carreau constitutive law (Seo, Schachter et al. 2005); fully-developed parabolic flow waveform at the inlet and zero relative pressure at the outlet; no-slip condition with vessel/stent boundaries.

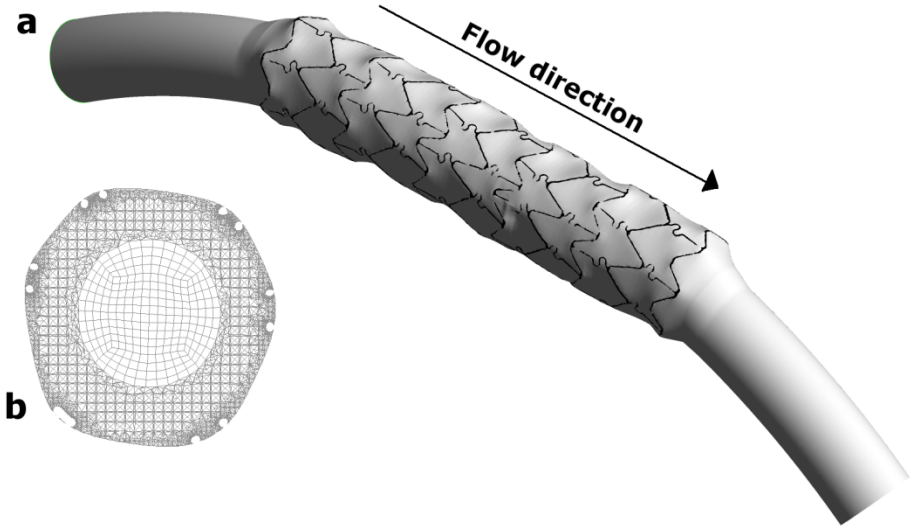

Figure IV.8 – a. Geometry of the boundary condition used for CFD simulations. b. Cross-section of the hybrid meshing for CFD. Adapted with permission from (Keller, Amatruda et al. 2014).

Results

The results of the fluid dynamics and solid mechanics models based on the 3D uCT data models are presented in *Figure IV.9*: here both FEM and CFD contour plots are presented to show the correspondence between the 3D uCT data (*Figure IV.9.a*), the structural analysis (*Figure IV.9.b*) and the fluid dynamics simulation (*Figure IV.9.*c). This allows comparison of localization of fluid and structural stress concentrations with the results of the NIT distribution obtained from the histological images (*Figure IV.3*).

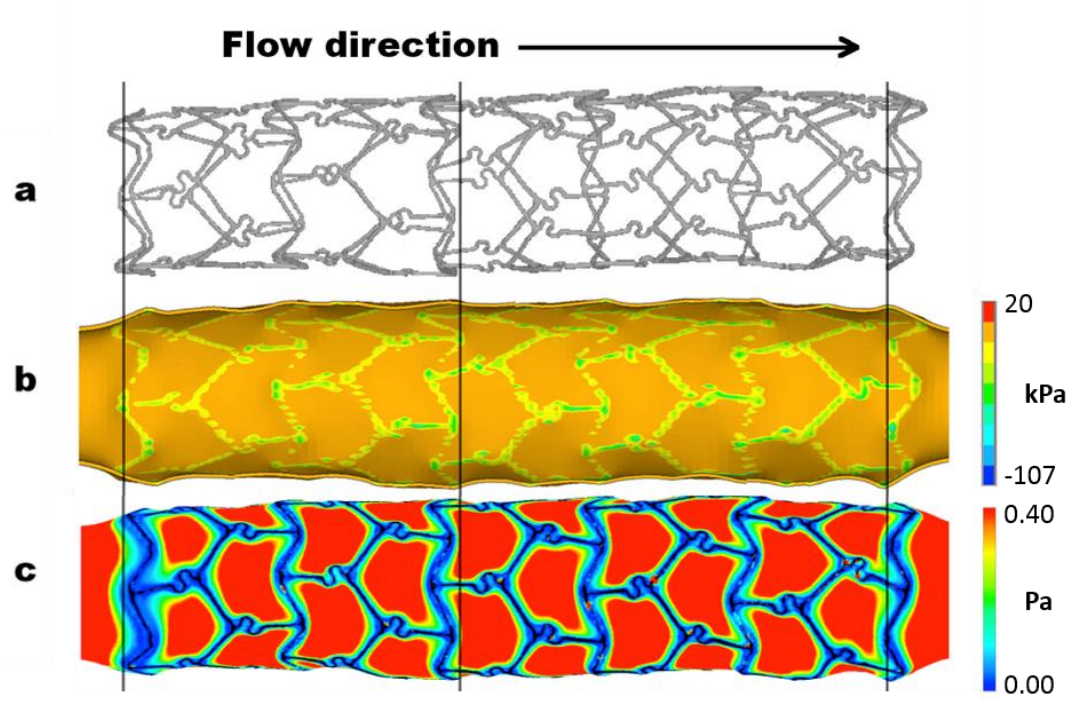

Figure IV.9 – 3D stent geometry (a), compressive stress contour plot from structural simulation (b) and wall shear stress contour plots from fluid dynamics simulation (c). Adapted with permission from (Amatruda, Bona Casas et al. 2014).

The results presented in this section will focus mainly on the structural results, first analysing the distribution of the compressive stress in comparison with histology, then describing a different method to post-process data (calculating the compressive force in the area of the stent strut) and finally comparing these results with both histology and with results obtained from post-processing of the fluid dynamic simulation.

Structural analysis

Seven simulations of vessel sections at different axial locations were performed to obtain stress data around the circumference of each cross-section, these axial locations correspond to the location of each of the histological images in *Figure IV.3*. The assumption for this model is that the injury provoked to the vessel wall by the expansion of a stent is related to the local compression in certain areas, specifically

behind the stent struts. For this reason, the measure that was chosen for analysis is the compressive stress, to determine the injury caused by the expanding stent, in the form of 3rd Principal Stress, as introduced in Chapter 3.

One of the first observations arises from comparison between the 2D model presented in Chapter 3 and the 3D model of this Chapter as shown in *Figure IV.10*.

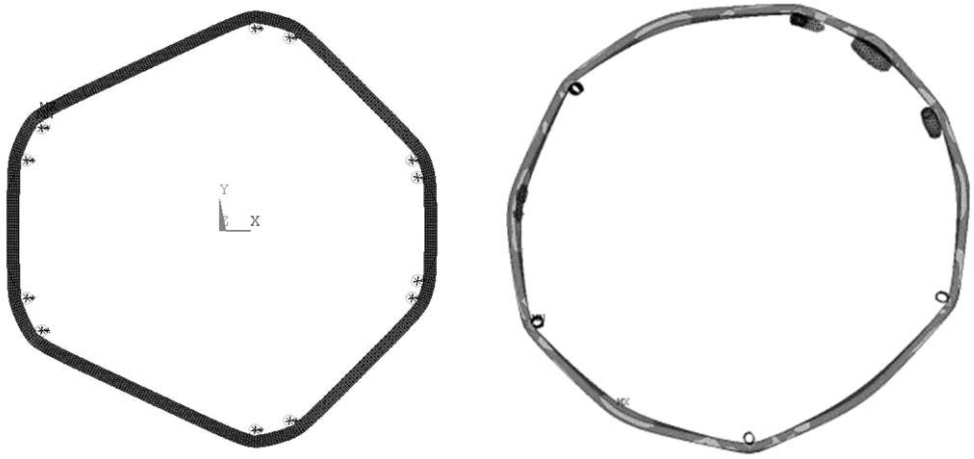

Figure IV.10 – Comparison between the 2D model of Chapter 2 and a cross-section of one of the 3D models.

Although the two models share the same vessel geometry, material model, similar expansion ratio, stent strut dimensions and distribution, the post-stenting vessel morphology presents a noticeably different appearance. The final shape of the 3D model shows a much more circular section, with much lower focal bending effects than its 2D counterpart. The reason can be found in the presence of struts in the out-of-plane regions of the 3D model, which influence the behaviour of the wall in the adjacent regions. The result of this is an increase of hoop strain over the whole geometry, and reduced regions of focal bending observed in Chapter 3. This first result already shows the importance of considering the full 3D geometry when recovery of a realistic distribution of stresses is required to assess the cellular response.

Compressive stress results

Contours of the compressive stress results are shown in *Figure IV.9.b*. This figure was obtained by combining the 3rd Principal Stress plots of the seven models: the agreement in stress results in the overlapping sections of the plots provides further reassurance of the low impact of the boundary conditions on the results in the central sections of the model. Arguably the concentration of the stress contours plot follows the pattern of the stent struts.

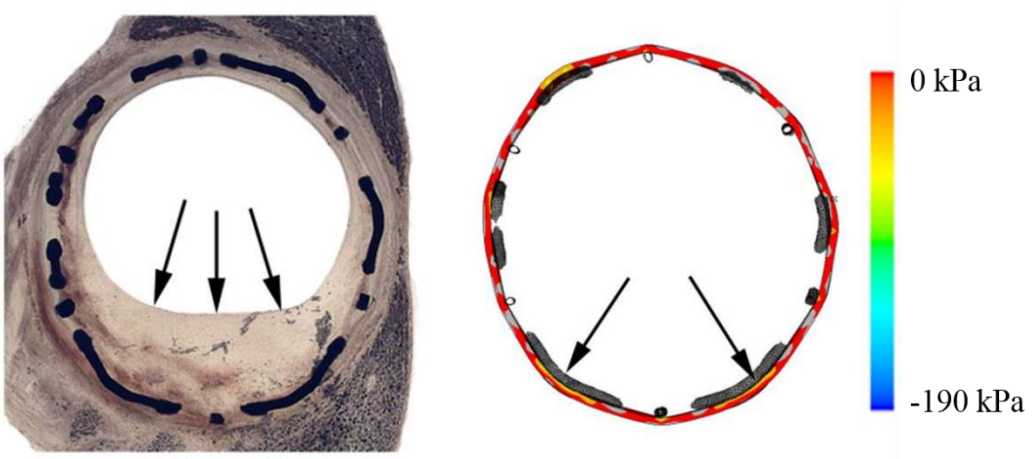

Figure IV.11 – Comparison between histological image and compressive stress plot on the cross-section of the relative model at the corresponding location. Arrows indicate the stent struts with the highest value of NIT on the left and with the highest values of compression on the right.

A more detailed analysis of the stress results was performed for each histology slide, comparing the stress distribution at the centre of each axial model location with the corresponding histological image. An example is reported in *Figure IV.11*, which shows the most proximal slide from *Figure IV.3*. The arrows on the left indicate the struts which correspond to the highest values of NIT and the arrows on the right indicate the struts where the highest values of compressive stress was reported.

The observation of contour plots is not the optimal way to establish how stresses vary from one location to the other, as each contour indicates a range of values. For more quantitative comparison, nodal results of the 3rd Principal stress

were exported for these cross-sections, selecting the inner nodes at the vessel lumen, for plotting against *NIT* values. These data are reported in *Figure IV.12* for the same slide shown in *Figure IV.11*.

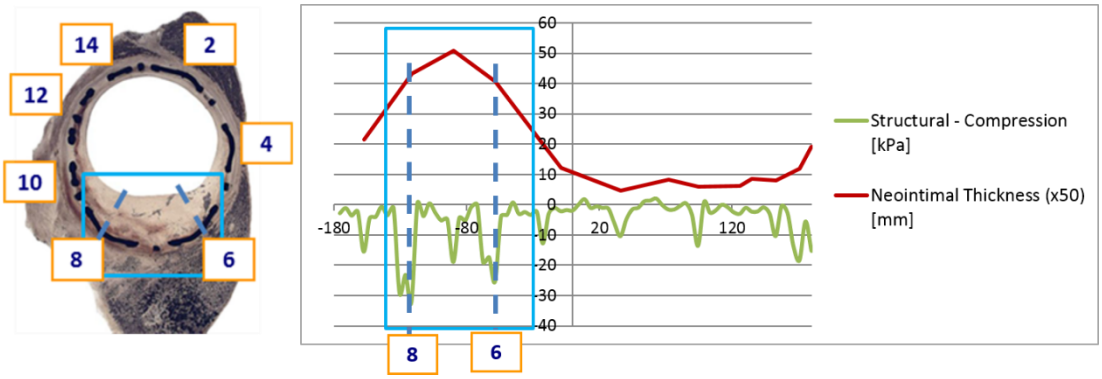

Figure IV.12 – Comparison between NIT and compressive stress values for one of the slides, reported through cylindrical coordinates, which corresponds to the histologic image shown on the right.

The numbers in the squares indicate the sequential numbering of the struts, where 1 is the top one and with clock-wise progression; the plot on the right follows the polar coordinates of the model, starting from the position at -180° (left) going anti-clockwise to 180°. Stress and *NIT* are reported on the same plot, the stress values are negative for convention reasons; from the plot peaks in stress can be clearly observed, corresponding to the stent strut locations. For this slide, there is clear correspondence between the highest values of *NIT* and the areas of highest stress, highlighted by the blue box, but this is not the case for all the slides, where values of *NIT* are lower.

In general, higher compressive stress values were found towards both ends of the stented region. The compressive stress values in areas between stent struts were found to be all around zero, and the peak value was evaluated for each stent strut. For the example represented in *Figure IV.12*, the compressive stress for strut number 8 is 32 kPa. The average value of these peaks amounts to 18 kPa, and the highest

values were found in the distal area, with a peak of 43 kPa, and in the proximal area, with a peak of 32 kPa. The most significant biological reaction was observed in the proximal area, whilst the amount of neointima was reduced in the middle and distal regions of the stented vessel.

The correspondence between areas of higher compressive stress and greater biological response in some regions of the stented vessel is consistent with the hypothesis that the injury provoked by the stent struts in the area of contact with the vessel wall influences neointimal growth (Boyle, Lennon et al. 2010). However, it is likely that the variation of stress in the region of each strut is influenced by the accuracy of the 3D stented geometry obtained from the micro-CT data. To reduce the influence of this effect results were obtained using a method which considers the effect of the whole contact area between each stent strut and the vessel, taking into account the full effect of the indentation of the strut, rather than considering the peak stress at a single point of the contact. For this reason, a method to integrate the stress related to a stent strut was developed, explained in more detailed in the next section.

Compressive force

To evaluate the structural stimulus for ISR development, the compressive stress was taken in consideration, but as it is possible to notice from *Figure IV.12*, there is not a single value of stress corresponding to a stent strut, but a distribution of values.

In addition, the process of identifying correspondence between histology images and the location of the struts in the finite element model may introduce uncertainties. The 3D geometry was reconstructed from the micro-CT of the stented vessel as a whole and the process of cutting slices to obtain the histological images may introduce small deformations of the stent struts (*Figure IV.13*).

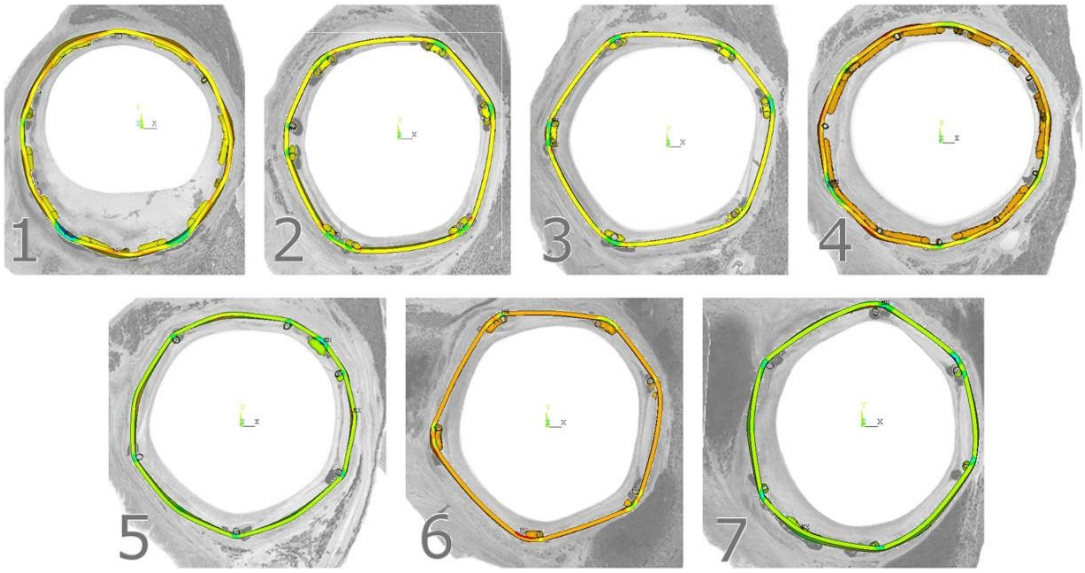

Figure IV.13 - Comparison between FEM images and correspondent histological images: it is easy to find the matching of the position of the stent struts, but in some cases there is a slight displacement.

Therefore, the use of the peak stress value to assess the structural stimulus can generate problems when there are several struts in a small area and can be very dependent on the accuracy of the segmentation of the stent geometry and on the smoothness of the meshing of the 3D stent geometry.

To provide a more accurate estimation of the local effect of each strut on the vessel wall, considering the total contact area, the contact force, *CF*, of each strut was computed. The 3rd Principal Stress, which in this case corresponds to the radial compression, was integrated over the region local to the stent strut position. The axial length of this region was chosen to be constant for all sections and strut locations. Following sensitivity tests, a local region of 0.15 mm about the central location were considered (*Figure IV.14*).

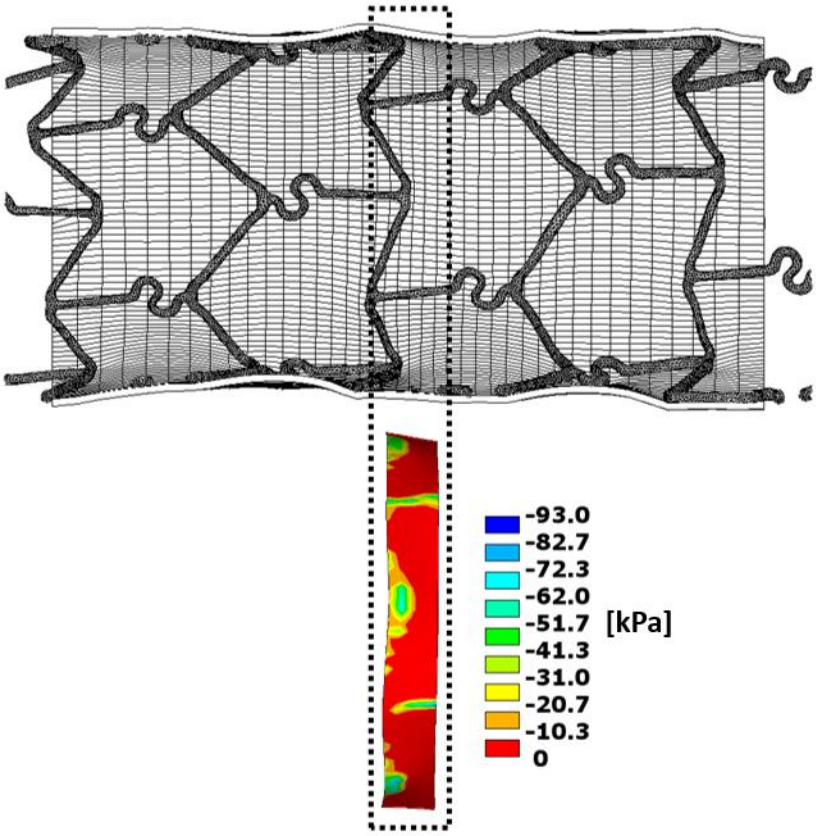

Figure IV.14 - Calculation of the compressive force: the third principal stress was integrated over the contact area of the strut, taking in consideration a thin strip of 0.15 mm in the axial direction and the contact area of the considered strut in the circumferential direction. Adapted with permission from (Keller, Amatruda et al. 2014).

The circumferential extent, on the other hand, was specific to the stent strut and was chosen so that the contribution of each strut to the compression of the vessel wall was considered.

Fluid dynamic analysis

Two indices were evaluated from the fluid dynamic simulation, at the locations of the histological images, time-averaged wall shear stress *WSS* and oscillatory shear index *OSI*. The latter is a measure of how, during pulsatile flow, the WSS deviates from its average direction and is given by equation 1.

$$OSI = \frac{1}{2}\left(1 - \frac{\left|\int_0^T \vec{\tau}_w dt\right|}{\int_0^T \vec{\tau}_w dt}\right) \quad [1]$$

To obtain an evaluation of these quantities for each stent strut, they were averaged in the region of each strut, considering the circumferential area of the contact and its neighbourhood, to the midpoint between the considered strut and its neighbour. The size of this region varies, given the asymmetry of the stent strut distribution. These two quantities were then compared with the *NIT* measurements for each stent strut location (Keller, Amatruda et al. 2014).

Statistical Analysis:

The three computational parameters (*CF*, *WSS*, *OSI*) were compared with the *NIT* values obtained from histology stent strut by stent strut. Linear regression was used for this purpose, and the coefficient of determination R_2 was obtained.

As a further examination, combinations of these indices were evaluated against *NIT*, in particular, *CF*/*WSS* and *CF* x *OSI* were analysed, as the current hypotheses are that high values of *CF* and *OSI* and low values of *WSS* could stimulate the growth. The use of similar combined indices has been found in literature, in particular from Chen *et al.* (Chen, Sinha et al. 2011).

In this way, it is possible to analyse the correlation of each these indices on their own and the correlation of multiple local stimuli with the level of neointimal growth, in the proximity of each stent strut.

Comparison between FEM and CFD results with NIT values:

The study was designed to obtain results for each stent strut in each of the seven histological images, resulting in 57 data points in total distributed along the axial and circumferential direction. For each strut location, four different types of data were considered: one measure of the amount of ISR, in the form of *NIT*, from the

histological images, and three measures of the mechanical stimuli on the vessel wall, both structural (*CF*) and fluid dynamic (*WSS* and *OSI*) obtained from computational simulations. *Figure IV.15* shows the distribution of these results strut by strut at three of the seven histology locations.

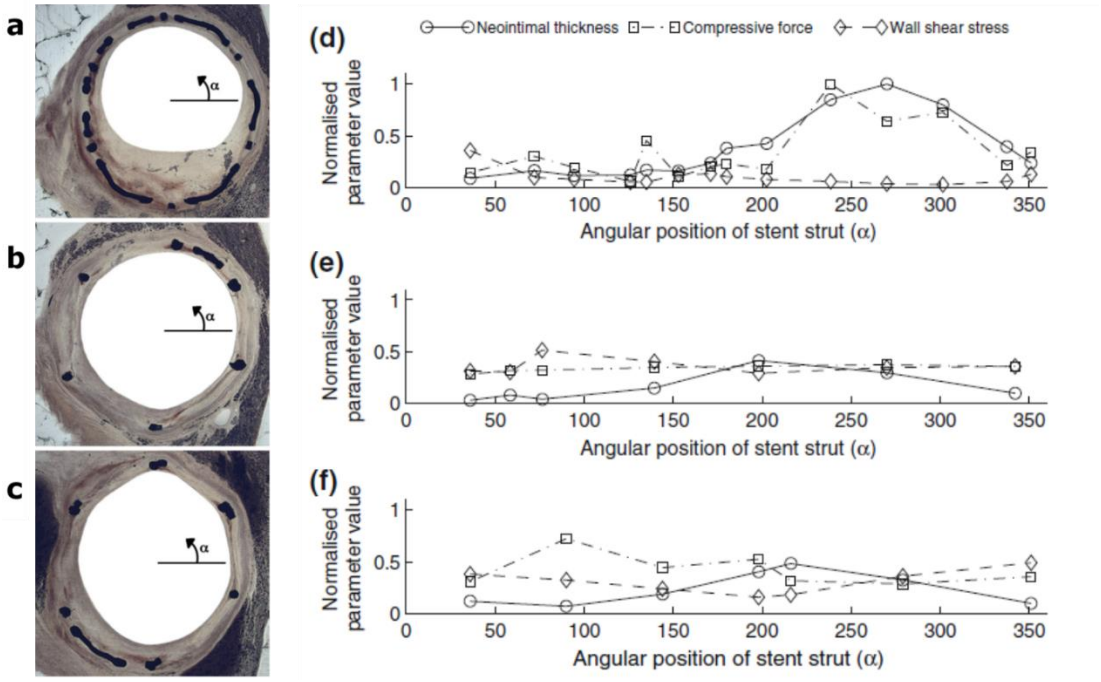

Figure IV.15 - Comparison of histological and computational results (d, e, f) obtained from the analysis of three locations (a, b, c) in different areas of the stented vessel: proximal region (a, d), middle region (b, e) and distal region (c, f). All the parameters have been normalised relative to their maximum value over the entire set of data along the whole model. Adapted with permission from (Keller, Amatruda et al. 2014).

These three locations correspond to the histological images 1, 4 and 7 of *Figure IV.3*, chosen to represent how the *NIT* changes from the proximal to middle and then distal regions. The percent restenosis by area at these locations is 41.8, 20.4, and 23.7%, respectively, with markedly higher growth in the proximal area.

In panels *a*, *b* and *c* of *Figure IV.15* the angular convention to locate the results shown in panels *d*, *e* and *f* is reported on the histological images. Panel *d*, *e* and *f* report variation in *NIT*, *CF* and time averaged *WSS* strut by strut with values normalised to the highest value of each parameter within the whole model. The *x*

axis of these plots represents α, the angular position of each strut in polar coordinates, which allows histology results to be compared directly with the computational results.

The complete set of results for all 57 data points at every strut location was analysed through linear regression and is reported in *Figure IV.16*.

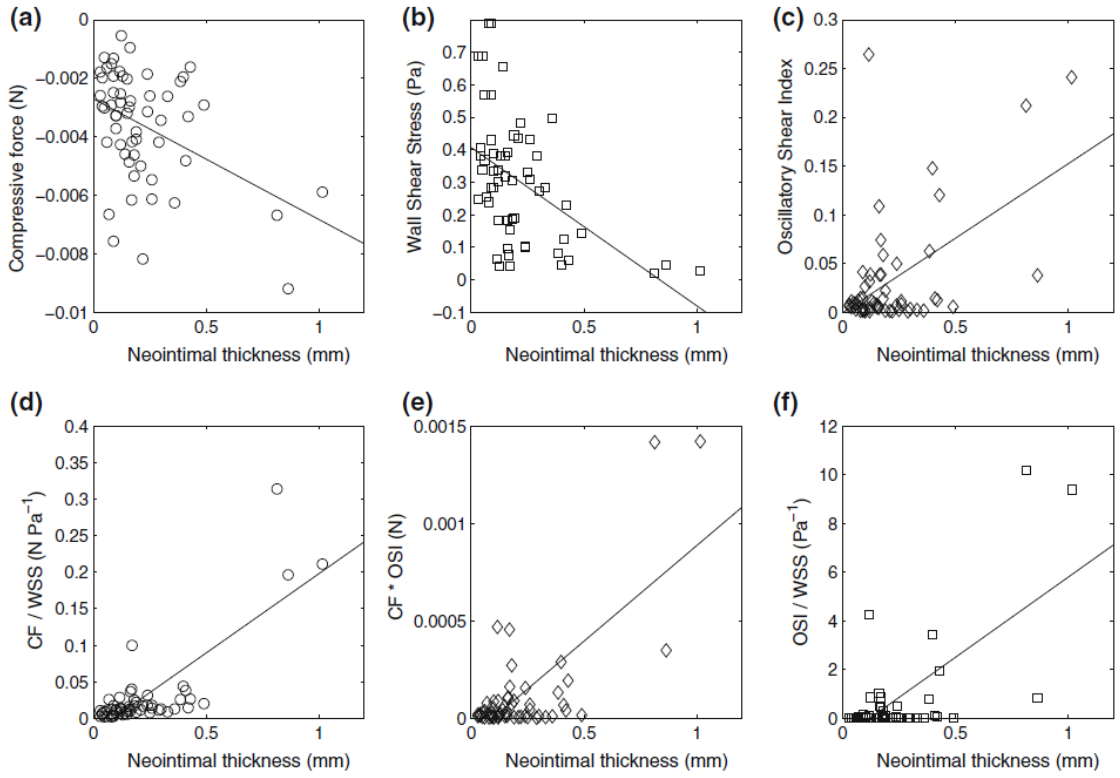

Figure IV.16 - Linear regression plots between for the neointimal thickness NIT against the mechanical stimuli, in terms of compressive force CF (a), wall shear stress WSS (b), oscillatory shear index OSI (c), and combinations of these: CF/WSS (d), CF*OSI (e) and OSI/WSS (f). Reproduced with permission from (Keller, Amatruda et al. 2014).

The first row of plots show each of the stimuli obtained computationally plotted against neointimal growth, with structural stimulus *CF* in *Figure IV.16.a* and the haemodynamic parameters, *WSS* in *Figure IV.16.b* and *OSI* in *Figure IV.16.c*. The second row of plots show three different combinations of stimuli plotted against neointimal growth *CF / WSS* (*Figure IV.16.d*), *CF x OSI* (*Figure IV.16.e*) and *OSI / WSS* (*Figure IV.16.f*). The choice of these combinations comes from the hypotheses

that high values of compression provoke a higher injury to the wall, while lower values of wall shear stress and higher values of OSI would increase cellular activity. The use of combining indices by multiplying or dividing them in order to evaluate their cooperation to the final outcome, specifically ISR, has been used by other authors at the level of individual cross-sections of the stented vessel (Chen, Sinha et al. 2011). The linear regression values for the plots presented in *Figure IV.16* are reported in *Table IV.2*: *m* represents the slope, *b* the intercept and R_2 the correlation coefficient.

Table IV.2 - Linear regression for each of the values against NIT, correspondent to plots shown in Figure IV.16. Reproduced with permission from (Keller, Amatruda et al. 2014).

	CF (N)	WSS (Pa)	OSI (%)	CF/WSS	CF*OSI	OSI/WSS
m	0.004	-0.53	0.15	0.22	0.001	6.58
b	0.003	0.44	0.001	-0.02	-9e-5	-0.79
R^2	0.19	0.25	0.28	0.64	0.52	0.47

Discussion

In the previous section, the data processing for an *in silico* model of stent-vessel derived from an *in vivo* animal model was presented, including: topologic correspondence of mechanical stimuli with the histological images; visual observations of the morphology of the post-stenting wall and neointimal growth; post-processing of the results obtained using the finite element method, from analysis of the compressive stress to the calculation of compressive force and its correlation with neointimal growth, including the concomitant effect of the change in fluid dynamics.

Obtaining a 3D geometry of the stent through micro-CT provided data to ensure an accurate matching not only between the axial locations of the cross-

sections in the two computational models and the relative histological images, but also of the stent strut locations in these cross-sections. The 3D stent geometry data are also essential to undertake analyses of the post-stenting mechanics, without assumptions relating to the stent/balloon interactions during deployment.

Comparing the cross-sections of the 3D analysis with the results obtained for the 2D models from Chapter 3, a difference in morphology is noticeable, with a rounder shape for the 3D model: this is due to the out-of-plane effects and the influence of neighbouring struts. These results demonstrate how a realistic interaction between the stent and the vessel results in less accentuated local bending of the vessel wall in region of each strut, and higher hoop strains.

The development of in-stent restenosis is not included in the finite element model at this stage and the vessel is assumed to be healthy, representing the stress distribution in the vessel wall immediately after stenting in the porcine model of ISR. Based on the localisation of biological response in the early stages after stent implantation in the region of the stent struts (Malik, Gunn et al. 1998), the radial compressive component of stress was considered as a potential stimulus for the development of ISR.

The 3rd Principal Stress, which corresponds to compressive stress, was analysed along the circumference in the axial locations corresponding to each histological image location. This analysis provides an insight of the influence of the strut distribution in determining the stress distribution in the cross-section. The stress peaks match the strut locations, while values around zero are found in area without struts. Higher stresses were found at the ends of the stent, which agrees with the location of ISR observed in clinical studies (Moore and Berry 2002). However,

the method to evaluate the load due to the stent on the vessel is not very accurate: on the one hand, the load is not imparted from the strut to the vessel on one single point but on an area; on the other hand, the results might be influenced by a slight deformation of the struts during the slice cutting process and the accuracy of the segmentation. Therefore, the integration of the stress over the area of contact between stent and vessel is proposed.

Compressive force (*CF*) has therefore been calculated for the same locations, i.e. for each strut in all seven cross-sections, over the circumferential extent of the contact for each strut and a constant axial distance. The compressive force results again show higher values at the ends of the stented vessel, but for these results the values in the proximal area were markedly higher, which corresponds to the region where the most significant neointimal growth was found.

The data obtained from the two computational models and the histology processing were compared using statistical analysis, discussion of the *CF* results and their correlation with *WSS*, *OSI* and *NIT* is provided below.

The *CF* is higher at the proximal and distal ends of the stented vessel than in than middle region, as shown in *Figure IV.15*. The greatest values can be found in the proximal region, in correspondence with high values of *NIT* (*Figure IV.15.d*), while this correspondence is not so strong in the distal area of the stented region (*Figure IV.15.f*). The correlation between *CF* and *NIT* was higher for the proximal area, which includes slides 1 and 2, with a value of $R_2 = 0.51$, while when the whole model is taken into consideration, only a value of $R_2 = 0.19$ is reported.

As previous described, the compressive force was preferred over compressive stress as it considers the contact of the whole strut rather than a single point of the

area: this avoids slight inconsistencies between the stent strut locations between the structural model and the histologic images and it overcomes the sensitivity to the smoothness of the meshing of the stent, dependent on the accuracy of the micro-CT data segmentation.

Similar studies from other groups have also investigated the correlation between structural stimuli and biological response (Chen, Sinha et al. 2011). In these studies the circumferential stress was considered for stented and non-stented regions of the vessel, averaged over each cross-section, using an idealised stent geometry deployed at a number of expansion ratios. The difference with this study is in the averaging process: in the work reported in this Chapter the aim is to evaluate stimulus and reaction locally at individual stent struts. The circumferential stress was analysed, but the local variations of this value are not as significant as the compressive stress.

The CFD results show a similar trend to the compressive force values. The values considered to stimulate neointimal growth are $WSS < 0.4$ Pa and $OSI > 0.2$: the correlation between these values and high *NIT* is predominant in the proximal region of the model, where the highest values of *NIT* were observed. In fact, at the entrance of the stented vessel, the physiological curvature of the vessel induces higher blood velocities in the upper area (top cross-section of *Figure IV.8.a*), which results in recirculation areas in the lower area (bottom cross-section of *Figure IV.8.a*) and therefore low values of *WSS*: a similar profile was indicated in other studies (LaDisa, Olson et al. 2005), and such flow features have been linked to increases in both platelet and inflammatory cell activation (Kroll, Hellums et al. 1996, Duraiswamy, Jayachandran et al. 2005). This supports the correspondence of this

area with the highest values of *NIT*. However, also in this case the correlation of each of the two quantities with the *NIT* values is not particularly high when the whole model is considered, with R_2 = 0.25 for *WSS* against *NIT* and R_2 = 0.28 for *OSI* against *NIT* (*Table IV.2*).

The correlation of each of the stimuli with the biological reaction, at each individual strut, was found to be higher in the proximal region of the stented vessel, in correspondence of the most noticeable neointimal thickening. This relationship becomes weaker when the whole length of the stent is considered, resulting in low R_2 values. However, when structural and fluid dynamic indexes are combined, the correlation becomes more substantial, as can be seen from *Figure IV.16*, where R_2 = 0.64 for *CF/WSS*, R_2 = 0.52 for *CF*OSI* and R_2 = 0.47 for *OSI/WSS* as reported in *Table IV.2*. Values of *CF* at the level of the strut are higher at both ends of the stent because of the sudden change of mechanical properties between stented and non-stented vessel regions (Moore and Berry 2002), while the abrupt change in *WSS* due to the skewing of the velocity profile happens mainly at the proximal end, and the effect decreases along the longitudinal length of the stent: the combination of the two effects is a possible explanation for noticeably higher values of *NIT* found in the proximal end of the stented vessel.

These results are consistent with findings reported by Chen *et al*. (Chen, Sinha et al. 2011): these suggest that mechanical stimuli contribute to the development of neointimal growth in each of the two forms, structural and fluid mechanical, and that the combination of the two may amplify the tissue healing process, promoting the progression of ISR.

This study shows how utilising a realistic 3D deployed stent geometry it is possible to gain information about both structural and fluid mechanics in the neighbourhood of the stent struts following stent deployment, and to compare the results directly to the biological response for each location through 2D histological sections, giving the chance to evaluate the influence of the loads to the neointimal growth, taken singularly or combined.

The analysis of fluid dynamics immediately after stenting and its correlation with neointimal growth was performed on patient-specific post implantation geometry from Sanmartín *et al*. (Sanmartin, Goicolea et al. 2006), and a similar negative correlation between WSS and NIT was found: however, the values of the correlation found are not particularly high, indicating that other factors might contribute to the ISR process. The influence of the stent geometry has not been reported.

The influence of the mechanical stress was analysed and compared with *in vivo* ISR data from animal models in a study from Timmins *et al*. (Timmins, Miller et al. 2011). In this case, circumferential wall stress was analysed to compare the potential of two different stent designs to damage the internal elastic lamina. As the expanded stent model is idealised, the values reported are peak values and no analysis at the strut level is performed.

A study from Chen *et al*. (Chen, Sinha et al. 2011) merges all these elements, *in vivo* measurements on animal models, structural (circumferential stress) and fluid dynamic values (WSS, WSS gradient, OSI) from computational studies. The values are averaged at each cross-section considered, as the aim is to compare various

expansion ratios, the strut level is not considered in this work. Moreover, the stent employed is an idealised stent, rather than a realistic expanded geometry.

The aim of this work is not to compare different stent geometries, but to propose a method to study the influence of various mechanical stimuli on the process of in-stent restenosis immediately after stenting. As it was observed that the growth, in its initial phases, appears to be confined in the neighbourhood of the stent struts (Malik, Gunn et al. 1998), the focus was to evaluate what happens locally to each strut. Therefore, the use of *in vivo* 3D micro-CT to capture the realistic expanded stent geometry, including asymmetry and irregularities, provides a more accurate estimate of the variation of these values in stents implanted *in vivo*. Furthermore, the availability of histological images 14 days post-implantation from the same *in vivo* model allows a numerical interpretation of the computational results, through statistical comparisons, not only of each stimulus on its own, but of a combination of solid and fluid components simultaneously, for each stent strut over every cross-sections.

As this work only proposes a method, further work needs to be done in order to validate the findings described here, by applying the same methods over several data sets from the porcine restenosis model and by comparing the results with observations of clinical ISR.

Follow-up studies and development of such data-driven computational methods could improve the knowledge and therefore the possible treatments of ISR, possibly encouraging the study of patient-specific cases.

A time-point of 14 days was chosen to allow significant ISR to be measured, avoiding the effect of vessel remodelling which may be observed at later time-points,

as described in Chapter 1. As the models reported here consider only the mechanics immediately post-stenting, comparison with early time-points may be more appropriate, as computational simulation based on the geometry of a healthy vessel just stented might not be able to be related to the effects of later evolution of neointimal growth.

The evolution of ISR has been modelled by Tahir *et al*. (Tahir, Bona-Casas et al. 2013) who proposed a simulation of neointimal growth based on a cellular model which captures the evolution of fluid dynamics stimuli and uses this as a stopping criteria for ISR, as described in more detail in Chapter 2. Other studies use the structural stimulus to initiate growth, like Boyle *et al*. (Boyle, Lennon et al. 2013), also described in Chapter 2, but the evolution of the stress is not considered and the both cell migration and stopping criteria for growth are driven by cellular rules alone.

The exact correlation between vessel stresses following stenting and cellular reactions is not completely understood due to the complexity of the phenomenon, which requires detailed models of the vascular wall which include the evolution of the wall geometry itself, through cellular growth, and the consequent variations in the vascular stress. A preliminary 2D model of ISR that represents the structural stress of the vessel wall and its evolution within the neointima is proposed in the next Chapter.

The work reported in this Chapter has shown the benefit of combining results from multiple simulations using the same reference geometry, such as an increased chance of validation and of evaluation of the combined action of multiple stimuli on the same phenomenon. This also applies to the whole framework described at the beginning of the Chapter and illustrated in *Figure IV.1*, the combination of all data

from several simulations based on a common experimental framework enhances the impact of the findings, compared to individual modelling approaches, when attempting to understand the dynamics of ISR.

The study described in this Chapter has some limitations: in particular these results are based on data derived from a single stent deployment in a single animal, which does not account for variability between animals and stent implantations. The advantage of the method is that it considers the stimuli at each individual stent strut, providing a sufficient number of data points to investigate variation of these parameters within a single experiment. The method may also capture variability due to the detail of stent deployment that is lost using approaches which average stimuli at each axial location (cross-section). The method proposed in this study could be used to guide the design of future animal studies to examine the progression of ISR at various time-points post-stenting and at more expansion ratios corresponding to different injury levels.

The material model used to describe the properties of the coronary artery in this study was isotropic. Other studies report the use of more refined models, which represent the characteristics of each single layer of the vessel wall (Conway, Sharif et al. 2012). Nonetheless, it is possible to assume that a change in properties through the thickness will have an influence mainly in the distribution of the stress in the radial direction, rather than a significant influence on the variation of stress in the circumferential direction, which is the main interest in this study.

Some studies have considered more detailed geometrical features of arteries, such as their tapering from proximal to distal areas (Timmins, Meyer et al. 2008). The effect of the tapering of the vessel has not been considered in this study. This

effect is more pronounced in arteries such as carotid artery and femoral arteries, where the change of diameter is noticeable over the length of a stent. However, a degree of tapering is also found in coronary arteries and should be considered to provide a complete description of the stress distribution in a stented vessel. The degree of tapering of the *in vivo* model is not known, consequently tapering was not considered to keep the model simple and remove dependence on the choice of an additional parameter. Tapering towards the distal end of the vessel would tend to increase the values of compressive stress at the distal end of the vessel relative to those at the proximal end, but would have little influence on the fluid dynamics results.

The process of statistic evaluation of the results could be improved by normalisation of the values, as *CF* and *WSS* have units while *OSI* is dimensionless: this would allow a better comparison of the values. However, this method was used here in order to allow direct comparison with another study found in the literature (Chen, Sinha et al. 2011).

This study does not require the full process of stent deployment to be simulated as the use of the 3D micro-CT geometry defined the stent geometry as a rigid contact surface, without considering its stress state, which is not the focus of this study. In the method described, the locations of the 2D histological images are manually matched to their position in the 3D geometry. A more robust method would include the development of imaging techniques to provide the 3D geometry and volumetric distribution of ISR. However, the study uses histological data provided by a different group from different studies; the more robust method described is suggested as a possible improvement of the study.

As the study considers both structural and fluid effects combining the simulation methods to consider fluid-structure interaction analysis would provide more detailed understanding of the mechanical environment. However, such an approach would require careful consideration of the assumptions relating to model boundary conditions and would result in significant increase in computational cost.

SUMMARY

This Chapter presents a method proposed to investigate both structural and fluid dynamic loads after stenting and their influence on ISR at the level of individual struts, as they have been both recognised to be contributing factors to this phenomenon.

The main issue related to the study of ISR that emerged in this Chapters is how it is dependent on multiple factors. Taking in consideration the mechanical stimuli only, on the one hand it is needed to understand how they change the local conditions immediately after stenting, in order to have an insight of the initial triggers of neointimal growth; on the other hand, it is important to keep track of how they change with time, in order to elaborate models and gain some understanding of how these stimuli affect the growth, its shape and the way it stops, by comparing the results with histological images of ISR. This approach is proposed in the next Chapter, where a model of evolution of ISR is proposed by combining a continuum model to detect the structural mechanics of the vessel, which is used as stimulus for a cellular model of neointimal growth; the change of the lumen geometry has an effect on the structural stimulus, so the stresses are investigated again through the continuum model and new information is sent as a feedback to the cellular model.

CHAPTER V – MODELLING ISR

INTRODUCTION

The previous Chapters of this thesis introduced the problem of in-stent restenosis and prior work that has been made to understand this phenomenon. All simulations in previous Chapters represent the structural environment of the vessel immediately after stenting. In this Chapter, a model of in-stent restenosis evolution is presented. First a cellular model of growth is developed, based on a geometry similar to that of the 2D finite element model presented in Chapter 3 and using the stress data to inform the initial stimulus for cellular growth. The results of this cellular model are then critically analysed in comparison with histological images of neointima development within a porcine model. Second, a refinement of the evolution of cellular growth is proposed, which includes feedback between the cellular model and the finite element model. An update of the geometry of the neointimal region is passed to the finite element model to compute the subsequent change of load on the neointima, and therefore on the cells, during the growth phase.

5.1 DEVELOPMENT OF A CELLULAR MODEL OF ISR

As described in preceding Chapters, interest in the investigation of in-stent restenosis (ISR) does not only relate to the burden of ISR on health systems. The fact that the factors triggering the phenomenon, its initiation, its evolution and particularly its end, are not yet completely understood creates a need for deeper understanding of the fundamental biological processes which drive the process. This could help in the development of more effective treatment approaches and more advanced stent designs.

Evidence has been provided of links between mechanical stimuli and changes in cell behaviour, influencing cell phenotype: various studies suggest that, when smooth muscle cells experience mechanical stimuli within the physiological range, the contractile phenotype is maintained, with promotion of a synthetic phenotype as cells are exposed to stimuli outside this range (Rensen, Doevendans et al. 2007). Particular mechanical stimuli include the influence of wall shear stress on endothelial cells and the effect of structural compressive stress on smooth muscle cells (SMCs). This thesis focusses on the first principal stress in the neointima, due to stretching of the ECM under pulsatile pressure. This stimulus has been shown to direct cellular motion (Tambe, Hardin et al. 2011) and its use to direct neointimal growth represents the novel aspect of the current study. In common with other authors (Zahedmanesh, Van Oosterwyck et al. 2012, Boyle, Lennon et al. 2013), the contribution of compressive stress in the artery wall due to compression by the struts provides initial stimulus for tissue growth.

ISR Cellular models reported in the literature are developed using either a lattice or a non-lattice approach. The lattice approach is computationally less

expensive, dividing the spatial domain into a grid and allowing limitation of the number of variables to the number of lattice points (Boyle, Lennon et al. 2010); with a non-lattice method the spatial domain is continuous, the cells have a volume, and the algorithms required are more computationally demanding (Zahedmanesh, Van Oosterwyck et al. 2012, Tahir, Bona-Casas et al. 2013).

As introduced in Chapter 1, adult SMCs can be found in one of two phenotypes, contractile or synthetic, according to the environmental stimuli, as they are not terminally differentiated; in reality, there is a spectrum of transition from one phenotype to another, with many intermediate phenotypes (Rensen, Doevendans et al. 2007). Most ISR models, though, simplify the cell functions through the two phenotypes as non-active (contractile) or active (synthetic) (Boyle, Lennon et al. 2011, Zahedmanesh, Van Oosterwyck et al. 2012, Tahir, Bona-Casas et al. 2013). For the scope of this model, the cell will be simply represented as either contractile or synthetic.

In the section below a model of in-stent restenosis is set-up using an initial geometry and a stress stimulus based on the results of the 2D FEM simulations reported in Chapter 2, without update of the stress stimulus. The local stress concentration beneath the stent strut provides a stimulus for a model of cellular evolution which includes proliferation and migration of SMCs and ECM synthesis.

An initial investigation of the influence of various parameters on the behaviour of the cellular model was performed in order to establish an initial set-up of the full model within the 2D stent/vessel geometry. The description used for this model is mainly phenomenological, as mechanistic modelling of cellular evolution requires consideration of a considerable number of processes over a range of scales,

which lie outside the scope of this study. The primary aim of the model is to understand the typical pattern of growth generated using a cellular model alone and how this compares with results obtained from *in vivo* biological models. Comparison of these results with those presented in the second section of this Chapter suggest how the evolution of cellular growth might be influenced by changes in the stress acting on the cells over time.

Methods

Cellular model: The cellular model of smooth muscle cells (SMCs) populating the coronary artery was developed in Matlab. A Cartesian lattice divides the space corresponding to the geometry of the vessel and lumen, into discrete points, which can contain a single SMC and a certain amount of extra-cellular matrix (ECM). The spatial domain represents a 1/12 symmetry of a stented vessel cross-section, with a dimension of about 2 mm^2.

A set of matrices are used to store variables at each lattice point of the grid. For example, geometry data are mapped through the use of Cartesian coordinates x and y and polar coordinates r and ϑ which are stored in four matrices. Another set of matrices describe the "content" of each lattice point, such as the presence of ECM (fraction between 0 and 1), the presence of SMCs (0 or 1), and whether this discrete part of the space is part of the vessel region, lumen or the boundaries of the model.

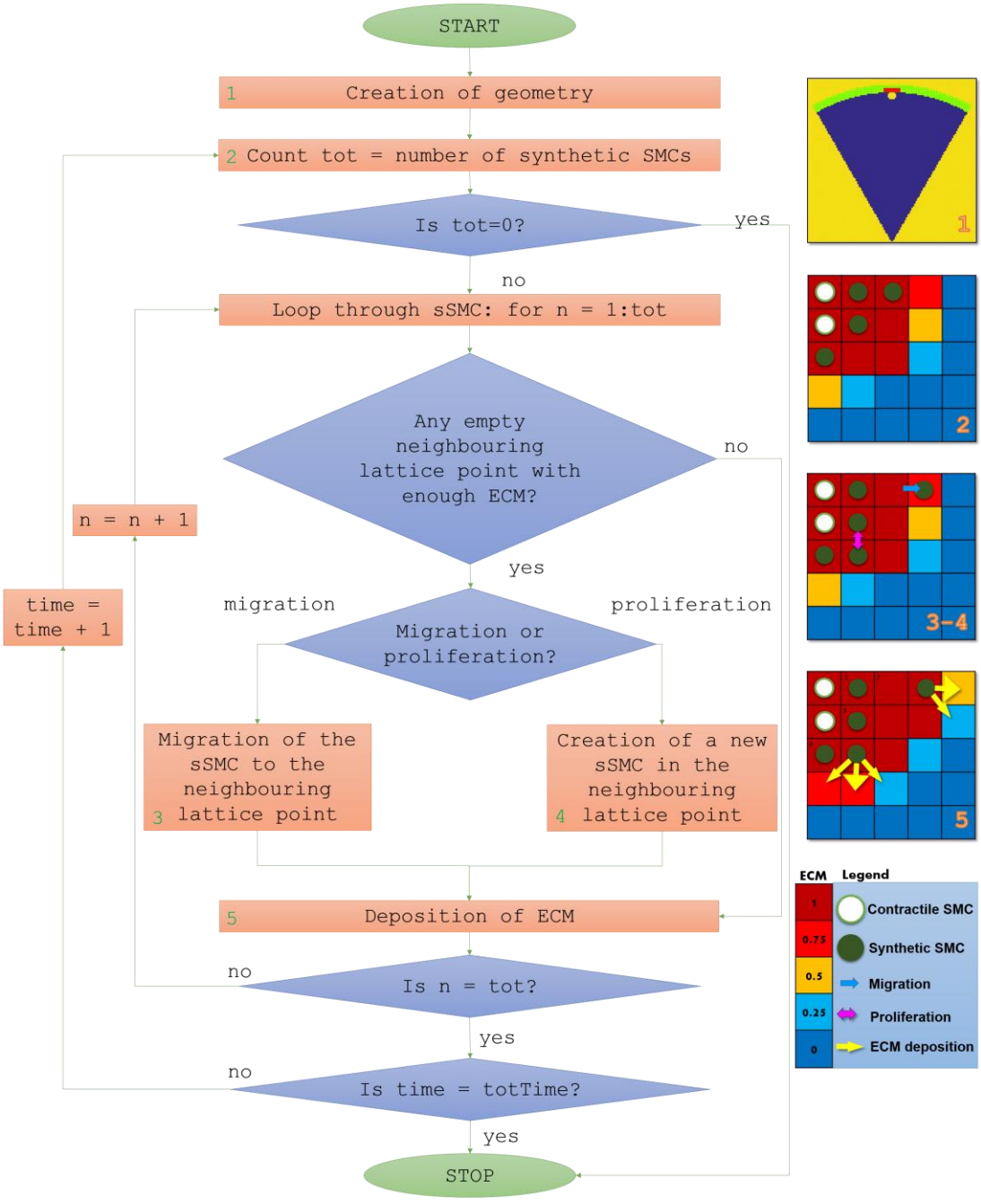

Figure V.1 - Flowchart representing the algorithm. The main phases are represented on the right-hand panel, as follows: 1. Creation of the geometry and the lattice. 2. Iteration to research the SMCs in contractile state. 3 and 4. Migration or proliferation of SMCs into vacant locations with sufficient ECM. 5. Deposition of ECM.

At each time-step the algorithm operates over all lattice points scanning through all locations to create a list of those that respect a certain rule, i.e. they are "stressed". For each location, it explores the state of its neighbourhood, in order to detect empty lattice points with sufficient ECM to host a new cell; then it checks whether a cell can proliferate, migrate or produce ECM both at the specific lattice point and for the surrounding ones. The cell is therefore moved, divides or is just left where it is. After this the cell produces ECM and the model goes on to analyse the next cell in the list. The flowchart in *Figure V.1* shows the algorithm step by step.

The components of the model are described in the next section which also explains the rules and the choice of parameters in further detail.

Components:

Lattice - the lattice is a grid that divides the considered 2D space into elements which each represent a lattice point. In this Chapter, the model represents a region of a 2D cross-section of the stented vessel, similar to the FEM representation presented in Chapter 3. The area occupied by the grid is rectangular rather than circular and includes: space outside the vessel, represented by inactive lattice points; vessel wall, populated by SMCs and ECM; the area occupied by the stent strut, which is also inactive, and the lumen, which initially contains empty lattice points.

SMCs - SMCs represent the cellular components of the model: each SMC occupies one lattice point, so their location in space is determined by the layout of the lattice. SMCs can be one of two different phenotypes: contractile (cSMC) or synthetic (sSMC) (Boyle, Lennon et al. 2010, Tahir, Bona-Casas et al. 2013). As described in Chapter 1, under normal physiological conditions, the cells of a coronary artery wall tend to be in a quiescent, contractile state, through which the cell contributes to the

circulation through vasodilation and vasoconstriction. Cells switch to a synthetic state if the environment requires a "reparation" (Thyberg, Hedin et al. 1990), as in the case of excessive compressive stress, which can lead to vascular injury (Linder-Ganz, Engelberg et al. 2006): this induces a change in the characteristics of the SMCs with their shape changing from spindle-shaped to rhomboid and increases in proliferation and migration rates. At the same time mechanical forces enhance the production of ECM to repair the damaged tissue (Rensen, Doevendans et al. 2007). It has been reported in Chapter 1 that cyclic stretch also plays a role in mechanotransduction mechanisms. Its cessation in the vessel wall post-stenting has not been considered, while its presence in the neointima has been included in the model described in the second section of this Chapter. For the model developed in this Chapter, when a lattice point experiences a compressive stress higher than a certain threshold (σ_{min}) cells move from the quiescent, contractile state to the synthetic state.

ECM - Each lattice point also contains a certain amount of ECM, which is represented in this model as a value between 0 and 1, where 0 represents no ECM content, i.e. a space that is not part of the vessel, such as the lumen, and 1 represents a lattice point full of ECM. A certain minimum amount of ECM at a lattice point, called *base*, is required for a SMC to be able to migrate or proliferate to that location.

Cellular rules:

The model is constructed in Matlab R2014b. As mentioned previously, the model is represented by a set of matrices; at every time iteration, all SMCs are scanned in order to identify the subgroup of SMCs that are in the synthetic phenotype: if the group is not empty, the algorithm checks for each of these SMCs whether there are

neighbouring lattice points that are empty of cells but have enough ECM to host a cell (over the *base* value). When cells are in the synthetic state, they are allowed to proliferate, migrate and produce extra-cellular matrix.

In this initial model the migration or proliferation of an SMC has no directional preference between the available lattice points in the surroundings, all adjacent lattice points that do not contain an SMC and whose ECM content is equal or higher than the *base* value are considered suitable. Migrating or new SMCs maintain their synthetic status. For a given time-step synthetic SMCs can either proliferate or migrate, but cannot do both. The activity is dictated by a random number, *P*, and the specific probabilities are:

$P \leq PProb$ = cell proliferation;

$PProb < P \leq PMigr+PProb$ = cell migrates;

$P > PMigr+PProb$ = cell does nothing.

After checking the presence of suitable neighbouring lattice points and potential migration or proliferation, the cell can produce ECM. Whilst in the synthetic phenotype SMCs are assumed to produce an amount of ECM that is distributed within the surrounding space in an amount that depends on the distance of the centre of the lattice point from the centre of the SMC. For this reason, two values for ECM deposition for each time-step are used, depending on the relative location.

The model matrices are updated to reflect the creation of new cells, cell migration and the addition of ECM for the neighbouring lattice points and the algorithm considers the next SMC from the group of active ones; once this process has been completed for all cells, the new lumen area is calculated. This is then used to estimate the value of WSS, and a new time-step is started.

WSS calculation:

At the end of each time-step, the new lumen area is computed by detecting the number of all lattice points that have no ECM content *nLum* and multiplying it by the size of each lattice point *dx*: $ALum = nLum * dx^2$. Whilst a more accurate measure of WSS could be obtained from a 3D model, such as that described in Chapter 4, the aim of this computation is to provide an estimate of changes in magnitude of WSS following cellular growth. The shape of the lumen is assumed to correspond to a circular section based on the computed area to calculate the new inner radius of the vessel through $rLum = \sqrt{ALum/\pi}$. An average constant flow Q_{mean} of 50 ml/min was assumed. This value was chosen from observation of the plot of the flow waveform over a cardiac cycle obtained from a porcine coronary artery found in literature (Huo, Choy et al. 2009, Keller, Amatruda et al. 2014). A Poiseuille assumption was used assuming a parabolic velocity profile with the mean value $v_{mean} = Q_{mean}/ALum$ and the shear stress was calculated as $\tau = \mu * dv/dr$.

The process stops if the total time of the model is reached or if the group of active cells is empty. The WSS is calculated in parallel.

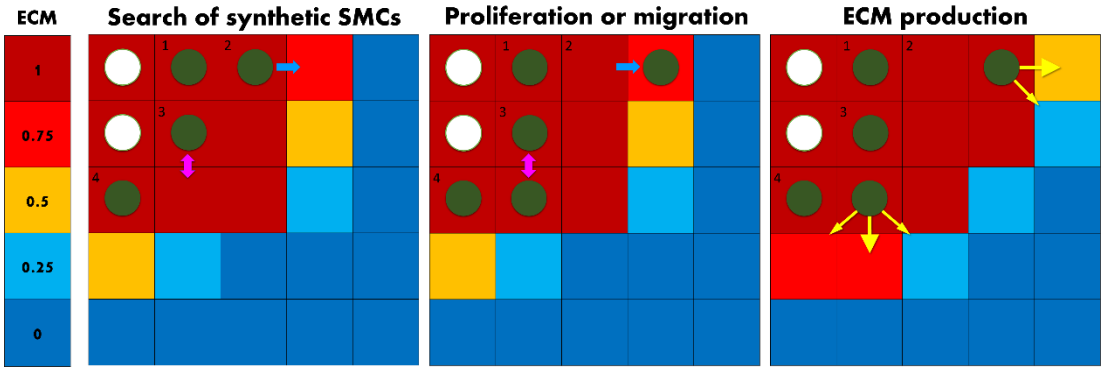

Figure V.2 – Algorithm steps: search for SMCs that are in the synthetic state (green dots) and have neighbouring lattice cells without a SMC and with enough ECM, represented by the grid colour (for this example, 0.75). Random choice of proliferation or migration with a specified probability, and ECM production.

Parameters - The duration of a single time-step was chosen as 24 hours. This is the same order of magnitude as a single cell cycle leading to SMC division which has been found to be around 32h for cultured porcine aortic SMCs (Le Breton, Plow et al. 1996). These timescales are consistent with those of ECM production, for although the first evidence of collagen production can be seen within a few hours, the creation of a pericellular network takes around 24h (Li, Van Den Diepstraten et al. 2003).

As already mentioned, SMCs change shape according to their state: this also changes the way they are distributed in space. Whilst contractile SMCs have a spindle shape and are organised around the circumference of the vessel, synthetic SMCs are smaller and their shape is more polygonal (Rensen, Doevendans et al. 2007); the dimensions change from the order of 100 μm in length and in the order of 5 μm in width for the contractile SMCs (Axel, Kunert et al. 1997) to a diameter of around 50 μm for synthetic SMCs. The lattice dimension has been chosen to be dx = 18.25 μm, consistent with other models found in literature (Boyle, Lennon et al. 2010), and of the same order of magnitude as the diameter of a synthetic SMC, so it is assumed that a single cell can occupy a single lattice point.

A set of tests has been performed in order to evaluate how much the choice of some of the parameters influences the outcome of the model. This is important as measurement of some values *in vivo* and *in vitro* may not directly translate to model parameters due to the influence of discretisation of the model.

The values that have been taken in consideration are:

- *base*, the minimum amount of ECM that has to be present at a lattice point in order to be occupied by a SMC. The effects of a low and high value of this parameter (0.2 and 0.5) will be explored;
- the relative probability of migration and proliferation for a synthetic SMC, expressed by variation of the parameter, *PProb*, between 5 and 60%.

In order to do this, a simple, square, 2D geometry was created, with 50 lattice points per side and an initial number of 4 SMCs, occupying the bottom left corner of the lattice and all of which are in the synthetic phenotype. Those lattice points which had SMCs had an ECM content equal to 1, whereas the rest of the space was composed of empty lattice points, representing the lumen.

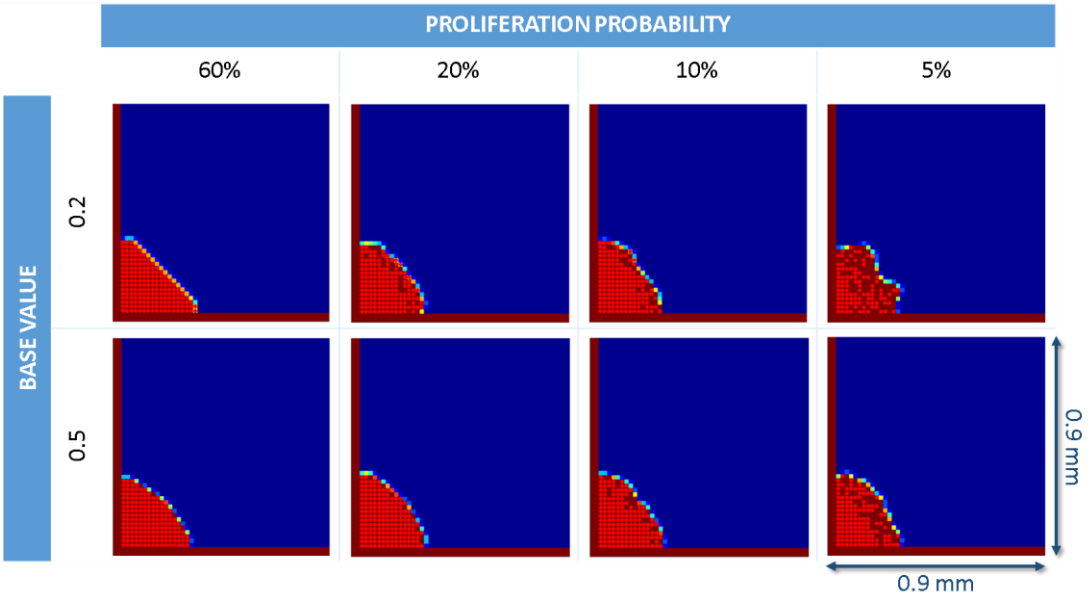

Figure V.3 - Results of the parametric analysis for the probability of proliferation over migration *PProb* (columns) and of the minimum amount of ECM needed for a cell to be able to occupy a lattice point *base* (rows) on a 50x50 lattice points square space (*dx* = 0.01825 mm, see *Table V.1*) .

The results of the parametric analysis are reported in *Figure V.3*. The variation in results demonstrates how influential the choice of these parameters is on the shape of the advancing front. In particular, the result corresponding to *PProb* = 60% and *base* = 0.2 (*Figure V.3*, top left) demonstrates development of the neointima that is

strongly aligned to the lattice geometry, with little evidence of the random direction of migration and proliferation. In general, for a higher *base* value (in this example, 0.5) the result has a predominantly rounded shape, which does not appear to vary much by decreasing the proliferation rate and increasing migration rate. The result on the top right, on the other hand, shows a growth that is more sensitive to the random choices of directions of the algorithm; as the aim of the model is to detect a difference in growth pattern introducing a direction preference given by the mechanical stimulus, the parameters combination of *PProb* = 5% and *base* = 0.2 is chosen.

The list of the chosen parameters for this cellular model is reported in *Table V.1*, together with the references to the literature for the choice of the other parameters.

Table V.1 – Parameters used in the cellular model

Quantity	Parameter	Value
Minimum content of ECM for a SMC to occupy a cell	*base*	0.2
Amount of ECM produced per time-step		0.1 - 0.2[a]
Stress threshold that activates cells	σ_{min}	35 kPA[a,b]
Time-step duration	t	~ 24h
Proliferation/migration probability	*PProb*	5%
Lattice point size	*dx*	0.01825 mm[a,c]

a - (Boyle, Lennon et al. 2010)
b - (Linder-Ganz, Engelberg et al. 2006)
c - (Schwartz, Chu et al. 1996)

Once these parameters had been chosen, an initial, simple, cellular model of ISR was developed, using a geometry similar to that employed for the 2D model described in Chapter 3.

Geometry: to explore the behaviour of the cellular model, a simple model has been developed based on a simplification of the final geometry of the stented vessel

reported by the finite element analysis in Chapter 3, as shown in *Figure V.4*. A vessel with six, evenly-distributed, stent struts was considered using 1/12 symmetry in order to decrease computational time and memory requirements, reducing the dimension of the matrices to be updated at each time-step. The geometric parameters are the same as in the models of the previous Chapters and the dimensions are reported in *Table V.2*.

Table V.2 - Model dimensions

Vessel initial radius	1.4 mm
Stent expansion ratio	1:1.4
Vessel thickness	0.1 mm
Stent radius	0.045 mm

The boundary conditions were set up by excluding any possible cell activity for the lattice points lying outside the symmetry model, outside the vessel and under the strut (lattice points with a yellow cross in *Figure V.4*). The vessel wall region is initially fully occupied by both ECM and SMCs (green circles) which are initially all in a contractile state. An area above the stent strut was chosen to "activate" the cells. These then change into the synthetic phenotype at the start of the simulation (red circles). The colour of the background shows the amount of ECM, in a scale from blue (ECM = 0, lumen) to yellow (ECM = 1, fully formed ECM). For simplicity, a full ECM was also set up for all boundary lattice cells.

The model was run for a varying number of time-steps, to determine the variability of cellular evolution and report the evolution of WSS over each simulation. The results are reported below.

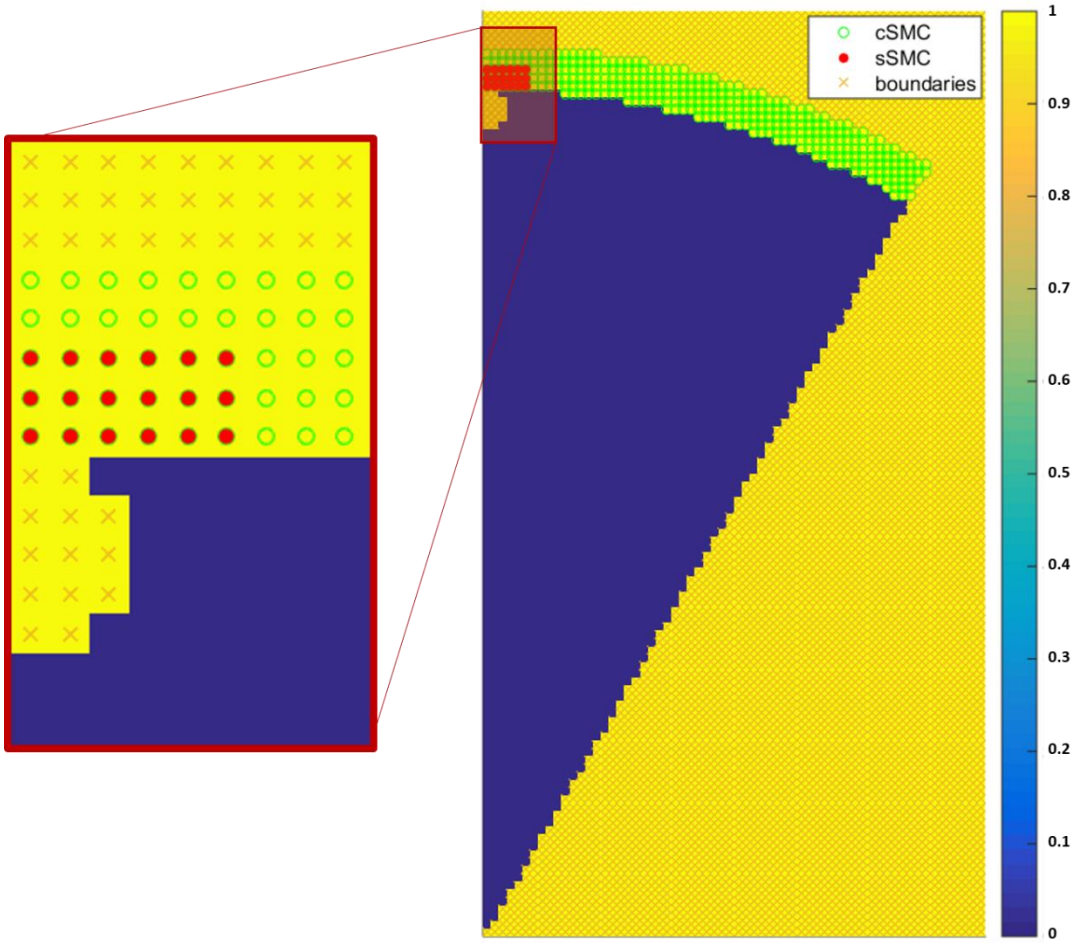

Figure V.4 - Schema of the setup of the model. The lattice points with crosses define the boundaries, the blue area is the lumen; the green circles are cells; if the circle is filled with red, the cell is in its synthetic state. The stent strut is on the top left: it is computed as "boundaries" to stop cells from occupying the corresponding lattice points.

Results

The results reported in *Figure V.5* compare two approaches to perform update of the SMCs at each time-step. On the left (*Figure V.5.a*), the cells are processed within the algorithm in an order determined by their index in the Matlab array. This drives growth towards the centre of the lumen, with a flattened region. On the right (*Figure V.5.b*), the stored cells are processed from the algorithm in a random order, which avoids this bias in evolution of the neointima. The difference in results is noticeable for all the time-steps after the first 10 and shows how processing the cells in their

index order affects the direction of the growth. Therefore, from this point, only results with the second method of selection of the "next cell" to process are shown.

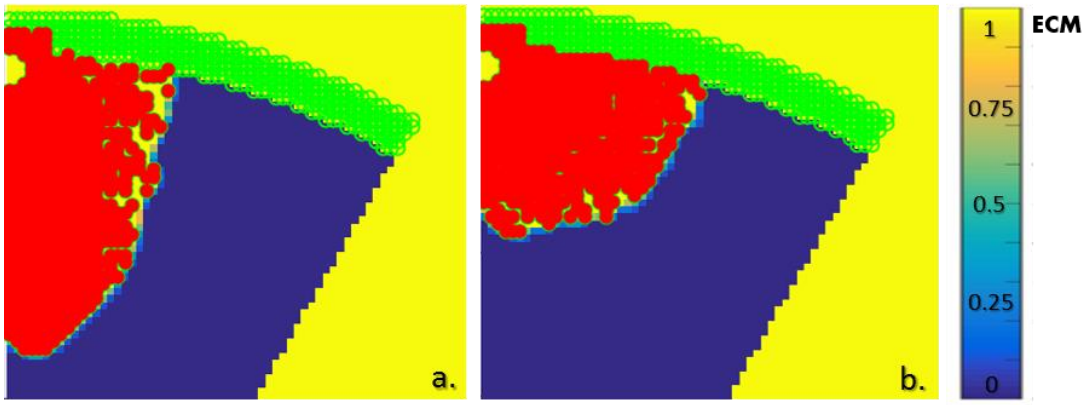

Figure V.5 - Results at 100 time-steps with two different methods to select the "next cell" to process through the algorithm for migration, proliferation, ECM production. a. The cells are processed in the order they appear in the Matlab array. b. The cells are processed in random order.

The results of the simulations are reported in the following figures for various time-points. In particular, *Figure V.6* represents a close-up of the evolution of the model at 10, 25 and 50 days after stenting and for the whole model at 75 and 150 days after stenting. It can be seen that the growth has a rounded shape from its early stages, moving from the corner between the strut and the vessel and eventually surrounding the stent strut. It proceeds with this rounded shape, occupying an increasing area of the lumen, until it reaches the boundaries of the model after around 180 time-points (not shown). For this model, different runs produce very similar results, as resulting neointimal shapes and their progress in time; therefore, only one set of results is presented.

Figure V.7.a shows the change in neointimal area in the first 200 time-steps after stenting, while *Figure V.7.b* shows the evolution of wall shear stress. The plots show how the increase of neointimal area has a positive gradient up to 180 time-steps, where it changes to a negative one: this corresponds to the moment the neointima reaches the boundary of the model. As expected, the wall shear stress

increases with the evolution of neointima, but the increase becomes steeper after 150 days. To place these results in context, WSS = 1.5 Pa is considered to be the physiological value for a vessel of this radius prior to stenting, as explained in Chapter 2: this value is reached in this simulation after 157 days.

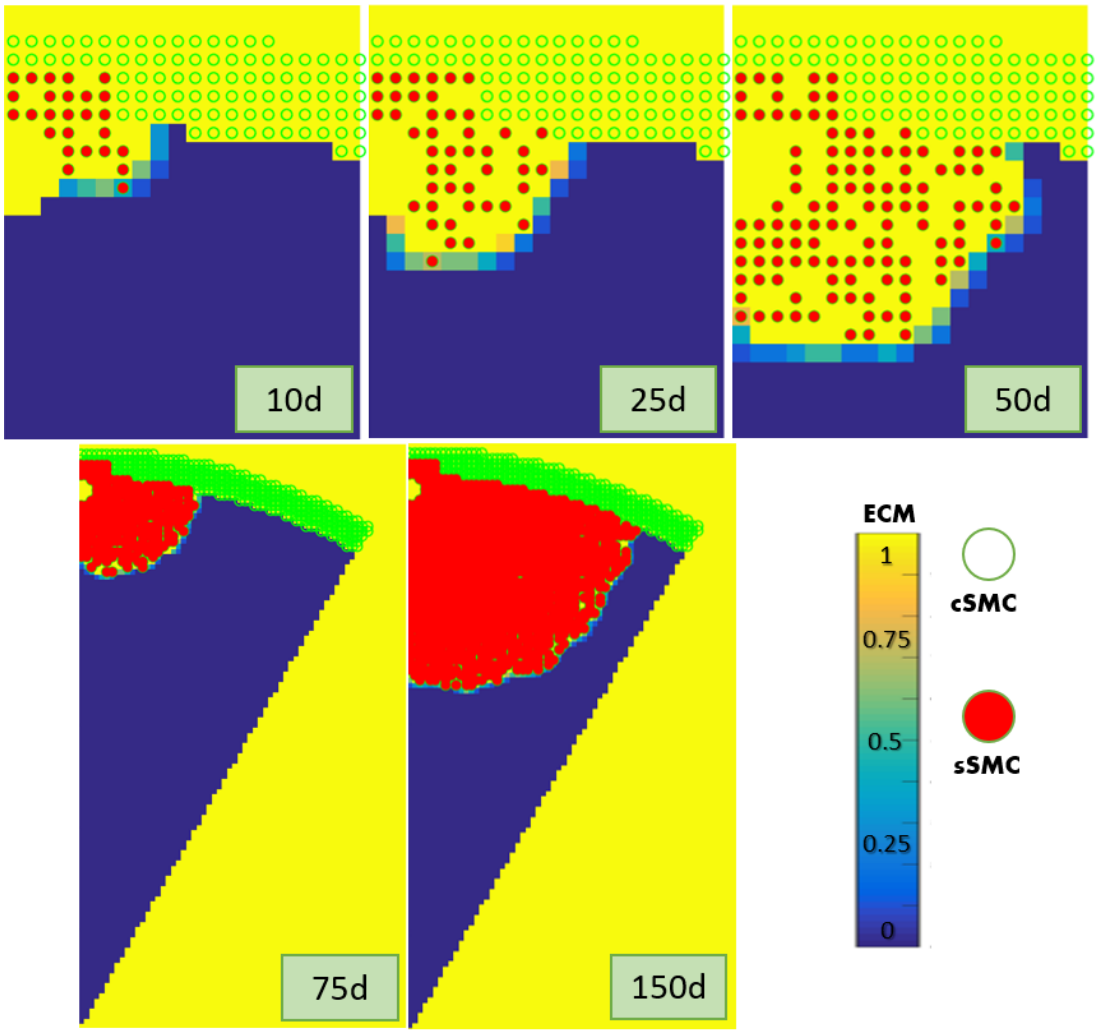

Figure V.6 - Evolution in time of the model at the following time-steps: 10 days, 25 days, 50 days, 75 days and 150 days.

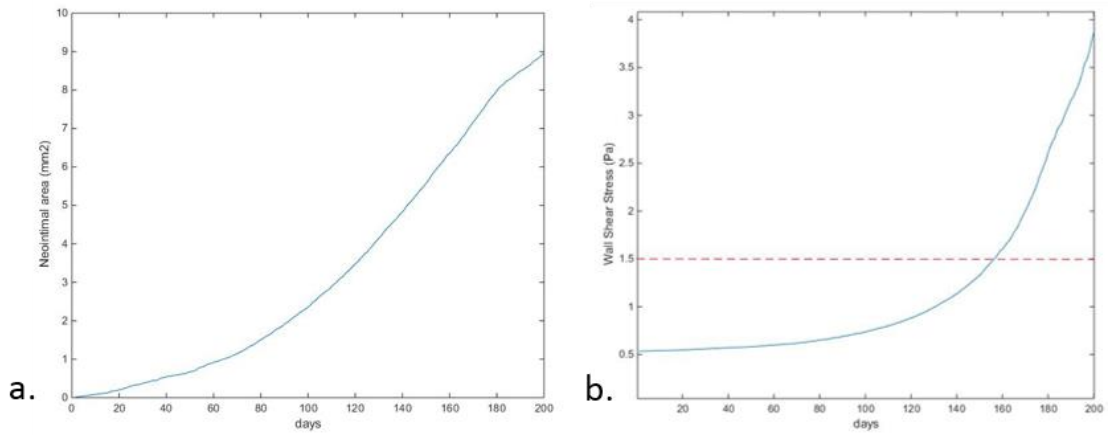

Figure V.7 - Evolution of the neointimal area (a) and of wall shear stress (b) at 200 days after stenting, the red dashed line indicates the pre-stenting WSS value of 1.5 Pa.

Discussion

The results of the cellular model have been reported in the form of images of the neointimal tissue region at particular time-points and plots of the variation in neointimal area and wall shear stress over time.

Comparison of these results with the development of ISR in a porcine *in vivo* model (Morlacchi, Keller et al. 2011) is summarised below. In this study histological sections were analysed from a porcine model of ISR processed at a different time-points, specifically 6 hours and 4, 7, 14, 21 and 28 days post stenting (*Figure V.8*). The porcine implantation work uses the methodology described by Malik *et al*. (Malik, Gunn et al. 1998). As introduced in Chapter 1, the evolution of human ISR is characterised by four phases, *thrombosis*, *inflammation*, *proliferation* and *remodelling*. This description is also valid for porcine ISR: various studies have examined neointimal formation in porcine coronary models of ISR, obtained by deploying an oversized stent (Miller, Karim et al. 1996, Christen, Verin et al. 2001) and reporting similar behaviour, with thrombotic and inflammatory reactions observed in the early stage post-stenting (4-8 days), a predominance of SMCs and proliferation within the neointima alone by day 14 and a distinct accumulation of

neointimal collagen at 14-28 days post-stenting, in particular in proximity of the stent strut locations of the neointima. This evolution of neointima over time is also visible in *Figure V.8* below: the presence of significant neointimal thickness is only visible from day 14 onwards. However, histology images at day 7 show that the initiation of neointimal growth occurs in the neighbourhood of the stent struts (*Figure V.9*), tending to reduce the acute angle created between the strut and the vessel. These images highlight the first limitation of the cellular model presented here as the evolution of the distribution of neointima differs significantly from these images, evolving to produce "lumps" of neointima around each stent strut. This difference follows the same trend as the analysis time proceeds. A similar response has been observed as a limitation of ISR models in other studies (Boyle, Lennon et al. 2010, Zahedmanesh, Van Oosterwyck et al. 2012).

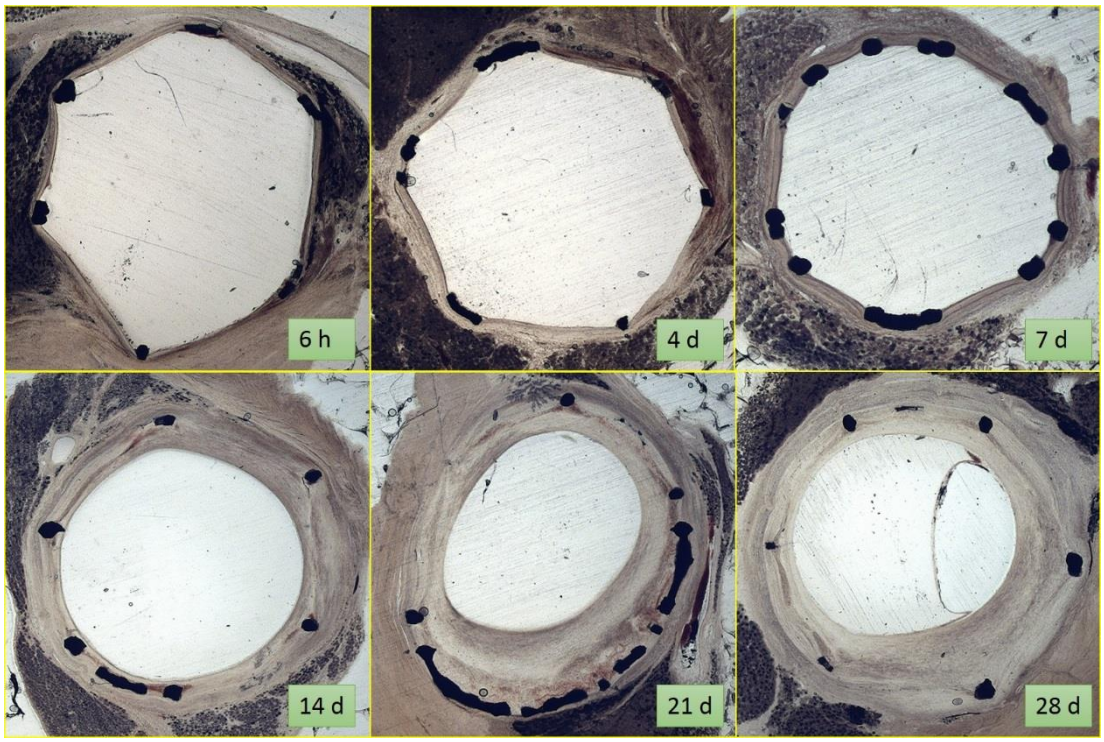

Figure V.8 - ISR at different time-points in the right coronary artery of porcine models (courtesy of Julian Gunn).

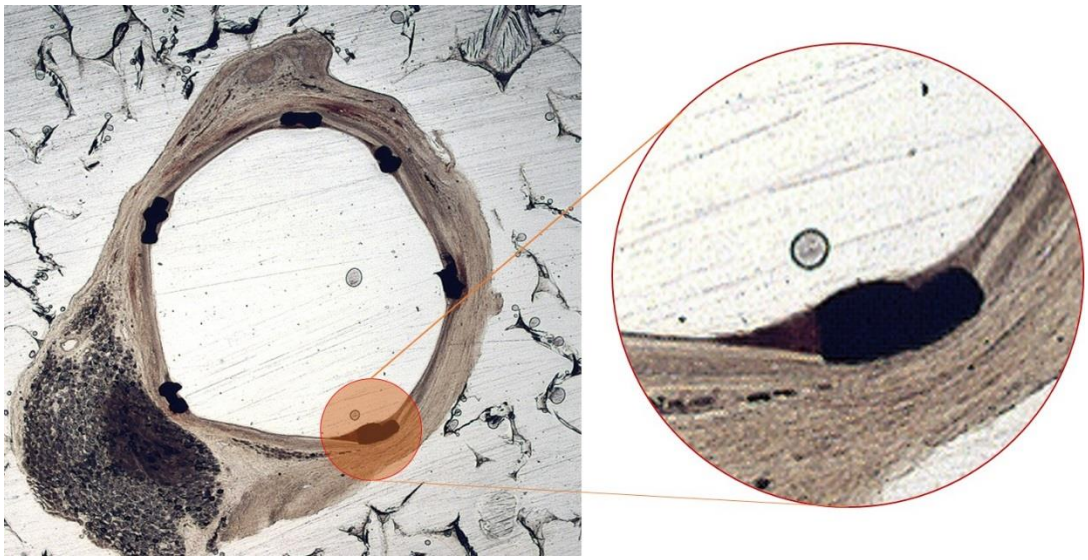

Figure V.9 - 1 week after stenting the right coronary artery of a porcine model, detail (courtesy of Julian Gunn).

Previous studies have analysed ISR development over time from porcine data, measured as neointimal thickness at the stent strut location for different levels of injury, to be used as a reference for the results of a cellular ISR model (Tahir, Hoekstra et al. 2011, Amatruda, Bona Casas et al. 2014). *Figure V.10.b* reports these neointimal thickness measures. The Gunn Injury Score is an indicator of the degree of injury imposed on the vessel (Gunn, Arnold et al. 2002), while *Figure V.10.a* reports the thickness of the growth at the strut location for the model described in this Chapter. The plots for the *in vivo* model all present a linear relationship for the first period, as observed in this cellular model, but, in common with the other plots shown for this model, the timescales are noticeably different.

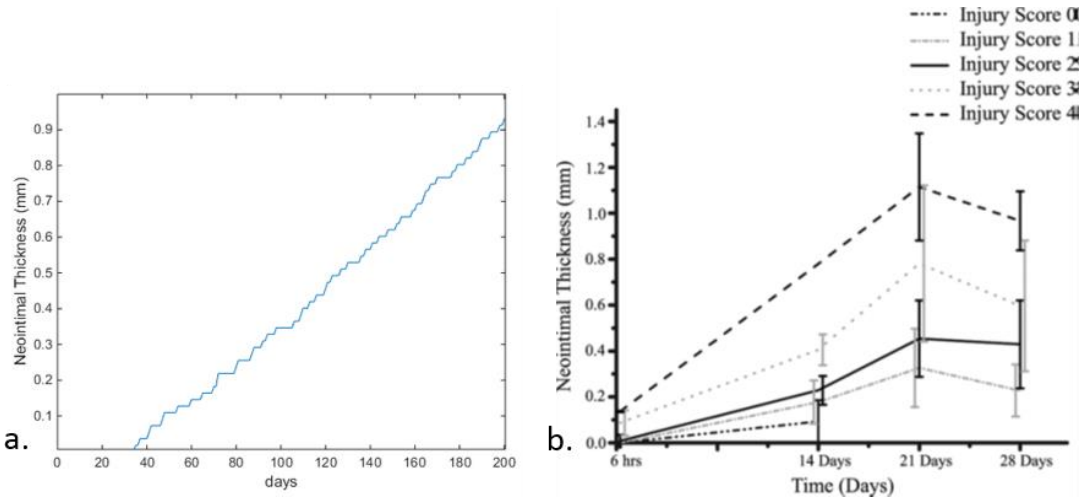

Figure V.10 – a. Evolution of the neointimal thickness for the cellular model b. Evolution of neointimal area in porcine models of ISR obtained by Tahir *et al.*, reproduced with permission from (Amatruda, Bona Casas et al. 2014).

Using the same assumptions as for Chapter 2 the model predicts a value of just over 0.5 Pa for a stent expansion ratio of 1.4:1 with a vessel radius of 1.4 mm. For this model, the wall shear stress increases up to the "pre-stenting" value of 1.5 Pa at only around 160 days after stenting, as indicated from the red dashed line in *Figure V.11*.

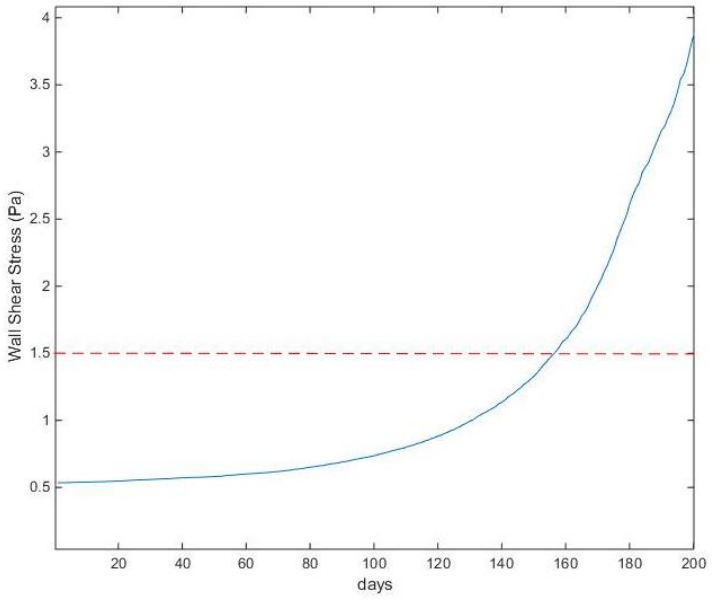

Figure V.11 - Evolution of WSS in the cellular model up to 200 days following stent expansion, where the red dashed line indicates the pre-stenting WSS value of 1.5 Pa.

The ISR modelling presented by Tahir *et al.*, introduced in Chapter 2 (Tahir, Hoekstra et al. 2011), predicts the evolution in neointimal area reported in *Figure V.12.b*, compared with the results of the cellular model developed here (*Figure V.12.a*). Whilst the timescale of neointimal growth is quite different, with 1 mm^2 of neointima already present after around 14 days for Tahir's model and more at 30 days for the current model, the shape of the curve follows a similar trend. As described previously, in this model the change in response at around 180 days occurs when neointimal growth starting from two neighbouring stent struts develops along the circumferential direction to reach the symmetry boundary.

The timescale of the model introduced in this Chapter is not accurately defined yet, as it depends on several factors such as the definition of time compared to the algorithm time, the effect of some parameters such as *PProb* and other implementation choices. For this reason, it is hard to define the length in time of a time-step; this is explored in more detail in Chapter VI (pag.188).

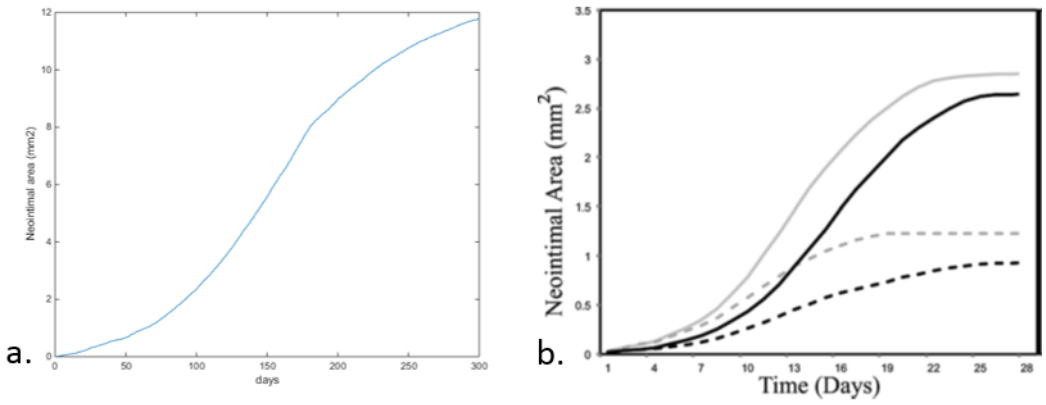

Figure V.12 – a. Evolution of the neointimal area for the cellular model of the present study b. Evolution of neointimal area for the cellular model of Tahir *et al.* for two deployment depths (90 µm in black, 130 µm in grey) and two re-endothelialisation rates (faster for dashed lines, slower for solid line), reproduced with permission from (Amatruda, Bona Casas et al. 2014).

The present cellular model represents a first attempt to represent the evolution of ISR through very simple rules: it represents the starting phase of ISR, as it only considers

the stress underneath the stress struts and it does not update the stress stimulus in the neointima. The next section of this Chapter proposes a refinement of the cellular model to represent the variation in stress stimulus over time as a result of the change in geometry of the neointima, to allow better understanding of the evolution in the neointimal growth at later time-points.

5.2 DEVELOPMENT OF A FRAMEWORK WITH CELLULAR AND CONTINUUM MODELS OF ISR

The previous section presented a 2D model of cellular growth of a section of a stented artery: this was idealised in many aspects, some of which are addressed in this section of the Chapter, whilst others will need to be addressed in future work. These simplifications are as follows: the post-expansion geometry of the vessel is still represented as a circle; the distribution of the stress in the vessel was chosen with reference to FEM models but was not directly exported from these and, in particular, cell growth is based simply on their internal rules and not on the stress, or change of stress, in the new vessel geometry, in particular of the neointima, as this changes consistently with the cellular growth itself.

This section proposes a method of driving cellular growth on the basis of a mechanical stimulus obtained from a continuum model that can be updated during cellular evolution.

Methods

The cellular model (CM) presented in the first part of this Chapter is a preliminary attempt to describe the neointimal growth in the initial post-stenting phase without

including the influence of evolution of stress with the change of geometry on cell behaviour.

It has been shown that the stresses acting on groups of cells can influence the direction of cell migration, which tends to follow the local orientation of maximal principal stress (Tambe, Hardin et al. 2011). To explore these effects in the context of ISR, this section describes refinement of the CM aimed at capturing the contribution of stresses within the neointima to the evolution of cellular growth, by coupling the CM to a finite element model which includes the geometry of the vessel wall and computes the evolution of the stress direction within the neointima during cell growth. For the remainder of this Chapter, this model is referred to as the Coupled Cellular Model (CCM).

The following sections describe the CCM workflow, which is also represented in *Figure V.13*, dividing it between an initial set-up, CM Matlab model and ANSYS finite element model.

Workflow: the workflow in *Figure V.13* defines the nature of the coupling between the two models, the frequency at which this takes place, and under what criteria. The workflow is controlled by Matlab, which uses batch files to load ANSYS simulations and waits for ANSYS to complete before moving to the next set of commands; the exchange of information between the two models is achieved using structured text files.

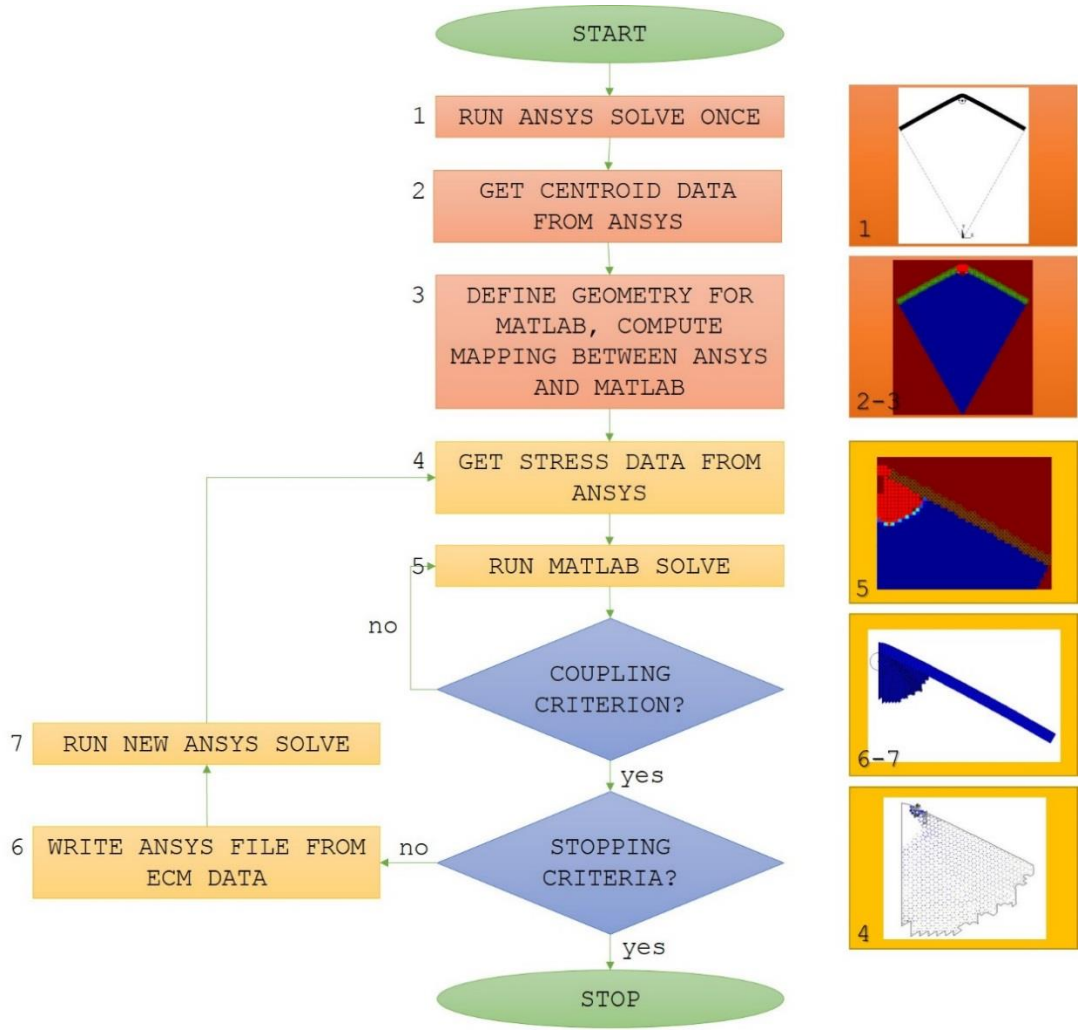

Figure V.13 – Workflow scheme, with an initial phase to set up the problem (orange blocks) and a loop phase with the coupling iterations (yellow blocks).

INITIAL STEPS: PROBLEM SET-UP. A first run of the two models is necessary to set up the coupling, to establish the correspondence between the nodes of the finite element model and the lattice points of the CM. During this first coupling, ANSYS performs the stent deployment of a 2D model of a cross-section of a vessel, similar to that described in the previous Chapters, loaded with physiological pressure (100 mmHg) to obtain the final position of the stent strut and the vessel (step 1). This model is described in further detail in the section "*Ansys model*".

The final *x* and *y* positions of the nodes are then imported into Matlab (step 2) to create a mapping between the ANSYS nodes and the *x* and *y* coordinates of the

CM lattice points. In this way, the lattice area is divided into "vessel wall", "lumen", "stent strut" and "boundaries". The points corresponding to the wall were filled with 100% content of ECM and with contractile SMCs (step 3). At this first iteration the finite element model also provides the distribution of compressive stress (S3) in the vessel wall; a threshold was chosen according to values already used in literature, i.e., a compressive stress of 35 kPa (Linder-Ganz, Engelberg et al. 2006, Boyle, Lennon et al. 2010). In locations where the compressive stress is higher than this threshold, corresponding to the "stressed area", a reaction from the cells is assumed and their state is changed to synthetic. The cellular model is set-up and its first run is started. This corresponds to step 4 for the first run of the flowchart; the information about stressed cells is passed on the next phases though the cellular model, and in step 4 of the following iterations the stress data passed from ANSYS to Matlab includes the first principal stress direction within the neointima generated by the cyclic changes in blood pressure acting on the vessel wall.

Matlab cellular model (CM): The rules of the CM are similar to those described in the previous section, in particular for the first run, with the difference that the geometry is imported directly from the ANSYS model as well as the information about which lattice points correspond to the section of the wall where the stress threshold is exceeded. From the second run, new information is provided to the CM from the finite element model to describe the direction of the principal stress in the neointima that grew during the previous iteration, as represented in *Figure V.14*. This information is imported into Matlab in the form of stress in *x, y* and *xy* direction and converted to the direction of the first principal stress (step 4 of the flowchart in *Figure V.13*). This direction is then used to inform the preferential direction of

growth for cells that will either migrate or proliferate to a neighbouring lattice point, as illustrated in *Figure V.16*.

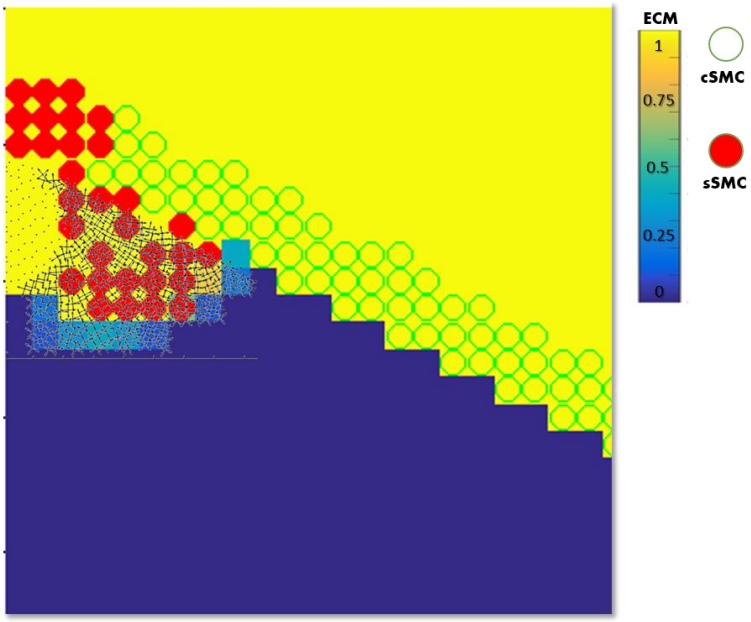

Figure V.14 – Representation of the neointima generated through the cellular model in Matlab, with the stress distribution obtained through the simulation with ANSYS.

The matrix that stores the directional information obtained through the ANSYS simulation for each lattice point is called *THETA* and contains the angle, relative to the reference system of the CM, of the first principal stress for each node of the ANSYS model. It has the same dimension as the other matrices used to describe the components of the CM, such as *SMC* and *ECM*; as there are multiple nodes that correspond to the location of one lattice point, the angle of the first principal stress is averaged over all nodes within a single lattice square.

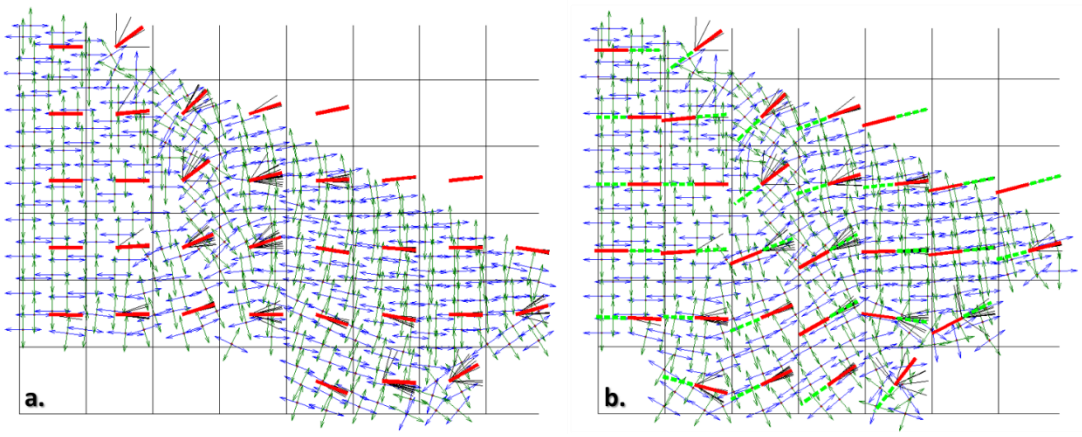

Figure V.15 – Correspondence between lattice points, node locations and stress information. a. Theta angles before the random choice of direction. The grid represents the lattice points of the cellular model: there are many dots, the nodes of the finite element, for each of them. The arrows represent the angles of the principal stresses; the first principal stress angle is reported at the centre of the lattice point (black lines) and their average is calculated (red line). b. Theta angles after the random choice of the direction.

This process is shown in *Figure V.15*, the grid represents the lattice squares of the CM, while the arrows show the direction of the first (blue) and second (green) principal stress of each node of the FEM model. The average direction for each lattice square is calculated and the resulting angle *theta*, represented by a red line, is reported at the centre of each lattice square (black lines) and stored in the *THETA* matrix (*Figure V.15.a*). It is assumed that cells can move in either of the two directions defined by the first principal stress (*theta* angle and *theta+180°*). A detailed description of the implementation options considered for the application of preferential direction to cellular growth is given at the end of this methods section. *Figure V.15.b* shows the case where cells are randomly assigned a value of either, *theta* or *theta+180°*: the solid red line shows the assigned direction and the green dashed line represents the opposite direction.

Following the definition of angle at each lattice point, all the information derived from the last ANSYS solution has been processed and the next iteration of the CM takes place.

Within the CM, synthetic SMCs are first identified. The algorithm scans through each of these, identifying cells which can migrate, proliferate and deposit ECM. This happens in a similar way to that described in the first section of this Chapter, but with extra regulation based on the direction of the stress in the neointimal tissue. This happens for each synthetic SMC; the process is then repeated until one of the exit criteria is met. *Figure V.16* represents, schematically, the process which occurs at each iteration for every cell, for a cell in the neointima.

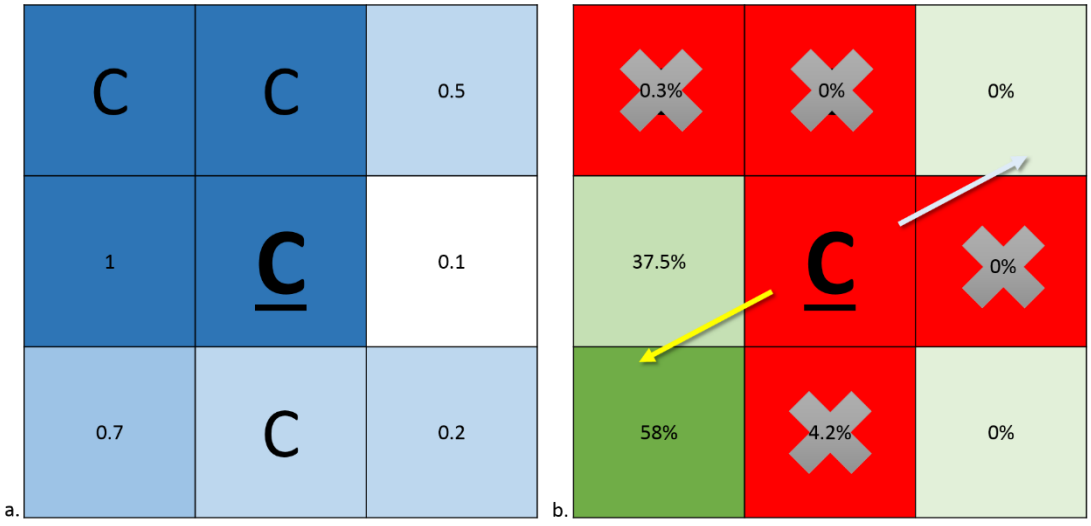

Figure V.16 – Example of the method to select the next lattice point where a cell can migrate or proliferate. a. Representation of the content (SMCs and ECM) of the lattice points neighbouring the SMC C. b. Representation of the probabilities of moving in one of the eligible neighbouring points. The arrows represent the direction of the principal stress in the neointima.

The algorithm determines the lattice points where a migrating cell can move or where a proliferating cell can replicate. The cell under consideration is represented by the symbol C, and the grids represent its neighbourhood. For each cell the algorithm scans the neighbourhood conditions (*Figure V.16.a*) to check if there is any lattice points where a cell could migrate or proliferate. The C in a lattice points means that it is occupied by a SMC, while the number represents the content of ECM. In this example an ECM threshold of 0.2 is used, meaning that 4 lattice points can be occupied, as these do not contain an SMC and there is enough ECM content

(green lattice points in *Figure V.16.b*). If the number of eligible lattice points is zero, the algorithm skips the next step of the process and simply produces new ECM in its neighbourhood, as explained in the first section of this Chapter and represented in *Figure V.2*. If any eligible position is found, the algorithm determines whether the synthetic SMC is in a proliferative or migrating state, according to the respective probabilities, as described previously. The grid on the right represents this phase of the iteration: the cell is unable to migrate or proliferate to any of the crossed lattice points, because of the presence of another SMC or insufficient ECM content. If the cell proliferates, the new cell will occupy any of the green lattice points, chosen randomly. If the cell migrates, the algorithm uses the principal stress direction in the neointima corresponding to the lattice point of the current SMC, stored in the *THETA* matrix: the arrows represent the direction of the principal stress in the neointima. This is the case for most implementations of the model; however, in some cases it has been chosen to make also the proliferation dependent on *theta*.

Cell movement is determined by a probability distribution determined by the principal stress direction. *Figure V.17* shows the probability distribution for a *theta* value of 210°; the probability distribution is centred on this angle using a the function given in *Equation 1* (dashed red line) and then discretised to each lattice position to provide probability values which sum to 100% (blue line, green dots).

$$P = \begin{cases} 0, & x - \vartheta < -\frac{\pi}{2} \\ \left(\frac{1}{2}(\cos(x-\vartheta)+1)\right)^2, & -\frac{\pi}{2} < x - \vartheta \leq \frac{\pi}{2} \\ 0, & x - \vartheta > \frac{\pi}{2} \end{cases} \qquad [1]$$

The resulting probability values for this example are represented using numbers on the grid of *Figure V.16.b*.

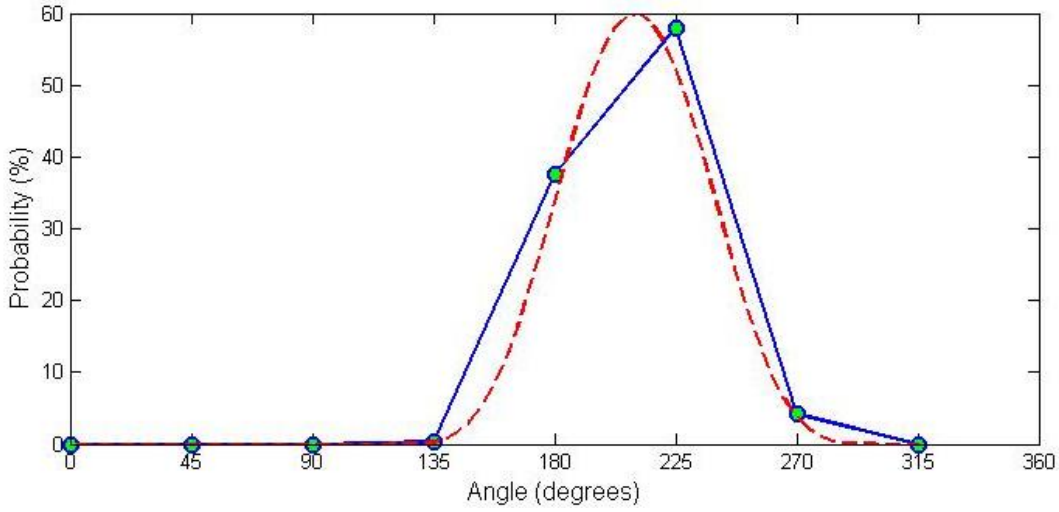

Figure V.17 – Example of probability distribution of the new lattice point for a migrating cell based on the *theta* value: in this case, *theta* = 210° (red dashed line) and the probability values obtained are, starting from the lattice point on the right (position 0°) in anticlockwise direction: 0, 0, 0, 0.3, 37.5, 58, 4.2, 0.

A random process of selection subsequently picks one of the lattice points accordingly to their probability: if the chosen location is already occupied by another cell, like the lattice points with the 0.3% and 4.2% probability in this example, the SMC will not be able to migrate for the current iteration. When a cell migrates, if the *THETA* value of the new lattice point is not already specified, for instance in cases where the ECM content of that section has been created after the last ANSYS run, the new lattice point takes the same value of *THETA*. At the end of this phase, new ECM is produced.

The algorithm then moves to the next cell of the stressed SMCs list, until the list has been completed. In that case, the algorithm checks whether any of the exit criteria to solve the ANSYS model are met: if not, it increases the time count and re-calculates the list of stressed SMCs to perform a new iteration of the CM.

The criteria to exit the CM iterations have been chosen so that the coupling with the ANSYS model happens when neointimal growth is sufficient to change the stresses in the neointima: through time (number of days) and through amount of

growth (number of cells). Once one of the coupling criterions is met, a new mapping is set up, this time between the neointima lattice points and the nodes of a pre-existing mask of a mesh of the neointimal area in ANSYS; this is used to define the geometry of the ANSYS model, as described in the next section.

ANSYS model: for the continuum model, ANSYS Mechanical APDL version 14.0 (ANSYS Inc.) is used. The geometry of the vessel and of the stent strut, the amount of deployment and the material properties of the model are the same as described in Chapter 3 and are reported in *Table V.1*. A set-up iteration is performed at the very beginning of the process (step 1 of the flowchart in *Figure V.13*), where the stent is expanded in the vessel, similar to the symmetric models in Chapter 3 (*Figure V.18.a*). All the iterations of the model are based on the final result of the set-up iteration. In order to establish the spatial relationship between the ANSYS model and the CM, in a second iteration the lumen area that might be occupied by neointima is meshed based on the expanded geometry (*Figure V.18.b*); the upper part of the neointima mesh is defined using the nodal coordinates of the deformed inner lumen of the vessel, but the mesh density in the neointima is independent of the mesh density on the vessel wall. A bonded contact condition is defined between the nodes on the neointima and the nodes on the vessel lumen to connect the meshes. The neointima elements are deactivated so they do not influence the stress results on the vessel.

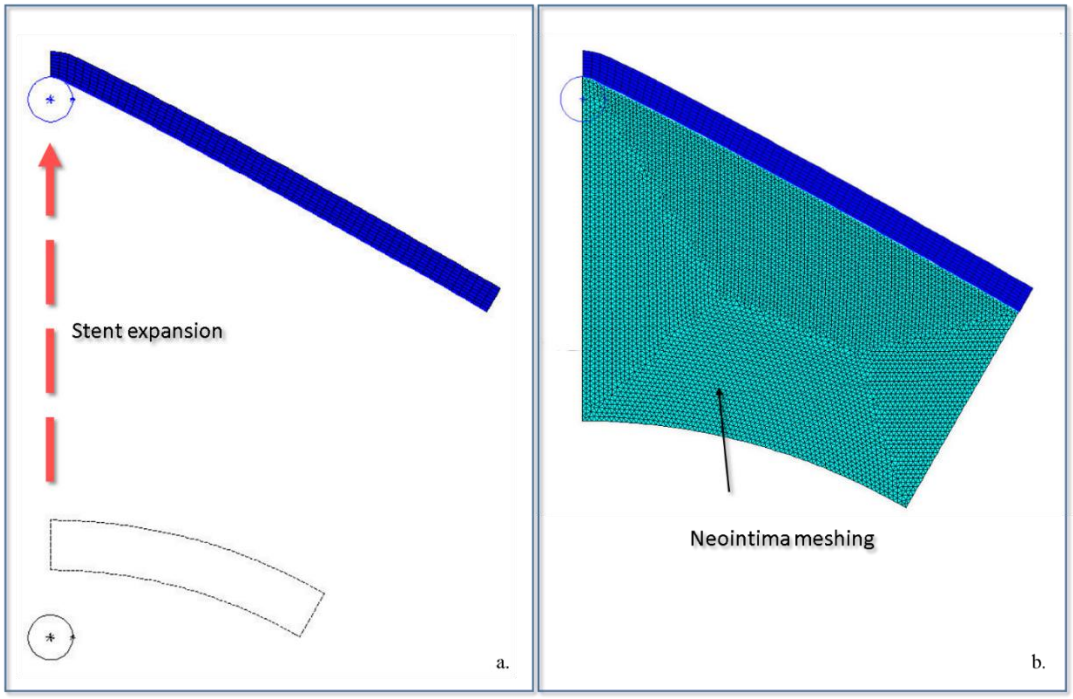

Figure V.18 – Representation of the two iterations which correspond to the two initial steps of the workflow. a. Creation of the initial 2d symmetric geometry and stent expansion. b. Meshing of the part of the lumen that is likely to be occupied by neointima in the following iterations on the basis of the expanded geometry, with subsequent de-activation of the corresponding elements.

At the end of these two iterations, represented in *Figure V.18* as "stent expansion" and "neointima meshing", information about the type and location of all the nodes is reported in tables that are then read in Matlab, distinguishing for instance between stent strut location, vessel nodes, stressed vessel nodes (the ones where the 3rd Principal stress, which corresponds to the compressive stress, is above 35 kPa); lattice points above the vessel wall and the boundary conditions are turned off and do not participate in the cellular iterations. This corresponds to the steps 2 and 3 of the flowchart (*Figure V.13*).

The following table reviews the geometry and the material properties for the first iteration of the simulations.

Table V.3 - Parameters for the ANSYS model

Vessel thickness	0.1 mm
Vessel radius (pre-pressure)	1 mm
Vessel radius (100 mmHg)	1.4 mm
Strut radius	4.5e-2 mm
Vessel material model (MPa)	$U = 0.04 \cdot (I_1 - 3) + 0.003 \cdot (I_2 - 3)^2 + 0.085 \cdot (I_2 - 3)^3$
Displacement ratio	1:1.4
Neointima material model	*E = 0.1 MPa; v = 0.49*

During the second iteration, the nodes of the ANSYS model which correspond to regions of the CM which are occupied by neointima are identified and these elements are activated. The neointima is assumed to behave as a linear elastic material. The material properties of the neointima are not as well-known as those of the coronary artery wall, and as the main feature that is captured from the simulation is the direction of the first principal stress, this is assumed to not change significantly for any isotropic material: so a simple model has been chosen, especially considering that this material will experience only small deformations due to the cyclic blood pressure change. As these elements are initially turned off, they do not contribute to the stress state of the ANSYS model until activated from the update of the CM.

Once these two iterations are completed and the nodes data have been sent to Matlab (step 1 and 2 of the flowchart in *Figure V.13*), the CM is created (step 3), the stressed SMCs are turned into synthetic (step 4) and the first cellular iteration starts (step 5). From this moment on, all the following ANSYS iterations are similar: neointimal growth is simulated by the CM, which changes the geometry of the stented vessel model. Once one of the coupling criteria of the workflow is met, the CM performs a new mapping of the neointimal area (*Figure V.19.a* and *b*), updating the correspondence between lattice points and elements (*Figure V.19.c*); the growth

information is therefore passed from the CM to ANSYS in form of a list of elements of this mesh (step 7 of the flowchart in *Figure V.13*). These are the new neointimal elements, and they are activated while the vessel is at its diastolic pressure (*Figure V.19.d*).

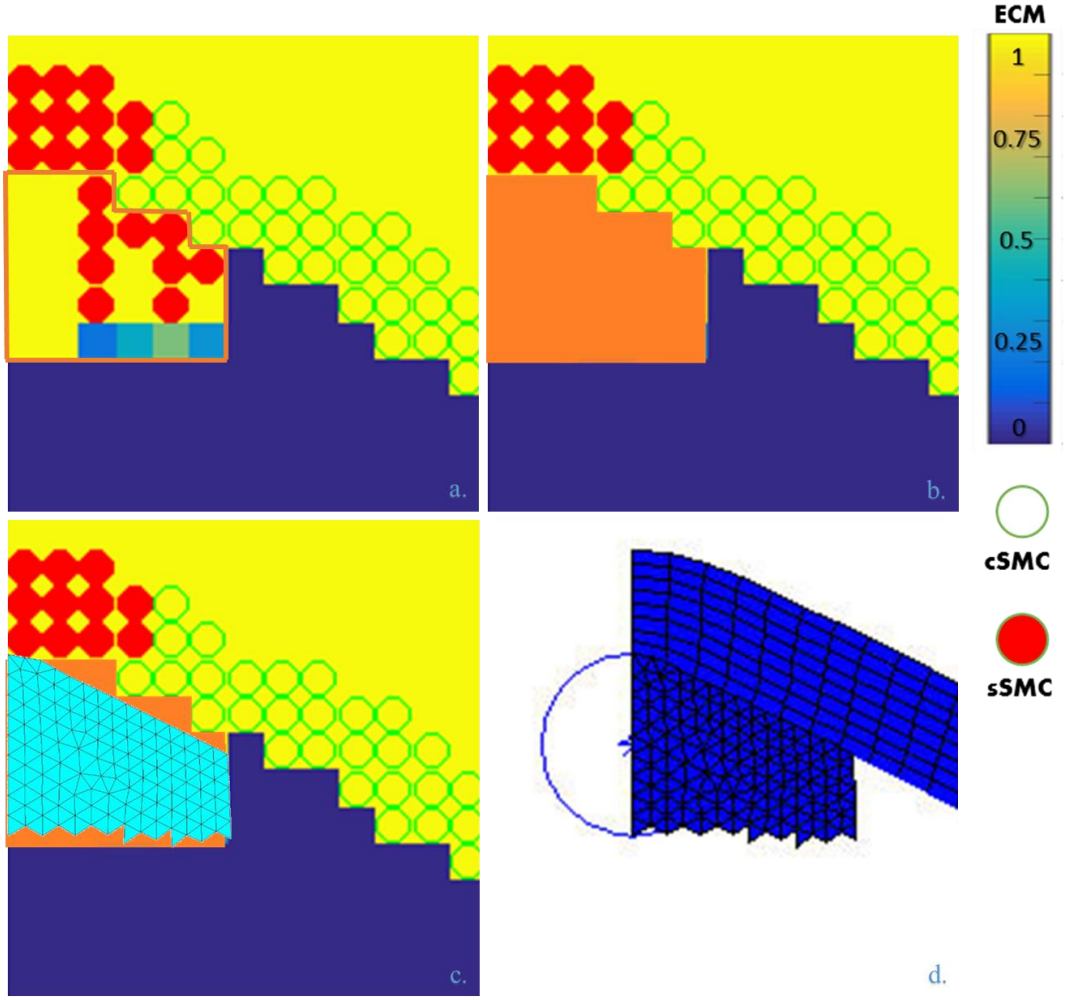

Figure V.19 – Representation of the process selection of the new nodes to be activated into the ANSYS model when a coupling criterion is met. a. and b. show the selection of lattice points that contain ECM (to make the process easier, these include the strut location). c. The algorithm searches through matching locations between cellular model and FEM to find what nodes correspond to the selected lattice points. d. Activation of the selected nodes in the finite element model.

The unstressed geometry of the neointima is defined at the diastolic pressure, *Pdias*; the difference between diastolic and systolic pressure, *dP = Psys-Pdias*, is then applied in the ANSYS model as an additional load on the new lumen defined by the vessel wall and the neointima. When the ANSYS solution is obtained at *Psys*, the

ANSYS iteration is completed and information about the stress state of the neointimal area is passed back to the CM. This approach is based on the hypothesis that the neointima is laid down in a "stress-free state" at the diastolic pressure. Regions of the vessel wall without a neointima experience the full systolic pressure and the neointima is loaded with the difference between diastolic and systolic pressure as shown in *Figure V.20*. This corresponds to step 7 of the flowchart in *Figure V.13*.

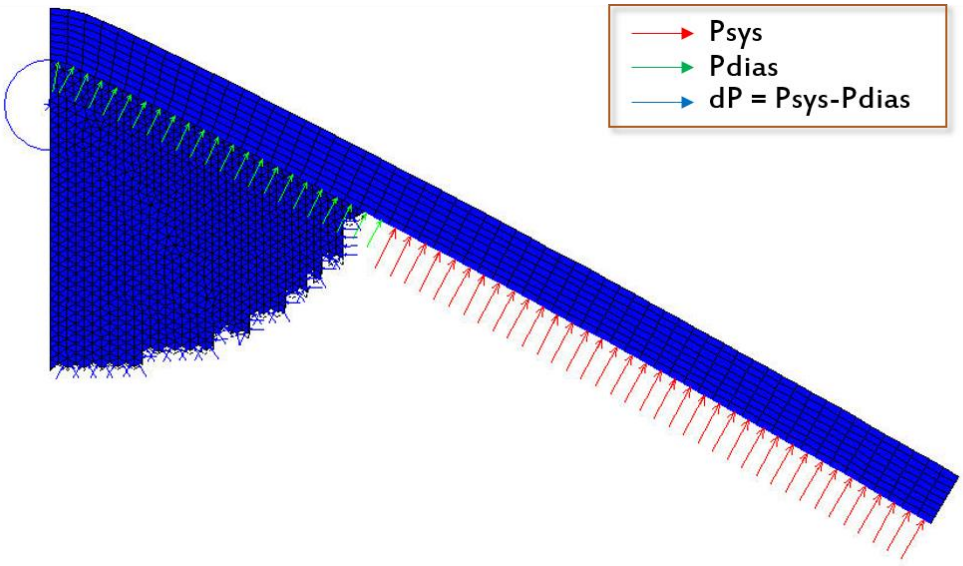

Figure V.20 - Pressure distribution during systole after neointima formation.

At the end of the simulation, the new set of data that is passed from ANSYS to the CM is the stress in *x*, *y* and *xy* direction, as previously explained, in order to obtain the direction of the principal stress in the neointima (step 4 of the flowchart in *Figure V.13*).

EXIT FROM THE WORKFLOW

The whole workflow is terminated ("stop" in the flowchart in *Figure V.13*) when it encounters either of these two conditions:

- When the value of WSS, which is calculated at the end of each CM iteration, exceeds the value of 1.6, corresponding to what the initial value would be before stent expansion, as calculated in Chapter 2. The rationale behind this choice is the assumption that the neointimal growth could stop when the physiological value of WSS is restored.
- When the total time of the workflow, calculated as the sum of the total number of time-steps of all the iterations, reaches a defined threshold (i.e. 1000). This allows the simulation to stop in case the neointimal growth is not evolving for some reason, i.e. too strict direction conditions or mistakes in the implementation.

Implementation of cellular direction

The main aim of this work is to test the hypothesis that the structural stress in the growing neointima might affect the pattern of the growth itself. The basic idea behind the proposed workflow is to capture the evolution of the stress during the ISR process, simulated through a 2D cellular model, and using such information to regulate the neointimal growth: this is achieved by performing frequent 2D finite element simulations with the most updated geometry of stented vessel and neointima.

The hypothesis taken into consideration is that the major stress affecting the neointima is the pulsatile pressure in the vessel due to the blood flow, so this has been captured in terms of first principal stress direction and imported into the CM as indication for the growth direction. As this is a novel approach, a number of tests have been undertaken to evaluate how the cellular growth predicted by the CCM is influenced by the implementation of cellular direction within the model. These approaches are summarised in *Table V.4* and described in the following section.

Table V.4 - Methods to implement cellular direction

Assignment of *theta*	**Process controlled by *theta***
Initial tests	
No Theta	N/A
Arbitrary Theta	Cell Migration only
Single principal direction	Cell Migration only
CCM setup tests with Dual Principal Direction	
Cellular Randomisation	Cell Migration only
Cellular Randomisation	Cell Migration and Proliferation
Total Randomisation	Cell Migration only
Total Randomisation	Cell Migration and Proliferation

The full model with the complete sequence of procedures (import set of data, process it and transform it into information for the next iterations) includes a number of steps that increase the randomness of the CM. In order to investigate the influence of the stress in the neointima for the whole CCM, some of these steps are introduced gradually, with the aim to have a better understanding of which factors significantly influence the results.

No Theta and *Arbitrary Theta* – The *No Theta* model is similar to what has been introduced in the previous section but with the updated geometry. The *Arbitrary Theta* model applies a fixed value of *theta* to all lattice cells of the neointima without an update obtained from the ANSYS model. The set of parameters is the same, so the difference in results is only based on the influence of *theta*.

Single principal direction – As a first attempt to introduce the *theta* values from the ANSYS model into the CM, any randomisation of stress direction was switched off. In this case the cells will migrate only following the angle assigned by the *THETA* matrix, as represented in *Figure V.15.a*, with no possibility of moving in the opposite direction (*theta+180°*) along the principal stress direction.

Dual principal direction – Under the hypothesis considered, which states that the cells follow the direction of the maximum principle stress, cell migration in the directions *theta* and *theta+180°* is equally likely. Two methods to assign the direction randomly have been implemented: with **CellRand** the direction of *theta* is randomly chosen lattice point by lattice point at the beginning of each CM to be either *theta* or *theta+180°*, as shown in *Figure V.15.b*; with **TotalRand**, at the beginning of each time iteration of the CM, the algorithm chooses randomly between the use of the matrix *THETA* or *THETA+180°* applied to every lattice point.

Influence of theta on migration/proliferation – For most tests (**Normal**) the effect of *theta* is imparted only to the SMCs that are in their migrating state. As this method might create a situation where the effect of *theta* is dependent on respective proliferation and migration rates, comparative simulations were run where the effect of *theta* is also imparted on the SMCs that are in their proliferating state (***theta*P**). As for random proliferation, if the identified lattice point is already occupied or does not have enough ECM, the proliferation does not happen.

Influence of other CCM parameters

As for the study of the CM in the first section of this Chapter, some other parameter tests were been performed, as follows.

Influence of base and PProb parameters – Tests varying the values of *base* (0.2 and 0.5) and *PProb* (5% and 10%) were undertaken to check the assumptions made during their choice by comparing the result with the outcomes observed using the CM only.

Variable PProb – An additional test was set up to explore potential variability in the SMC response based on changes in the local environment of the cell. In this case a new condition changes the probability of proliferation for a specific SMC during one time-step in case it is surrounded by ECM: $PProb = 45*(x/8)^5 + 5$, where x is the number of eligible neighbouring lattice points, not occupied by another SMC and with enough ECM (*Figure V.21*). This maintains the value of *PProb* close to 5% for most of the cases and only increases if there is a lot of "free space" around it.

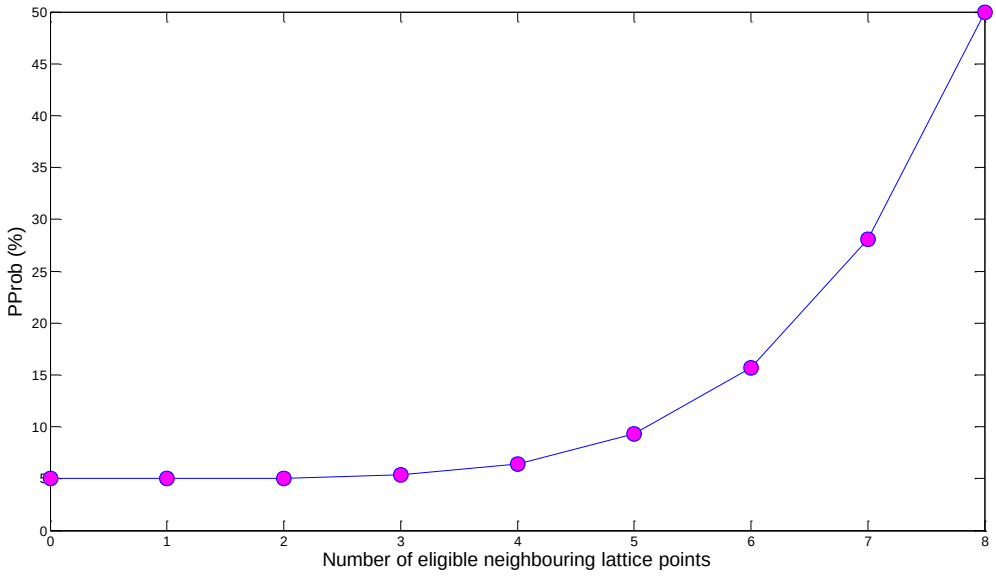

Figure V.21 - Variable PProb: the proliferation probability varies with the number of eligible lattice points around the SMC.

Results

The results are reported in the order they have been described in *Table V.4*, introducing increasing complexity to the model.

Figure V.22 compares results obtained in two extreme cases, the model with *No Theta* applied and the model with one *Arbitrary Theta* direction ($7/4\pi$) assigned to every single lattice point of the CM.

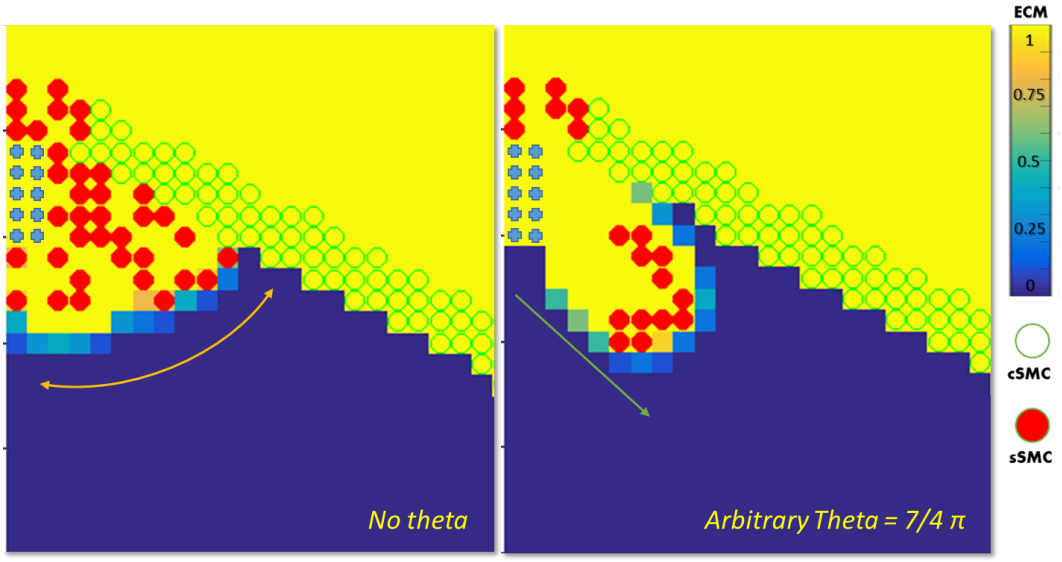

Figure V.22 - Comparison of results of the model without the influence of a *theta* value (*No Theta*, left panel) and a *theta* value that has been fixed for all the lattice points (*Arbitrary Theta*, right panel).

In both cases the workflow is followed until step 5, but then the coupling with ANSYS is switched off: in this way the vessel/stent geometry is the same as the complete CCM in both cases. In the first case, the result is similar to that shown in *Figure V.6*, with a neointima that grows in a rounded manner around the stent strut, whilst, in the second case, the neointima distinctly follows the direction of *theta* in its growth. This represents an "extreme" test case to validate that the presence of a very directional stress input has a noticeable effect on the neointimal growth; in the next steps the stress information coming from the *ANSYS* model is introduced.

Initially, the direction of cellular growth is determined using a *Single Principal direction*: *Figure V.23* represents the stresses resulting from the ANSYS model. The black arrows represent the orientation of the first principal stress in early iterations; the stresses are captured at the end of the systole, and it is noticeable how they are generally directed from the stent strut to the vessel wall.

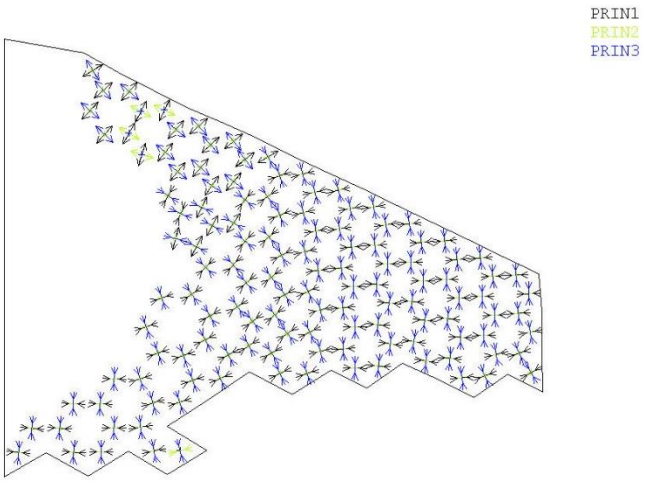

Figure V.23 - Principal stress directions in the neointima for the first ANSYS iteration for the *Single Principal Direction* model, with *theta* not randomised.

As it has been already shown how the introduction of a strict, arbitrary *theta* visibly changes the shape and direction of the growth of new tissue, it is expected that a model that constrains the migrating cells to move following these directions would show a growth that is more biased along the lumen, rather than outward from the strut region.

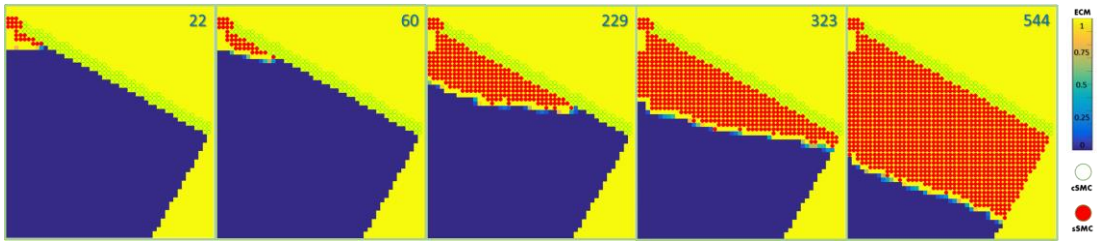

Figure V.24 – CM results of the neointimal growth for the *Single Principal Direction* model, at different time-steps, indicated in the right top corner.

Figure V.24 represents the results of this test at different time-points: it is visible how the shape of the neointima follows the direction imparted by the stress update, which is quite different from the results obtained through the stress-free model of the first section (*No Theta*, left panel of *Figure V.22*). In fact, the cells tend to invade the space between the strut and the vessel in a more "horizontal" shape, with the border forming a straight line between the strut and the vessel. This feature is maintained

throughout the whole simulation, even after the symmetry boundary of the model is reached and the strands of neointima join (*Figure V.25.a*). The CCM was run until the *exit* condition based on the WSS was met (*Figure V.25.b*), with a WSS value greater than 1.6: it is noticeable how by this point the shape of the neointima is rounded, similar to observed histology in the later stages of ISR (*Figure V.25.c* and bottom panels of *Figure V.8*). Running the same test model several times gave similar results.

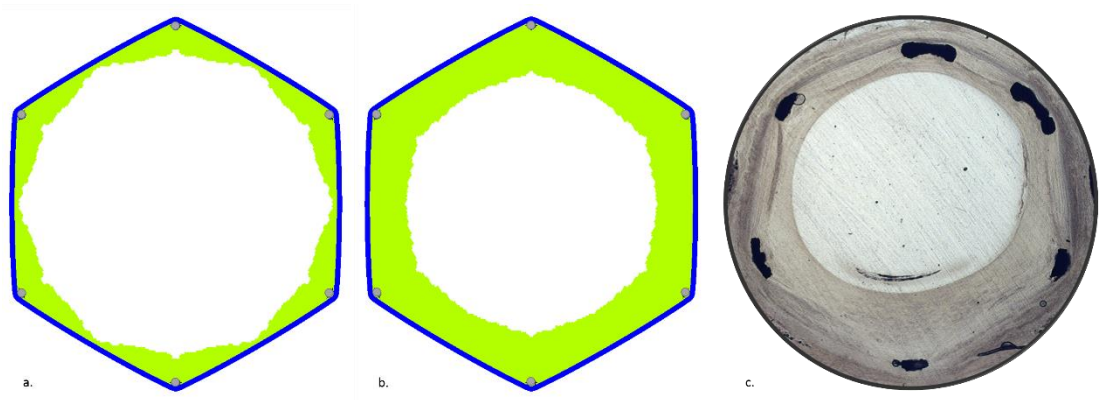

Figure V.25 – Symmetric expansion of the ANSYS results for the *Single Principal Direction* model, after 22 iterations (a) and 37 iterations, which correspond to the final situation when the *exit* condition is met (b), in comparison with a histologic image of a fully developed ISR, 28 day after stenting (c).

Finally, the full CCM model with *Dual Principal direction* was tested with the various settings introduced in the *Methods* section. These settings were combined and the results reported for different phases of the simulations: early, middle and late phases.

Early phase

The early results of the models with the settings described are reported in *Figure V.26*. This includes, on the left, the image of the model with *No Theta* and the detail of a histology image from the *in vivo* porcine model one week after stenting (as reported in *Figure V.9*). The figures have been chosen based on the amount of

neointima produced, rather than a specific time-step, to make the images more comparable.

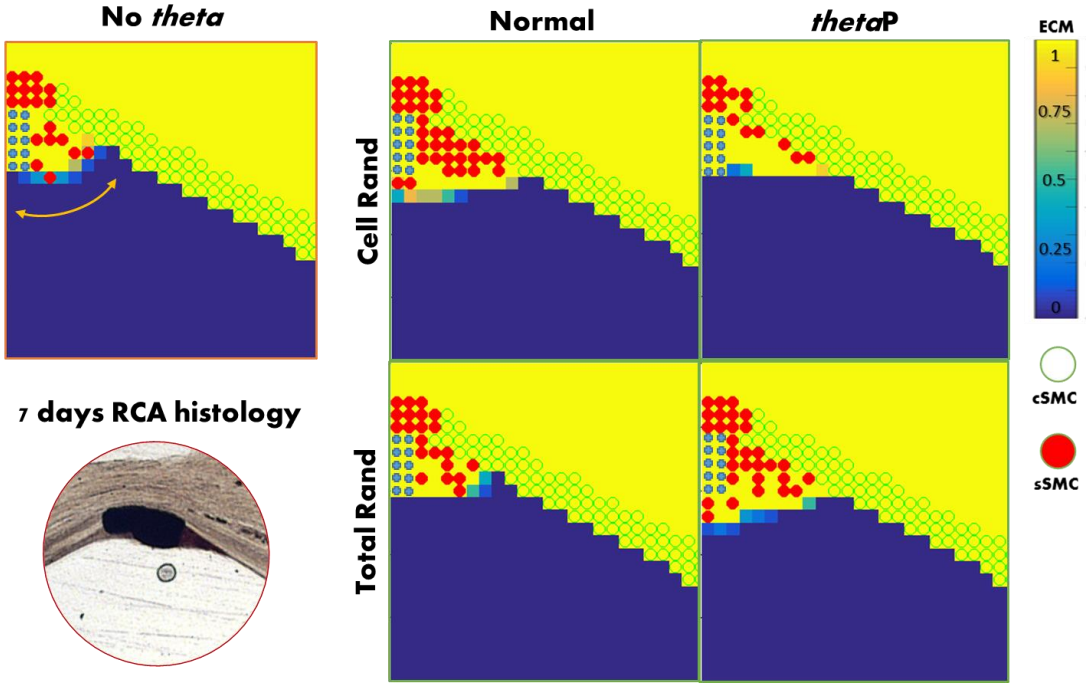

Figure V.26 - Results of the CCMs in the early phase of neointimal growth, compared to the model without the influence of *theta* on the top left and to a detail of one of the histological images of an *in vivo* ISR model, 7 days after stenting, on the bottom left.

At this early stage of growth, whilst there is some variation in the ratio of SMC/ECM and the shape of the ECM, all the models where *theta* is applied show a certain trend. The neointima tends to develop "horizontally", following lines between the stent strut and the vessel, which correspond to the direction of the first principal stress output from the ANSYS model. This looks similar to what is observed in histology (bottom left panel), and is not captured with the same model if the influence of *theta* is switched off (top left panel).

Middle phase

Results during the middle phase of the neointimal growth are reported in *Figure V.27* with images at two time-points for each run of the CCM, to give a better idea of its evolution in time.

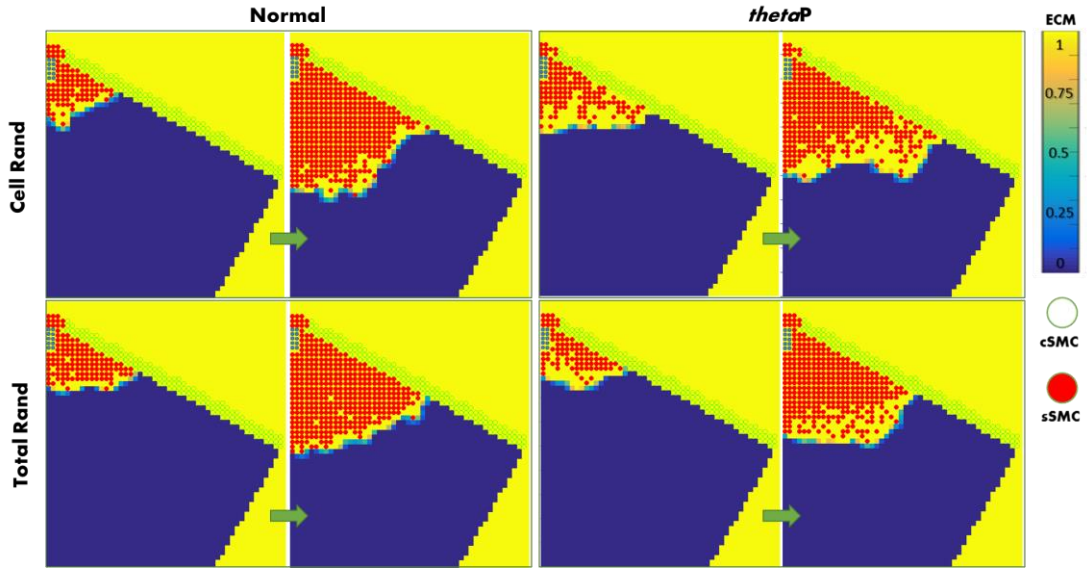

Figure V.27 - Results of the CCMs in the middle phase of neointimal growth: two time-steps are reported for each model.

At this stage, the differences between the models are more visible. In general, it is possible to notice how, extending the influence of *theta* also to the proliferating cells (*theta*P, on the right), the tendency to follow the neointimal stresses is maintained in a more consistent way throughout the simulation. The "Cell Rand – Normal" model starts showing more isotropic growth quite early, while the "Tot Rand – Normal" model maintains a more directional growth for longer, gradually becoming more isotropic.

Both the *theta*P models also show a lower ratio of SMC/ECM, which is likely to allow the influence of the stress direction to be more pronounced. The most promising results have been observed from the "Cell Rand – *theta*P" model, although this formulation shows poor repeatability.

Both models that employ the "Cell Rand" approach often demonstrate the effect of some "shooting SMCs" occurring in some of the simulations. This "Shooting SMC" effect happens over a few iterations of the CM after the last ANSYS solve. The cell creates ECM around itself, moves to one of the new lattice points with enough ECM and transports the *theta* value of the former position, as the new one was not part of the neointima at the last ANSYS iteration and does not have a *theta* value yet. From there, the SMC produces more ECM in its neighbourhood and keeps on moving in the same direction, determined by the *theta* value of its first position, or follows the *theta* direction of the lattice point if that part of neointima had a value assigned already. An example of such behaviour is provided in *Figure V.28*. This effect occurs much less, or never occurs, for the "Tot Rand" models.

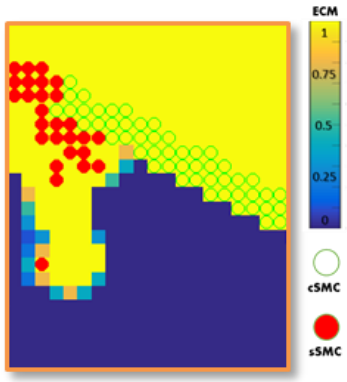

Figure V.28 - Example of the "shooting SMC" effect

Late phase

In almost all the CCMs where *theta* is randomised, with whatever combination of parameters and set ups, the growing neointima has not reached the opposite symmetry boundary (*Figure V.29*) when the *exit* condition is met (*WSS > 1.6*).

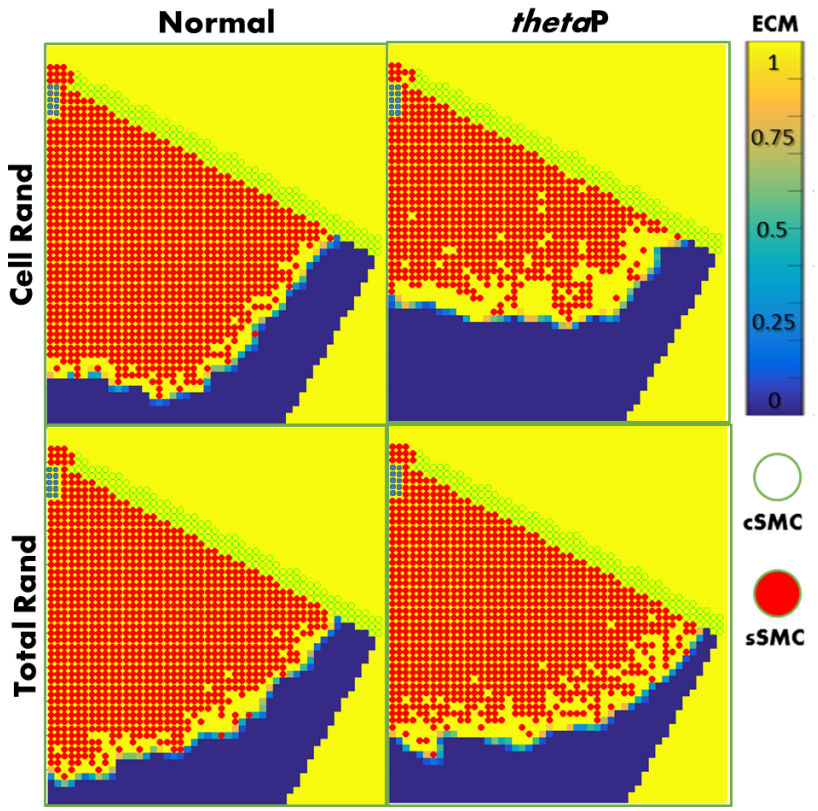

Figure V.29 - Results of the CCMs in the latest phase of neointimal growth, when the *exit* condition of the workflow determined by the WSS stops the simulation.

In some cases the shape of the neointima is flatter and in others more "rounded"; in some cases it is still possible to notice a directional growth and in other cases it appears more isotropic. This variability demonstrates how the implementation, and certain parameters, can affect the influence of *theta* on the overall growth (especially for the *theta*P models). In all cases the effect of the stress direction on the cellular behaviour is not sufficiently dominant to produce a circular intima as observed for the model with a *Single Principal direction* shown in *Figure V.25*.

Finally, some additional tests were performed: a set to test the influence of *base* and *PProb* parameters and a set to test the *Variable PProb* were performed. For higher values of *base* and *PProb*, the ratio of SMC/ECM is smaller, and the models tend to give a more controlled but rounded and isotropic behaviour, similar to the *no theta* models reported for the CM in the first section of this Chapter. The

Variable PProb setting, on the other hand, has been tested with a few of the settings proposed above: on one hand, the results appear to be less dependent on the "shooting SMCs" effect, but on the other hand, it seems to increase the SMC/ECM ratio, with more isotropic growth, especially in the middle and late phases.

Discussion

The model of in-stent restenosis introduced in the second part of this Chapter is based on the idea of providing information about the mechanical stimuli and its evolution during the process of the neointimal growth, influencing the cellular process. This is achieved through a frequent feedback between cellular model (CM) and ANSYS model. The passage of information between the two types of models occurs through a geometric correspondence. The CM is constructed using the geometry provided by the 2D FEM of stent expansion in a vessel, and the matching between ANSYS node position and lattice point locations is stored and used for all feedback.

This method generates the first issues with the CCM. The dimension of the lattice determines how smooth the profile of the neointima will be. A smoothing process would give a more realistic shape of neointima and it could address possible issues with the computational model. In fact, the creation of unnatural sharp edges in the ANSYS model might generate convergence problems. Whilst this was not seen in the current study, the possibility should be taken in consideration, especially if a less refined lattice is chosen.

This model has been developed as a means to test hypotheses about the process of ISR within a framework that can be adapted in terms of model set-up (dimension of lattice grid, frequency of feedback between CM and ANSYS, choice

of how to apply the stress to the CM) and in terms of the biological assumptions of the model (proliferation/migration rate, migration time). The results reported in this Chapter are a first attempt to test the potential of this CCM.

First, the ability to introduce a stress stimulus into the workflow has been tested through an *Arbitrary Theta* value that has been assigned to all the lattice points of the CM, without any update from ANSYS. The difference between the *Arbitrary Theta* and *No Theta* models is clearly visible as the growth follows the direction imposed through this fictitious stress. This ensures that the model works correctly before analysis of the full CCM where observations of isotropic growth could be due to either mistakes in the setting or too many random factors "covering" the effect of *theta*.

Subsequently, the complete workflow was run, first switching off the random choice for cells to follow either *theta* or *theta+180°*. This test with a *Single Principal direction* was meant to evaluate the function of the model with the simplest implementation. It is interesting that the images of these results show a shape of neointimal growth with greater similarity to observations from histology (*Figure V.9*) than any of the results reported from previous models of ISR, which show a more rounded growth around the stent strut (*Figure II.9* in Chapter 2) (Zahedmanesh, Van Oosterwyck et al. 2012). This is quite encouraging, as not only the initial phases of the growth, but also its evolution, especially the final neointimal shape when the *exit* criterion is met, look similar to the histological images from *in vivo* models, obtained from healthy animals, which is what this model attempts to replicate.

Finally, the full CCM with the *Dual Principal direction* method has been tested to determine what accentuates certain effects (for example, the "shooting SMCs" or

the tendency of the growth to become too isotropic). Various implementations were described in the *Methods* section and their results compared to provide understanding of the potential and flaws of the current CCM.

From analysis of the early stage of growth, all implementations of the model which include application of *theta* produce promising results. Both the difference with the more "rounded" results obtained from the *No Theta* model and the similarity with the shape and direction observed in histology are noticeable. For these models, the neointima tends to first occupy the space between the stent strut and the vessel following the line of the stresses produced by the pulsatility of the blood pressure. It is possible that the influence of the stress direction is particularly relevant in the early stages of ISR. The fact that this behaviour is observed with every model implementation supports the suggestion that the neointimal stress is influential in this early phase. However, it has to be noted that to obtain a more accurate representation of this phase of ISR, thrombosis should be included in a refinement of the model.

However, observing the evolution of later stages of growth it is visible how, whilst in some cases the first part of the middle phase has some similarity with the "*Single Principal direction*" model, the second part already has quite a "bulky" shape that looks increasingly different from what is observed in the histology images. With the current implementation, the regulation of cell growth based on the stress experienced by the neointima appears to have a significant effect only up to a certain time-step. At this point the "packing" of SMCs allows freedom only to a thin strip of SMC, which combines with the constraints of the lattice construction, making the

growth more isotropic, like in the simple test studies of the first section of the Chapter (*Figure V.3*), and the stress parameter has only a localised effect.

It is also noticeable that models with parameters that produce a low SMC/ECM ratio show more significant influence of *theta*. This was explored in the first section of the Chapter, with variation of *PProl* (probability of proliferation over migration) and *base* (the minimum amount of ECM required in a lattice point to allow a cell to occupy it), where high values of *PProl* and *base* resulted in "packing" of SMCs and a more consistent geometry of growth (*Figure V.3*). Lower values of these two parameters were chosen for the CCM to examine whether this results in greater sensitivity to the addition of the new parameter, *theta*. The tests performed on the CCM confirm this hypothesis, the higher the ratio of SMC/ECM, the more similar the results are to the original CM, with a more rounded shape of neointimal growth. However, with parameters that result in less "packing" of cells the results are more sensitive to random "shooting SMCs", as described in the *Results*. An approach to limit this effect was attempted with the *Variable PProb* method, assuming that cells that are more isolated are more likely to proliferate. These results showed control of this phenomenon, but produced more isotropic growth patterns. Lack of smoothness in neointimal boundaries is evident also in previous studies by other authors (Boyle, Lennon et al. 2011).

It is worth noting that all implementations where the influence of *theta* was applied to both migrating and proliferating SMCs (*theta*P) demonstrate more distinctively the influence of stress on the ISR. In these cases growth "stretches" more towards the vessel than the "Normal" set up at the same phase of growth (middle phase, *Figure V.27*) and maintains this behaviour for longer (late phase,

Figure V.29). The set up that gave results closest to those of the *Single Principal direction* model was the "CellRand – *theta*P" model, but these results were less repeatable than the "TotRand – *theta*P" model because the "shooting SMCs" effect occurred more frequently. When running several simulations for all models, the "CellRand" approach demonstrated less control than "TotRand" over these random effects, which probably occur more easily when the choice between *theta* and *theta+180°* occurs cell by cell. The "CellRand" method may create impediments to cellular movement in cases where SMCs at adjacent lattice points are orientated in opposite directions.

As the application of a preferential direction for cell growth is novel and has not been addressed in previous studies of ISR, there is no definitive approach. A series of assumptions have been made in these implementations and compared in order to explore this new aspect of modelling the evolution of ISR.

The greater similarity between the form of ISR observed in histology and the *Single Principle direction* model opens some questions about the assumptions. There may be effects that were not taken into consideration in this form of the model, such as cellular signalling phenomena that might give preference to the direction that takes the cell further from the site of initial injury. Experimental tests would be required to explore this hypothesis in more detail.

In Chapter 2 a comparison between models found in literature of ISR evolution was presented, including studies from Boyle *et al*. (Boyle, Lennon et al. 2013), Zahedmanesh *et al*. (Zahedmanesh, Van Oosterwyck et al. 2012) and Tahir *et al*. (Tahir, Bona-Casas et al. 2013). This model is similar to these previous studies, particularly the approach of Boyle *et al.*, due to the lattice definition for vessel and

lumen geometry. Most importantly, the stimulus considered the starting driver of the ISR process is the structural stress immediately after stenting, as reported by Boyle *et al*. and Zahedmanesh *et al*. In these previous studies this is investigated through FEM simulations, to provide initial conditions for the cellular model. Another similarity is that ECM is considered to play a role in SMC migration and proliferation. Whilst all these studies consider the main cellular component to be the SMC, Tahir *et al*. also considers the role of endothelial cells in the regulation of ISR: this cellular component has not been considered in this study. Also, the latter is the only model where the main mechanical stimulus, the wall shear stress in this case, is taken in consideration during its evolution along with the neointimal growth.

This study presents a few limitations, some of which have been discussed already. Whilst the method is novel, certain model implementations show unexpected results, for example the "shooting SMCs", and the reason is not always obvious. Some approaches have been proposed to limit these effects, but extra investigations would be required to gain a better understanding of what provokes them, in order to generate a better implementation of the model.

Another limitation of the model is the lattice nature of the CM, resulting in a finite element geometry that is similarly structured, with SMCs only able to move in eight possible directions. However, while it could be useful to improve the cellular rules, so they would resemble more what happens *in vivo* or *in vitro*, maintaining a lattice structure is also very useful for this type of CCM, as it creates the possibility of a simple location-based feedback between CM and ANSYS model and it is easy to control.

Evidence from Chapter 4 and from previous studies reviewed in Chapter 1 suggests that the local distribution of fluid shear stress participates in the process of ISR. In the CCM the impact of WSS is only used as a stopping condition of the entire algorithm. Observing the evolution of the neointimal growth, it is noticeable how, whilst results in the early phase resemble the histological images of *in vivo* models of ISR, this is less noticeable in later phases of the evolution, where the growth progresses outward from the stent strut location. Even if there is a tendency for growth toward the edges of the model, there is also considerable growth perpendicular to the lumen in all *Dual Principal direction* models, creating a "gap" in the area between two stent struts. With the hypothesis that areas of recirculation and low WSS experience an increase of cellular growth, the inclusion of the fluid shear stress to the CM would tend to flatten out this growth, promoting a more circular profile of the new lumen, more similar to *in vivo* ISR. However, as the fluid shear stress itself is dependent on the geometry the results of this study suggest that both neointimal stress and fluid stress may play a role in the evolution of ISR.

Finally, a simple isotropic elastic material model has been chosen for the neointima as the deformations it experiences are small. An aspect that could influence the results and has not been taken in consideration is the stress relaxation of the vessel wall over time due to the change in the wall constituents: this has been included in previous studies for arteries for different scopes, such as aneurysm development (Watton, Selimovic et al. 2011), and should be included in a future refinement of this model. The influence of fibre alignment with the stress direction could be also considered through definition of anisotropic material properties.

SUMMARY

This Chapter proposes the combined use of two models, a cellular one and a finite element one, to develop a more complete model of ISR which aims to capture the influence of the evolution of the stress in the neointima on tissue growth.

The main objective of this work is to propose a framework that allows testing of hypotheses related to ISR. Several implementations have been explored, increasing progressively the complexity of the framework from a purely cellular model in the first section, to the inclusion of the stress in the neointima with various strategies.

The most interesting results, which are consistent for most implementations, concern the early phases of the growth where the shape of the neointima presents noticeable similarities with what is observed in the histological images of experimental models of ISR. This is a novel result compared to what has been reported in previous studies.

However, as observed from the results of Chapter 4, the local fluid wall shear stress plays an important role in ISR, and further development of this model with the inclusion of the fluid effects on the growth might improve the understanding of the evolution of neointimal formation as a whole.

The cellular behaviour is complex and hard to represent in full; the implementation of the cell behaviour could be improved by means of *in vitro* testing which could allow validation of specific rules for the CCM. Some improvements to the model are suggested in the next Chapter.

CHAPTER VI – CONCLUSIONS AND FUTURE WORK

6.1 CONCLUSIONS

This thesis explores the problem of in-stent restenosis using modelling approaches as a tool to gain a deeper understanding of the phenomenon, with particular focus on the influence of mechanical stimuli on neointimal growth.

Many previous studies have evaluated the mechanical environment of the vessel immediately after stenting, from both a structural and fluid dynamic perspective, using models of various degrees of sophistication (Chapter 1). A smaller number of studies have attempted to model the development of ISR, based on either structural or fluid stimuli (Chapter 2). Whilst some contributing factors have been identified, the biological processes which regulate the initiation and evolution of ISR remain rather unclear.

This thesis explores the role of structural stresses in the development of ISR through incremental phases:

1. Development of a simple analytical model to understand the order of magnitude of stresses and strains in a stented vessel, replicating the stenting of a healthy porcine coronary artery;
2. Analysis of a 2D cross-section of a stented vessel to evaluate the structural stress, considered in this thesis to be a significant factor in the process of ISR;

3. Extension from 2D to a 3D model with realistic expanded stent geometry to investigate the correspondence between stent strut location and compressive forces. Comparison of structural results with fluid dynamic results obtained with the same geometry to describe the complete mechanical environment after stenting, investigation of the correlation between mechanical stimuli and measurements of ISR from histology in corresponding stent strut locations;
4. Development of a complex 2D model to study the evolution of ISR over time and the response to changes in structural stimuli. The model involves frequent feedback between a cellular model and a finite element model, in order to capture not only the cellular growth, but also the evolution of the stimulus with time.

The first phase, introduced in Chapter 2, is a simple analytical model which has been set up to explore how the expansion of a stent in a healthy vessel alters the mechanical environment from the physiological situation, from both a structural and fluid dynamic perspective. The importance of these changes arises from the fact that whilst vascular cells are constantly subject to mechanical forces, variation in the magnitude and direction of these loads can lead to a change in their behaviour through mechanotransduction mechanisms. Whilst this analysis is simple and represents the stenting process through uniform stent deployment, it allows the investigation of the influence of single parameters, such as expansion to various final radii, and provides a reference framework for the following, more complex models.

The extension of this work consists in phase 2 (Chapter 3), where the presence of the single stent struts is represented in a 2D model, developed both analytically and using the finite element method, with a focus on the structural

loads. Symmetric models with increasing numbers of stent struts and asymmetric models with uneven distributions of stent struts were explored to replicate typical strut distributions observed from histology of an *in vivo* porcine model. These results highlight how both the analytical and finite element models show the same trends for the symmetric models and the same variation in distribution of the stresses for the asymmetric case. However, the finite element model also captures the variation in stress across the thickness of the vessel and around its circumferential direction, which is essential for the development of a model that uses this information to drive cellular growth. In general, higher compressive stresses are found where the distance between two struts is greater.

The 2D model cannot consider out-of-plane effects. For this reason, the third phase for this research developed a full 3D model of a realistic stented vessel, reported in Chapter 4. The geometry of a real stent expanded into a porcine coronary artery was reconstructed and combined with an idealised cylindrical model of a vessel, allowing the evaluation of realistic stress distributions. The same stent-vessel model was used to examine the fluid dynamics within the stented vessel in a different research centre in Sheffield. Moreover, local histology data from the same study was available, permitting a comparison of the local compressive stress, wall shear stress and oscillatory shear index (to describe local variations in the mechanical environment immediately after stenting) with neointimal thickness observed in the *in vivo* model in the region of each stent strut. Although previous studies have tackled the combination of FEM, CFD and *in vivo* data, the results are averaged by section or use idealised stent geometry without a realistic expansion. The novelty of this work is the investigation of mechanical loads and relative neointimal growth localised to each stent strut. The results show how the correlation

between stimuli and ISR is stronger when the effect of structural and fluid dynamics are considered in combination, suggesting they both contribute to the phenomenon.

In order to achieve fully the aim of the thesis and examine the evolution of ISR in response to changes in structural stimuli, the 2D model developed in Chapter 3 was combined with a cellular model to create the coupled model described in Chapter 5. As in the previous models, the structural stress was considered as the primary stimulus. In this case the timeframe considered in the analysis is not just the acute response seen immediately after stenting, but it also includes the evolution of both the tissue growth and the mechanical stimulus over time. Structural stimuli considered included the compressive stress applied to the vessel wall directly underneath the stent strut (initial injury) and also the direction of first principal stress which directs the cellular growth within the neointima. The novelty of this study lies in the continuous feedback between the cellular model and the ANSYS model, allowing frequent update of the geometry of the finite element model during neointimal growth. Therefore, there is a regular update of the stress information that regulates the cellular processes. The model was used to investigate various implementation options and the influence of specific model parameters. Analysis of the results highlighted aspects of the biological response captured by this novel approach, but also demonstrated the need for future refinement of the method. The outcomes obtained show promising results for the early phases of neointimal growth, where the distribution of new tissue agrees the observations from histology filling the gap between the strut and the vessel, following the direction of the circumference of the vessel. In later phases, this tendency is progressively lost and a more isotropic response is observed.

6.1 FUTURE WORK

As described above, this thesis reports a series of models of increasing complexity which builds up to the results presented in Chapters 4 and 5 for a 3D realistic stented vessel and the 2D coupled cellular model (CCM) of ISR. However, these models are subject to some limitations, providing opportunities for further improvement and refinement.

The 3D model allows data to be obtained throughout the stented region from many different locations to allow analysis of the response over many stent struts. However, full validation of the relationship between stimuli and biological response requires such an analysis to be repeated for several stent expansions in different animals, to take into account potential differences in the response between experiments.

The vessel geometry assumed for the 3D model is idealised and does not include the natural tapering of the vessel, which will have an impact on the resulting stresses, with higher stresses reported for sections of the vessel with a smaller initial radius. The material model used for this 3D model was taken from the literature and represents a SEDF for human tissue. Further work could include the use of material properties for porcine tissue and the extension of the model to include variation in response of the layers of the vessel wall.

Due to the complexity of the CCM, assumptions are required in the setup, which present some limitations of the approach. First of all, this setup does not take in consideration all the steps of neointima formation: as introduced in Chapter 1, the very first reaction to stent implantation, occurring within the first few days, is the formation of the thrombus, due to the deposition of platelets from the circulating

blood. This thin layer of blood clot is believed to be the first element filling the space between the stent strut and the vessel: for this reason, although it has been shown that SMCs play a dominant role in neointima formation, the thrombosis has to be included in a refinement of the ISR model in order to obtain more reliable representation of the reaction to stenting.

Additionally, the cellular ruleset assumed for this model is quite simple and neglects some effects such as apoptosis and extracellular matrix degradation. These simple rules attempt to capture the detail of complex biological processes including cellular proliferation and ECM production but could be developed further to include more realistic rules relating to cell signalling, variation in ECM production over time and variable distances of cell migration within a time-step. The definition of time within the CCM is dependent on assumptions incorporated within the cellular ruleset and, as a result, it is challenging to relate a "time-step" of the model to a defined increment of real time. This aspect needs to be considered in future development of the model. Refinement of these rules would require specific focus on the biological processes and should be developed in collaboration with experts in this field. In particular, such rules might be informed by controlled *in vitro* experiments to quantify specific aspects of cellular behaviour.

From the 2D model in Chapter 3 it has been observed how an uneven distribution of stent struts in the cross-section can affect magnitude and distribution of the compressive stress. Simulation of the CCM over the entire cross-section would establish whether variation in the initial stress distribution is significant enough to result in a noticeable difference in neointimal growth. Comparison of the 2D model of Chapter 3 and the 3D model of Chapter 4 demonstrates that out-of-plane effects play a role in determining the magnitude of the mechanical load underneath a stent

strut. Extension of the CCM framework to a 3D simulation would capture these effects, but would require a considerable amount of computational power and memory. Prior to extension to 3D strategies to reduce the computational cost of the process should be considered, such as testing the minimum feedback frequency required between the CM and the ANSYS model without decreasing the validity of the model. In addition, extension to 3D could be attempted combining the framework from Chapter 5 with the approach use in Chapter 4, using the same realistic expanded stent geometry and allowing comparison between neointimal growth from the CCM with histology measurements from the porcine model.

A consideration emerging from the results of the 3D model is the need to consider both structural mechanics and fluid dynamics. The inclusion of local variations in fluid wall stress would be a valuable addition to the CCM and might help better predict the outcome of stenting. An example of this is the later phases of growth, where cells in the neointima between stent struts might experience lower WSS, which may promote more even growth along the circumference, resulting in the development of a circular luminal profile.

An important aspect that concerns the representation of the stress in the vessel wall regards the effect of stress relaxation; ISR is a phenomenon that occurs in a time-scale between weeks and months, and the remodelling of this tissue over time might reduce stress in the wall. This has not been included in this work, but it is important to consider, as this may influence stresses in the neointima; it could be included computationally through a viscoelastic material model, but there is no certain data about the parameters to choose, so more research would be needed in order to refine the present model of ISR.

Some studies have suggested that endothelial cells may play a role in stopping the neointimal growth. Although this cell type is not currently included in the CCM, the framework has the potential to represent endothelial cell behaviour, providing appropriate rules could be defined.

Finally, in addition to the results presented within this thesis, the work in Chapter 5 provides a framework for further investigation of the interaction between mechanical stimuli and the biological response during ISR. This framework is also compatible with the approach taken in Chapter 4, allowing extension to 3D and complex geometries, and can also be extended to incorporate more complex biological rules. The novelty of this thesis is the coupling between the cellular and finite element models of ISR and the demonstration that cellular growth driven by variations in stress direction captures aspects of the biological response.

REFERENCES

https://commons.wikimedia.org/wiki/File%3ACoronary_arteries.svg

https://commons.wikimedia.org/wiki/File%3ABlausen_0259_CoronaryArteryDisease_02.png

https://commons.wikimedia.org/wiki/File%3ACell_Cycle_2-2.svg

http://medgadget.com/archives/2008/09/micro_drug_eluting_coronary_stent_gets_fda_ok.html

Amatruda, C. M., C. Bona Casas, B. K. Keller, H. Tahir, G. Dubini, A. Hoekstra, D. R. Hose, P. Lawford, F. Migliavacca, A. J. Narracott and J. Gunn (2014). "From histology and imaging data to models for in-stent restenosis." Int J Artif Organs **37**(10): 786-800.

Axel, D. I., W. Kunert, C. Goggelmann, M. Oberhoff, C. Herdeg, A. Kuttner, D. H. Wild, B. R. Brehm, R. Riessen, G. Koveker and K. R. Karsch (1997). "Paclitaxel inhibits arterial smooth muscle cell proliferation and migration in vitro and in vivo using local drug delivery." Circulation **96**(2): 636-645.

Bangalore, S., B. Toklu, N. Amoroso, M. Fusaro, S. Kumar, E. L. Hannan, D. P. Faxon and F. Feit (2013). "Bare metal stents, durable polymer drug eluting stents, and biodegradable polymer drug eluting stents for coronary artery disease: mixed treatment comparison meta-analysis." BMJ **347**: f6625.

Beamish, J. A., P. He, K. Kottke-Marchant and R. E. Marchant (2010). "Molecular regulation of contractile smooth muscle cell phenotype: implications for vascular tissue engineering." Tissue Eng Part B Rev **16**(5): 467-491.

Bedoya, J., C. A. Meyer, L. H. Timmins, M. R. Moreno and J. E. Moore (2006). "Effects of stent design parameters on normal artery wall mechanics." J Biomech Eng **128**(5): 757-765.

Berry, J. L., E. Manoach, C. Mekkaoui, P. H. Rolland, J. E. Moore, Jr. and A. Rachev (2002). "Hemodynamics and wall mechanics of a compliance matching stent: in vitro and in vivo analysis." J Vasc Interv Radiol **13**(1): 97-105.

Boyle, C. J., A. B. Lennon, M. Early, D. J. Kelly, C. Lally and P. J. Prendergast (2010). "Computational simulation methodologies for mechanobiological modelling: a cell-centred approach to neointima development in stents." Philos Transact A Math Phys Eng Sci **368**(1921): 2919-2935.

Boyle, C. J., A. B. Lennon and P. J. Prendergast (2011). "In silico prediction of the mechanobiological response of arterial tissue: application to angioplasty and stenting." J Biomech Eng **133**(8): 081001.

Boyle, C. J., A. B. Lennon and P. J. Prendergast (2013). "Application of a mechanobiological simulation technique to stents used clinically." J Biomech **46**(5): 918-924.

Butany, J., K. Carmichael, S. W. Leong and M. J. Collins (2005). "Coronary artery stents: identification and evaluation." J Clin Pathol **58**(8): 795-804.

Caiazzo, A., D. Evans, J. Falcone and J. Hegewald (2009). "Towards a Complex Automata Multiscale Model of In-Stent Restenosis." Computational Science - ICCS 2009 **5544/2009**: 705-714.

Chen, H. Y., A. K. Sinha, J. S. Choy, H. Zheng, M. Sturek, B. Bigelow, D. L. Bhatt and G. S. Kassab (2011). "Mis-sizing of stent promotes intimal hyperplasia: impact of endothelial shear and intramural stress." Am J Physiol Heart Circ Physiol **301**(6): H2254-2263.

Cheng, R., Y. G. Lai and K. B. Chandran (2004). "Three-dimensional fluid-structure interaction simulation of bileaflet mechanical heart valve flow dynamics." Ann Biomed Eng **32**(11): 1471-1483.

Chiu, J.-J., L.-J. Chen, C.-N. Chen, P.-L. Lee and C.-I. Lee (2004). "A model for studying the effect of shear stress on interactions between vascular endothelial cells and smooth muscle cells." Journal of Biomechanics **37**(4): 531-539.

Christen, T., V. Verin, M. Bochaton-Piallat, Y. Popowski, F. Ramaekers, P. Debruyne, E. Camenzind, G. van Eys and G. Gabbiani (2001). "Mechanisms of neointima formation and remodeling in the porcine coronary artery." Circulation **103**(6): 882-888.

Conway, C., F. Sharif, J. P. McGarry and P. E. McHugh (2012). "A Computational Test-Bed to Assess Coronary Stent Implantation Mechanics Using a Population-Specific Approach." Cardiovascular Engineering and Technology **3**(4): 374-387.

Crowther, M. A. (2005). "Pathogenesis of Atherosclerosis." ASH Education Program Book **2005**(1): 436-441.

De Beule, M., P. Mortier, S. G. Carlier, B. Verhegghe, R. Van Impe and P. Verdonck (2008). "Realistic finite element-based stent design: the impact of balloon folding." J Biomech **41**(2): 383-389.

Dean, C. J., A. C. Morton, N. D. Arnold, D. R. Hose, D. C. Crossman and J. Gunn (2005). "Relative importance of the components of stent geometry to stretch induced in-stent neointima formation." Heart **91**(12): 1603-1604.

Dobrin, P. B. (1978). "Mechanical properties of arterises." Physiol Rev **58**(2): 397-460.

Driessen, N. J., C. V. Bouten and F. P. Baaijens (2005). "A structural constitutive model for collagenous cardiovascular tissues incorporating the angular fiber distribution." J Biomech Eng **127**(3): 494-503.

Duraiswamy, N., B. Jayachandran, J. Byrne, J. E. Moore, Jr. and R. T. Schoephoerster (2005). "Spatial distribution of platelet deposition in stented arterial models under physiologic flow." Ann Biomed Eng **33**(12): 1767-1777.

Duraiswamy, N., R. T. Schoephoerster, M. R. Moreno and J. E. Moore (2007). "Stented artery flow patterns and their effects on the artery wall." Annual Review of Fluid Mechanics **39**: 357-382.

Edelman, E. R. and C. Rogers (1998). "Pathobiologic Responses to Stenting." The American Journal of Cardiology **81**(7, Supplement 1): 4E-6E.

Edelman, E. R. and C. Rogers (1998). "Pathobiologic responses to stenting." Am J Cardiol **81**(7A): 4E-6E.

Evans, D. J., P. V. Lawford, J. Gunn, D. Walker, D. R. Hose, R. H. Smallwood, B. Chopard, M. Krafczyk, J. Bernsdorf and A. Hoekstra (2008). "The application of multiscale modelling to the process of development and prevention of stenosis in a stented coronary artery." Philos Transact A Math Phys Eng Sci **366**(1879): 3343-3360.

Gijsen, F. J., F. Migliavacca, S. Schievano, L. Socci, L. Petrini, A. Thury, J. J. Wentzel, A. F. van der Steen, P. W. Serruys and G. Dubini (2008). "Simulation of stent deployment in a realistic human coronary artery." Biomed Eng Online **7**: 23.

Gunn, J., N. Arnold, K. H. Chan, L. Shepherd, D. C. Cumberland and D. C. Crossman (2002). "Coronary artery stretch versus deep injury in the development of in-stent neointima." Heart **88**(4): 401-405.

Gunn, J. and D. Cumberland (1999). "Does stent design influence restenosis?" European Heart Journal **20**(14): 1009-1013.

Gupta, V. and K. J. Grande-Allen (2006). "Effects of static and cyclic loading in regulating extracellular matrix synthesis by cardiovascular cells." Cardiovasc Res **72**(3): 375-383.

Hara, H., M. Nakamura, J. C. Palmaz and R. S. Schwartz (2006). "Role of stent design and coatings on restenosis and thrombosis." Adv Drug Deliv Rev **58**(3): 377-386.

Holzapfel, G. A. (2006). "Determination of material models for arterial walls from uniaxial extension tests and histological structure." J Theor Biol **238**(2): 290-302.

Holzapfel, G. A., T. C. Gasser and R. W. Ogden (2000). "A new constitutive framework for arterial wall mechanics and a comparative study of material models." Journal of Elasticity **61**(1-3): 1-48.

Holzapfel, G. A. and R. W. Ogden (2010). "Constitutive modelling of arteries." Proceedings of the Royal Society A: Mathematical, Physical and Engineering Science **466**(2118): 1551-1597.

Huo, Y., J. S. Choy, M. Svendsen, A. K. Sinha and G. S. Kassab (2009). "Effects of vessel compliance on flow pattern in porcine epicardial right coronary arterial tree." J Biomech **42**(5): 594-602.

Iqbal, J., J. Gunn and P. W. Serruys (2013). "Coronary stents: historical development, current status and future directions." Br Med Bull **106**: 193-211.

Iqbal, J., Y. Onuma, J. Ormiston, A. Abizaid, R. Waksman and P. Serruys (2014). "Bioresorbable scaffolds: rationale, current status, challenges, and future." Eur Heart J **35**(12): 765-776.

Jones, G. and S. Chapman (2012). "Modeling Growth in Biological Materials." SIAM Review **54**(1): 52-118.

Kalita, P. and R. Schaefer (2008). "Mechanical Models of Artery Walls." Archives of Computational Methods in Engineering **15**(1): 1-36.

Keller, B., C. Amatruda, D. R. Hose, J. Gunn, P. Lawford, G. Dubini, F. Migliavacca and A. Narracott (2014). "Contribution of Mechanical and Fluid Stresses to the Magnitude of In-stent Restenosis at the Level of Individual Stent Struts." Cardiovascular Engineering and Technology: 1-12.

Kim, M. S. and L. S. Dean (2011). "In-Stent Restenosis." Cardiovascular Therapeutics **29**(3): 190-198.

Kroll, M. H., J. D. Hellums, L. V. McIntire, A. I. Schafer and J. L. Moake (1996). "Platelets and shear stress." Blood **88**(5): 1525-1541.

LaDisa, J. F., Jr., L. E. Olson, R. C. Molthen, D. A. Hettrick, P. F. Pratt, M. D. Hardel, J. R. Kersten, D. C. Warltier and P. S. Pagel (2005). "Alterations in wall shear stress predict sites of neointimal hyperplasia after stent implantation in rabbit iliac arteries." Am J Physiol Heart Circ Physiol **288**(5): H2465-2475.

Le Breton, H., E. F. Plow and E. J. Topol (1996). "Role of platelets in restenosis after percutaneous coronary revascularization." J Am Coll Cardiol **28**(7): 1643-1651.

Lehoux, S. and A. Tedgui (2003). "Cellular mechanics and gene expression in blood vessels." J Biomech **36**(5): 631-643.

Li, S., C. Van Den Diepstraten, S. J. D'Souza, B. M. Chan and J. G. Pickering (2003). "Vascular smooth muscle cells orchestrate the assembly of type I collagen via alpha2beta1 integrin, RhoA, and fibronectin polymerization." Am J Pathol **163**(3): 1045-1056.

Libby, P. and P. Theroux (2005). "Pathophysiology of coronary artery disease." Circulation **111**(25): 3481-3488.

Linder-Ganz, E., S. Engelberg, M. Scheinowitz and A. Gefen (2006). "Pressure-time cell death threshold for albino rat skeletal muscles as related to pressure sore biomechanics." J Biomech **39**(14): 2725-2732.

Lusis, A. J. (2000). "Atherosclerosis." Nature **407**(6801): 233-241.

Malik, N., J. Gunn, C. M. Holt, L. Shepherd, S. E. Francis, C. M. Newman, D. C. Crossman and D. C. Cumberland (1998). "Intravascular stents: a new technique for tissue processing for histology, immunohistochemistry, and transmission electron microscopy." Heart **80**(5): 509-516.

Maurel, W., Wu, Y., Magnenat Thalmann, N., Thalmann, D. (1998). Biomechanical Models for Soft-Tissue Simulation. Berlin, Springer.

Members, T. F., G. Montalescot, U. Sechtem, S. Achenbach, F. Andreotti, C. Arden, A. Budaj, R. Bugiardini, F. Crea, T. Cuisset, C. Di Mario, J. R. Ferreira, B. J. Gersh, A. K. Gitt, J.-S. Hulot, N. Marx, L. H. Opie, M. Pfisterer, E. Prescott, F. Ruschitzka, M. Sabaté, R. Senior, D. P. Taggart, E. E. van der Wall, C. J. M. Vrints, E. C. f. P. Guidelines, J. L. Zamorano, S. Achenbach, H. Baumgartner, J. J. Bax, H. Bueno, V. Dean, C. Deaton, C. Erol, R. Fagard, R. Ferrari, D. Hasdai, A. W. Hoes, P. Kirchhof, J. Knuuti, P. Kolh, P. Lancellotti, A. Linhart, P. Nihoyannopoulos, M. F. Piepoli, P. Ponikowski, P. A. Sirnes, J. L. Tamargo, M. Tendera, A. Torbicki, W. Wijns, S. Windecker, D. Reviewers, J. Knuuti, M. Valgimigli, H. Bueno, M. J. Claeys, N. Donner-Banzhoff, C. Erol, H. Frank, C. Funck-Brentano, O. Gaemperli, J. R. Gonzalez-Juanatey, M. Hamilos, D. Hasdai, S. Husted, S. K. James, K. Kervinen, P. Kolh, S. D. Kristensen, P. Lancellotti, A. P. Maggioni, M. F. Piepoli, A. R. Pries, F. Romeo, L. Rydén, M. L. Simoons, P. A. Sirnes, P. G. Steg, A. Timmis, W. Wijns, S. Windecker, A. Yildirir and J. L. Zamorano (2013). "2013 ESC guidelines on the management of stable coronary artery disease: The Task Force on the management of stable coronary artery disease of the European Society of Cardiology." European Heart Journal.

Miller, D. D., M. A. Karim, W. D. Edwards and R. S. Schwartz (1996). "Relationship of vascular thrombosis and inflammatory leukocyte infiltration to neointimal growth following porcine coronary artery stent placement." Atherosclerosis **124**(2): 145-155.

Mongrain, R. and J. Rodes-Cabau (2006). "Role of shear stress in atherosclerosis and restenosis after coronary stent implantation." Rev Esp Cardiol (Engl Ed) **59**(1): 1-4.

Moore, J., Jr. and J. L. Berry (2002). "Fluid and solid mechanical implications of vascular stenting." Ann Biomed Eng **30**(4): 498-508.

Morlacchi, S., B. Keller, P. Arcangeli, M. Balzan, F. Migliavacca, G. Dubini, J. Gunn, N. Arnold, A. Narracott, D. Evans and P. Lawford (2011). "Hemodynamics and in-stent restenosis: micro-CT images, histology, and computer simulations." Ann Biomed Eng **39**(10): 2615-2626.

Morlacchi, S. and F. Migliavacca (2013). "Modeling stented coronary arteries: where we are, where to go." Ann Biomed Eng **41**(7): 1428-1444.

Nichols, W. W., M. F. O'Rourke and D. A. McDonald (2005). McDonald's blood flow in arteries : theoretical, experimental, and clinical principles. London

New York.

Ong, A. T., J. Aoki, E. P. McFadden and P. W. Serruys (2004). "Classification and current treatment options of in-stent restenosis. Present status and future perspectives." Herz **29**(2): 187-194.

Ozolanta, I., G. Tetere, B. Purinya and V. Kasyanov (1998). "Changes in the mechanical properties, biochemical contents and wall structure of the human coronary arteries with age and sex." Med Eng Phys **20**(7): 523-533.

Prendergast, P. J., C. Lally, S. Daly, A. J. Reid, T. C. Lee, D. Quinn and F. Dolan (2003). "Analysis of prolapse in cardiovascular stents: a constitutive equation for vascular tissue and finite-element modelling." J Biomech Eng **125**(5): 692-699.

Ramanathan, T. and H. Skinner (2005). "Coronary blood flow." Continuing Education in Anaesthesia, Critical Care & Pain **5**(2): 61-64.

Rensen, S. S., P. A. Doevendans and G. J. van Eys (2007). "Regulation and characteristics of vascular smooth muscle cell phenotypic diversity." Neth Heart J **15**(3): 100-108.

Roy, S., C. Boss, R. Rezakhaniha and N. Stergiopulos (2010). "Experimental characterization of the distribution of collagen fiber recruitment." Journal of Biorheology **24**(2): 84-93.

Rzucidlo, E. M., K. A. Martin and R. J. Powell (2007). "Regulation of vascular smooth muscle cell differentiation." Journal of Vascular Surgery **45**(6, Supplement): A25-A32.

Sahni, D., G. D. Kaur, H. Jit and I. Jit (2008). "Anatomy & distribution of coronary arteries in pig in comparison with man." Indian J Med Res **127**(6): 564-570.

Sanmartin, M., J. Goicolea, C. Garcia, J. Garcia, A. Crespo, J. Rodriguez and J. M. Goicolea (2006). "[Influence of shear stress on in-stent restenosis: in vivo study using 3D reconstruction and computational fluid dynamics]." Rev Esp Cardiol **59**(1): 20-27.

Schiele, T. M. (2005). "Current understanding of coronary in-stent restenosis. Pathophysiology, clinical presentation, diagnostic work-up, and management." Z Kardiol **94**(11): 772-790.

Schwartz, R. S., A. Chu, W. D. Edwards, S. S. Srivatsa, R. D. Simari, J. M. Isner and D. R. Holmes, Jr. (1996). "A proliferation analysis of arterial neointimal hyperplasia: lessons for antiproliferative restenosis therapies." Int J Cardiol **53**(1): 71-80.

Seo, T., L. G. Schachter and A. I. Barakat (2005). "Computational study of fluid mechanical disturbance induced by endovascular stents." Ann Biomed Eng **33**(4): 444-456.

Serruys, P. W., H. M. Garcia-Garcia and Y. Onuma (2012). "From metallic cages to transient bioresorbable scaffolds: change in paradigm of coronary revascularization in the upcoming decade?" European Heart Journal **33**(1): 16-25b.

Sigwart, U., J. Puel, V. Mirkovitch, F. Joffre and L. Kappenberger (1987). "Intravascular stents to prevent occlusion and restenosis after transluminal angioplasty." N Engl J Med **316**(12): 701-706.

Stankovicova, T., M. Szilard, I. De Scheerder and K. R. Sipido (2000). "M cells and transmural heterogeneity of action potential configuration in myocytes from the left ventricular wall of the pig heart." Cardiovasc Res **45**(4): 952-960.

Stettler, C., S. Wandel, S. Allemann, A. Kastrati, M. C. Morice, A. Schömig, M. E. Pfisterer, G. W. Stone, M. B. Leon, J. S. de Lezo, J.-J. Goy, S.-J. Park, M. Sabaté, M. J. Suttorp, H. Kelbaek, C. Spaulding, M. Menichelli, P. Vermeersch, M. T. Dirksen, P. Cervinka, A. S. Petronio, A. J. Nordmann, P. Diem, B. Meier, M. Zwahlen, S. Reichenbach, S. Trelle, S. Windecker and P. Jüni (2007). "Outcomes associated with drug-eluting and bare-metal stents: a collaborative network meta-analysis." The Lancet **370**(9591): 937-948.

Tahir, H., C. Bona-Casas and A. G. Hoekstra (2013). "Modelling the effect of a functional endothelium on the development of in-stent restenosis." PLoS One **8**(6): e66138.

Tahir, H., A. G. Hoekstra, E. Lorenz, P. V. Lawford, D. R. Hose, J. Gunn and D. J. Evans (2011). "Multi-scale simulations of the dynamics of in-stent restenosis: impact of stent deployment and design." Interface Focus **1**(3): 365-373.

Takashima, K., T. Kitou, K. Mori and K. Ikeuchi (2007). "Simulation and experimental observation of contact conditions between stents and artery models." Med Eng Phys **29**(3): 326-335.

Tamai, H., K. Igaki, E. Kyo, K. Kosuga, A. Kawashima, S. Matsui, H. Komori, T. Tsuji, S. Motohara and H. Uehata (2000). "Initial and 6-month results of biodegradable poly-l-lactic acid coronary stents in humans." Circulation **102**(4): 399-404.

Tambe, D. T., C. C. Hardin, T. E. Angelini, K. Rajendran, C. Y. Park, X. Serra-Picamal, E. H. Zhou, M. H. Zaman, J. P. Butler, D. A. Weitz, J. J. Fredberg and X. Trepat (2011). "Collective cell guidance by cooperative intercellular forces." Nat Mater **10**(6): 469-475.

Thyberg, J., U. Hedin, M. Sjolund, L. Palmberg and B. A. Bottger (1990). "Regulation of differentiated properties and proliferation of arterial smooth muscle cells." Arteriosclerosis **10**(6): 966-990.

Timmins, L. H., C. A. Meyer, M. R. Moreno and J. E. Moore, Jr. (2008). "Mechanical modeling of stents deployed in tapered arteries." Ann Biomed Eng **36**(12): 2042-2050.

Timmins, L. H., M. W. Miller, F. J. Clubb, Jr. and J. E. Moore, Jr. (2011). "Increased artery wall stress post-stenting leads to greater intimal thickening." Lab Invest **91**(6): 955-967.

Townsend, N., M. Nichols, P. Scarborough and M. Rayner (2015). "Cardiovascular disease in Europe - epidemiological update 2015." Eur Heart J.

van Andel, C. J., P. V. Pistecky and C. Borst (2003). "Mechanical properties of porcine and human arteries: implications for coronary anastomotic connectors." Ann Thorac Surg **76**(1): 58-64; discussion 64-55.

van Beusekom, H. M. and P. W. Serruys (2010). "Drug-eluting stent endothelium: presence or dysfunction." JACC Cardiovasc Interv **3**(1): 76-77.

van den Broek, C. N., A. van der Horst, M. C. Rutten and F. N. van de Vosse (2011). "A generic constitutive model for the passive porcine coronary artery." Biomech Model Mechanobiol **10**(2): 249-258.

VanBavel, E., P. Siersma and J. A. Spaan (2003). "Elasticity of passive blood vessels: a new concept." Am J Physiol Heart Circ Physiol **285**(5): H1986-2000.

Vito, R. P. and S. A. Dixon (2003). "Blood vessel constitutive models-1995-2002." Annu Rev Biomed Eng **5**: 413-439.

Wang, J. H. and B. P. Thampatty (2006). "An introductory review of cell mechanobiology." Biomech Model Mechanobiol **5**(1): 1-16.

Wang, W. Q., D. K. Liang, D. Z. Yang and M. Qi (2006). "Analysis of the transient expansion behavior and design optimization of coronary stents by finite element method." J Biomech **39**(1): 21-32.

Watton, P. N., A. Selimovic, N. B. Raberger, P. Huang, G. A. Holzapfel and Y. Ventikos (2011). "Modelling evolution and the evolving mechanical environment of saccular cerebral aneurysms." Biomech Model Mechanobiol **10**(1): 109-132.

Zahedmanesh, H. and C. Lally (2012). "A multiscale mechanobiological modelling framework using agent-based models and finite element analysis: application to vascular tissue engineering." Biomech Model Mechanobiol **11**(3-4): 363-377.

Zahedmanesh, H., H. Van Oosterwyck and C. Lally (2012). "A multi-scale mechanobiological model of in-stent restenosis: deciphering the role of matrix metalloproteinase and extracellular matrix changes." Comput Methods Biomech Biomed Engin.

APPENDIX

PUBLICATIONS

Journal Articles

- Keller*****, B., **C. Amatruda***, D. R. Hose, J. Gunn, P. Lawford, G. Dubini, F. Migliavacca and A. Narracott (2014). *Contribution of Mechanical and Fluid Stresses to the Magnitude of In-stent Restenosis at the Level of Individual Stent Struts.* Cardiovascular Engineering and Technology: 1-12. (*****These authors shared first authorship)

- **Amatruda, C. M.***, C. Bona Casas*****, B. K. Keller*****, H. Tahir*****, G. Dubini, A. Hoekstra, D. R. Hose, P. Lawford, F. Migliavacca, A. J. Narracott and J. Gunn (2014). *From histology and imaging data to models for in-stent restenosis.* Int J Artif Organs **37**(10): 786-800. (*****These authors shared first authorship)

Conference proceedings

- **Amatruda, C. M.**, D. R. Hose, P. Lawford and A. Narracott (2011). *Modelling the Development of In-Stent Restenosis: Preliminary Results of a Structural Model.* International Conference on Advancements of Medicine and Health Care through Technology. S. Vlad and R. V. Ciupa, Springer Berlin Heidelberg. 36: 276-279. DOI: 10.1007/978-3-642-22586-4_58

Book Chapter

- **Claudia M Amatruda**, D Rodney Hose , Patricia V Lawford , Julian Gunn, Andrew J Narracott (2013) *Chapter 8 – Modelling of In-Stent Restenosis: From Stent/Vessel Interactions to Tissue Growth.* Medical Devices Design in

Cardiovascular Applications By the MeDDiCA Research Team, Mechanical Engineering Department, University College London, UK. ISBN 978-0-9576347-1-8
http://www.ucl.ac.uk/antiresdev/leaflet/MeDDiCABook

CONFERENCE PRESENTATIONS / ABSTRACTS

- MediTech2011, Cluj-Napoca, RO – 29th August/2nd September 2011 – *oral presentation*
- Marie Curie Researchers Symposium, Warsaw, PL – 25th/27th September 2011 – *poster presentation*
- CMBBE2012 in Berlin, DE – 11th/14th April 2012 – *poster presentation*
  C.M. Amatruda, P.V. Lawford, D.R. Hose and A.J. Narracott. (2012) *Spatial and temporal variation of vessel stress as a stimulus for neointimal growth.* The Proceedings of the 10th International Symposium on Computer Methods in Biomechanics and Biomedical Engineering. Published by ARUP; ISBN: 978-0-9562121-5-3
- ESB2012 in Lisbon, PT – 1st/4th July 2012 – *oral presentation*
  Amatruda, C. M., Hose, D. R., Lawford, P. V., & Narracott, A. J. (2012) *Influence of stent strut distribution on local vessel stress*. Journal of Biomechanics **45, Supplement 1**: S25. doi:10.1016/S0021-9290(12)70026-X
- VPH2012 in London, UK – September 18th/20th 2012 – *oral presentation*
- 8th Symposium in Vascular Biology and Cardiovascular Disease, Rotterdam, NL – 18th/19th April 2013 – *poster presentation*